Manipulating Structure and Properties of Colloidal In$_2$O$_3$ Nanocrystals

by

Shokouh Sadat Farvid

A thesis
presented to the University of Waterloo
in fulfillment of the
thesis requirement for the degree of
Doctor of Philosophy
in
Chemistry

Waterloo, Ontario, Canada, 2012

AUTHOR'S DECLARATION

I hereby declare that I am the sole author of this thesis. This is a true copy of the thesis, including any required final revisions, as accepted by my examiners.

I understand that my thesis may be made electronically available to the public.

Abstract

Transparent conducting oxides (TCOs) have attracted extensive attention for decades due to their remarkable applications in optoelectronic devices. The development of functional nanostructured TCOs with unique properties, and an expansion of their functionalities are therefore research directions of significant current interest. Among TCOs, In_2O_3 is widely applied because of its high charge carrier concentration and mobility, as well as the ease with which it can be deposited as a thin film. The important role of surfaces in tuning properties in materials shows the importance of studying nanostructured materials with high surface areas. In this thesis I examined the synthesis of phase-controlled In_2O_3 nanocrystals (NCs) and showed the effect of doping and composition on the materials properties. Owing to the relevance of size, structure, and composition for manipulating properties of nanomaterials, synthesis of well-defined nanocrystals of pure and doped In_2O_3 has been of considerable interest for fundamental studies as well as for technological applications.

Phase controlled synthesis of colloidal In_2O_3 NCs was achieved *via* a size-structure correlation. The study of the morphological and phase transformations of In_2O_3 NCs during their growth in solution implies that corundum (rh-In_2O_3) is a transient structure in the formation of cubic bixbyite (bcc-In_2O_3) phase. The formation of NCs smaller than 5 nm leads to the spontaneous stabilization of metastable phases owing to the surface energy and/or surface stress contributions, both of which are dependent on size. The growth beyond the critical size lowers the potential energy barrier height and causes the nanocrystal phase transformation. In addition, phase transformation of colloidal In_2O_3 NCs in the temperature range of 210-260 ˚C during their synthesis in solution was studied using a combination of structural and spectroscopic methods, including X-ray diffraction (XRD), transmission electron microscopy (TEM) and extended X-ray absorption fine structure (EXAFS) spectroscopy, and analyzed data using Johnson-Mehl-Avrami-Erofeyev-Kholmogorov (JMAEK) and interface nucleation models. The phase transformation occurs *via* nucleation of bcc-In_2O_3 phase at the interface between contacting rh-In_2O_3 NCs, and propagates rapidly throughout the NC volume. *In situ* high temperature XRD patterns collected during nonisothermal treatment of In_2O_3 NCs reveal that phase transformation of smaller NCs occurs at a faster rate and lower temperature, which is associated with the higher packing density and contact formation probability of smaller nanoparticles. Owing to the fact that NC surfaces and interfaces play a key role in phase transformation, their control through the synthesis conditions and reaction kinetics is an effective route to manipulating NC structure and properties.

Although, doping semiconductor NCs is crucial for enhancing and manipulating their functional properties, the doping mechanism and the effects of dopants on the nanocrystal growth and structure are not well understood. We show that dopant adsorption to the surfaces of colloidal In_2O_3 NCs during incorporation inhibit NC growth and leads to the formation of metastable rh-In_2O_3 for nanocrystals smaller than ca. 5 nm. Direct comparison between Cr^{3+} and Mn^{3+} dopants indicates that the nanocrystal structure directly determines the dopant incorporation limits and the dopant electronic structure, and can be predicted and controlled. These results enable a new approach to designing multifunctional nanostructures and understanding the early stages of crystal growth in the presence of impurities. Nanocrystalline films fabricated from colloidal Cr^{3+}- and Mn^{3+}- doped In_2O_3 nanocrystals exhibit strong ferromagnetic ordering up to room temperature. The absence of ferromagnetism in the free standing transition metal (TM)-doped In_2O_3 NCs and appearance of ferromagnetism only in TM:In_2O_3 films prepared from colloidal NCs, are attributed to the formation of extended structural defects, proposed to be oxygen vacancies at the NC interfaces. In fact, in TM:In_2O_3 NCs with high surface to volume ratios, more oxygen vacancies are present at the surface of NCs and networking of NCs in the prepared film causes an increase in grain-boundary defects at the interfaces. A comparative study of magnetic circular dichroism (MCD) spectra of Cr^{3+}-doped bcc-In_2O_3 and Cr^{3+}- doped rh-In_2O_3 revealed that Cr^{3+} ions distinctly occupy different symmetry sites in corundum and bixbyite crystal structure of In_2O_3. In fact, a change in the crystal structure of In_2O_3 from bixbyite to corundum changes the electronic configuration of Cr^{3+}.

By manipulating the NC composition and structure in solution we applied a one-step synthesis of ternary gallium indium oxide (GIO) nanocrystals with variable crystal structures. The structures and sizes of GIO NCs can be simultaneously controlled, owing to the difference in the growth kinetics of In_2O_3 and Ga_2O_3 NCs, and the polymorphic nature of both materials. These dependences, induced by the interactions between specific defect sites acting as electron donors and acceptors, were used to achieve broad emission tunability in the visible spectral range at room temperature. The nature of the photoluminescence is identified as donor -acceptor pair (DAP) recombination and changes with increasing indium content owing to the changes in the energy states of, and interactions between, donors and acceptors. Structural analysis of GIO nanocrystals by extended X-ray absorption fine structure spectroscopy reveals that In^{3+} occupies only octahedral, rather than tetrahedral, sites in the spinel-type γ-Ga_2O_3 nanocrystal host lattice, until reaching the substitutional incorporation limit of ca. 25%. The emission decay dynamics is also strongly influenced by the nanocrystal structure and composition.

Acknowledgements

Table of Contents

List of Figures

List of Tables

List of Abbreviations

bcc	Body-centered cubic
CN	Coordination number
DAP	Donor-acceptor pair
DMS	Diluted magnetic semiconductor
DMSO	Diluted magnetic semiconductor oxide
DSC	Differential scanning calorimetry
EXAFS	Extended X-ray absorption fine structure
FFT	Fast Fourier transform
FWHM	Full width at half maximum
GIO	Gallium indium oxide
ICP-AES	Inductively coupled plasma atomic emission spectroscopy
ITO	Indium tin oxide
JMAEK	Johnson-Mehl-Avrami-Erofeyev-Kholmogorov
LCP	Left circularly polarized
LFEA	Ligand-field electronic absorption
MCD	Magnetic circular dichroism
NC	Nanocrystal
PL	Photoluminescence
PPMS	Physical property measurement system
QBS	Quinine bisulfate
RCP	Right circularly polarized
rh	Rombohedral

STXM	Scanning transmission X-ray microscopy
TCO	Transparent conducting oxide
TEM	Transmission electron microscopy
TGA	Thermal gravimetric analysis
TM	Transition metal
TOPO	Tri-n-octylphosphine oxide
UV	Ultraviolet
Vis	Visible
XANES	X-ray absorption near edge structure
XMCD	X-ray magnetic circular dichroism
XAS	X-ray absorption spectroscopy
XRD	X-ray diffraction

Chapter 1[*]

Introduction

1.1 Transparent Conducting Oxides

Wide band gap semiconductor oxides, often referred to as transparent conducting oxides (TCOs), have found a variety of applications due to their attractive combination of properties — transparency to visible light, hardness, chemical inertness, and electrical conductivity. Such a combination of properties makes them suitable for the fabrication of transparent electrodes, sensors, catalysts, optical window coatings, and solar cells.[1, 2] Most TCOs are also polymorphic, which makes them good model systems for the fundamental studies of phase transformation in solid state, and allows for the control of their functional properties by structural manipulation.[3-5]

Structural defects such as oxygen vacancies play a crucial role in defining the properties of TCOs. The electrical and optical properties of TCOs can be tuned by controlling the defects in these materials.[6-8] Studies of TCO nanostructures have also received much recent attention, partly because of the increase in the surface-to-volume ratio, which has a significant importance for tuning the properties in TCOs and also because of the possibilities to manipulate their electronic structure at the nanoscale.

This thesis deals with identification of TCOs with the most favorable properties and an expansion of their functionalities. For example, photoluminescence (PL) in TCO nanocrystals (NCs) arises mostly from surface states and localized crystal lattice defects.[7] Subsequently, these NCs do not generally experience the same size-dependent emission tunability associated with quantum confinement like typical semiconductor quantum dots (i.e. CdSe, CdS, ZnSe etc.).[9]

As one of the most important functional oxides among the TCO materials, indium oxide is the focus of the present study. The polymorphs of In_2O_3 are cubic bixbyite- and corundum-type crystal structures.[5, 10] The bixbyite and corundum crystal structures are common for rare-earth oxides and transition metal oxides.[5, 11, 12] The structural relations as well as the possible phase transformation mechanism provide deeper understanding of functional properties in solid state materials. The superiority of In_2O_3 to the other TCOs is largely due to the higher mobility of electron in In_2O_3 films. Films of In_2O_3 prepared by various techniques have mobilities in the range 10-75 cm^2 V^{-1} s^{-1}, at a carrier density of ~ 10^{19}-10^{20} electrons cm^{-3}.[13, 14] Furthermore, the possibility of using the nanostructures of In_2O_3 and In_2O_3-based materials for different applications is attractive, because semiconductor NCs always shows unique size, shape, and composition dependent properties.

1.2 Indium Oxide Polymorphs

Indium oxide is a wide band gap ($E_g \approx 3.7$ eV) semiconductor, characterized by high charge carrier concentration and mobility, as well as the ease with which it can be deposited as a thin film.[14, 15] Because of these characteristics, In_2O_3 has been employed in batteries, solar cells, electrodes, displays and sensors.[16, 17] In In_2O_3, an oxygen vacancy is the major donor which causes the n-type conductivity. Oxygen vacancies in In_2O_3 have shallow states and are capable of producing free electrons in the conduction band.[18, 19] The energy required to form an oxygen vacancy decreases rapidly towards the surface (Figure 1.1) a consequence high electron concentration is present at surface and interface of In_2O_3.[19] The critical role of defects and defect states in manipulating properties in oxide materials shows the importance of studying nanostructured materials with high surface area and possibly a greater propensity for defect formation in NCs. The electronic device characteristic of indium oxide can be tuned by controlling defects in the material. Improvements in the performance of In_2O_3 thin-film and nanowire transistors by controlling the oxygen ratio have been reported.[20, 21]
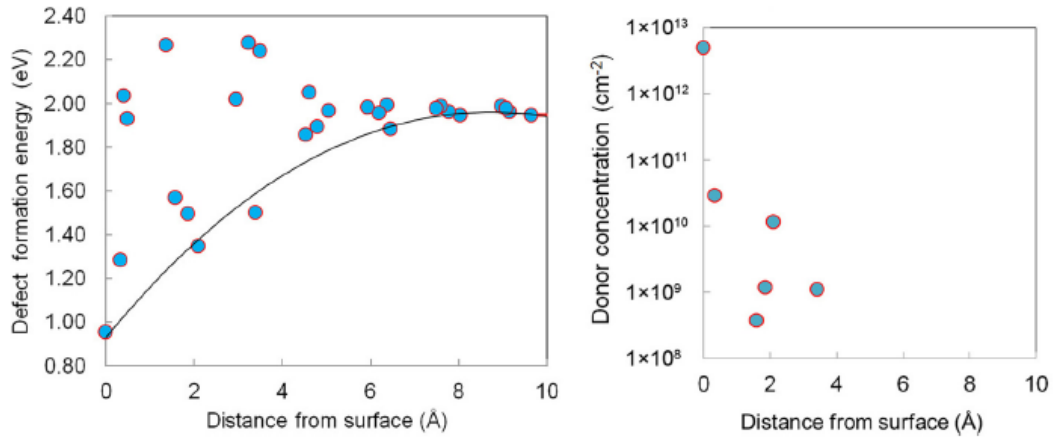
Figure 1.1 (left panel) Energy of formation for an oxygen vacancy in In_2O_3 as a function of distance from the (111) terminated surface, as calculated by density functional theory. (right panel) Distribution of surface donors at an equilibrium temperature of 750 K[19]†

The polymorphs of In_2O_3 have the cubic bixbyite-type crystal structure (bcc-In_2O_3, bcc=body-centered cubic) under ambient conditions, and the corundum-type structure (rh-In_2O_3, rh=rhombohedral) under high-pressure and temperature.[5, 10] The stable form of In_2O_3 having bixbyite-type crystal can be derived from the fluorite crystal structure by removing one-fourth of the anions, and slightly offsetting the positions of the remaining anion sites Figure 1.2a. As a consequence, In^{3+} cations exhibit two characteristic sites, known as b- and d-sites (Figure 1.2c).[22] One-fourth of In^{3+} cations reside in b-sites which have slightly trigonally compressed octahedral coordination with S_6 or C_{3i} symmetry.[12, 22] Three-fourths of In^{3+} cations are located in highly distorted octahedral d-sites with C_2 symmetry sites.[12, 22] As the symmetries of b- and d-sites are different, cations are expected to have distinct spectroscopic properties in these two sites. The metastable corundum-type In_2O_3 belongs to the hexagonal crystal family and consists of hexagonal close-packed oxygen ions, with In^{3+} filling two-thirds of the six-coordinate C_{3V} sites (Figure 1.2b, d).
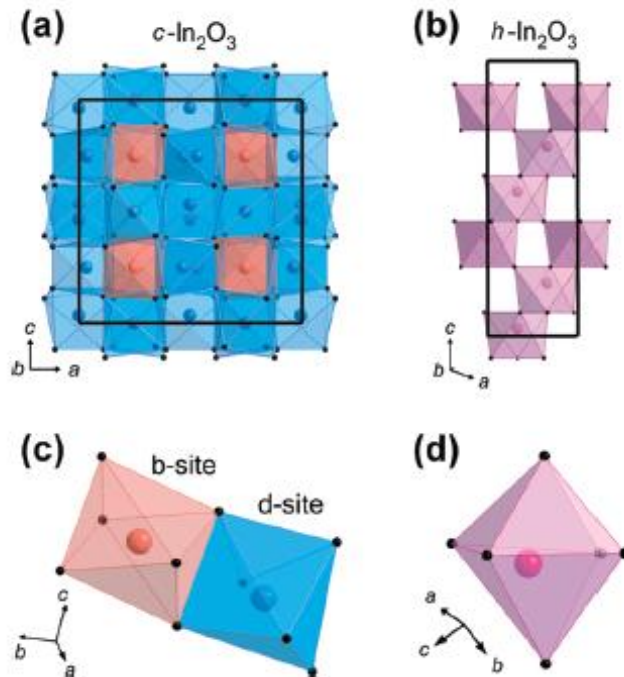
Figure 1.2 (a, b) Crystal unit cell of cubic bixbyite-type In_2O_3 (bcc-In_2O_3, a), and corundum-type In_2O_3 (rh-In_2O_3, b) viewed along the b-axes. The angle between a- and b- axes for rh-In_2O_3 is 120°. (c, d) The In^{3+} sites in bcc-In_2O_3 (c), and rh-In_2O_3 (d). Indium ions are shown as large colored spheres, and oxygen ions as small black spheres.[23‡]

1.3 Thermodynamic Phase Stability of NCs

The process of formation of a fresh surface of a substance is divided in two steps. In the first step, the solid or liquid expose a new surface by cleavage while the atoms stay fixed in the same positions that they occupy in the bulk phase.[3, 24] The reversible work per unit area in forming a new surface of a substance by cleavage is defined as the surface free energy.[3] Surface free energy constitutes a large part of the total free energy of substances of ultrafine particle sizes. In the second step, the atoms at the surface are allowed to rearrange to their final equilibrium positions.[24] The reversible work per unit area required to elastically stretch or compress a surface is the surface stress.[3] In the case of the liquid surfaces, these two steps occur as one, because the mobility of liquid molecules is high. Thus the work required for cleavage or surface stretching is the same, and surface free energy equals surface

stress.[24] For this reason, surface free energy is also called surface tension. However, for solids the atoms (or ions) are relatively immobile, the work needed in cleavage and surface deformation is not the same, thus with solids it is possible to stretch or to compress the surface region (surface stress) only by changing the distance of atoms on the surface.[3, 24]

It is now well known that the thermodynamic phase stability of solids can be spontaneously reversed below critical sizes. TiO_2 is a notable example; in bulk the rutile phase is thermodynamically more stable relative to anatase, whereas for particle sizes below ca. 14 nm anatase becomes more stable than rutile.[3, 4] The reversal of the phase stability in nanocrystalline materials has been associated with large surface to volume ratios in reduced dimensions. The high surface area of nanostructures can lead to the spontaneous stabilization of metastable phases, owing to the surface energy and/or surface stress contributions, both of which are dependent on size.[3] Control and manipulation of crystal structures has important implications for the design and preparation of new solid-state materials.

1.3.1 Thermodynamic Phase Stability of Indium Oxide NCs

The first synthesis of the metastable rh-In_2O_3 was reported by Shannon in 1966,[11] who found that at high temperature (1250 °C) and under high pressure (6.5 GPa) In_2O_3 undergoes phase transformation from the stable bixbyite crystal structure to the metastable corundum crystal structure. Rind and Ringwood reported in 1969 the formation of rh-In_2O_3 under the pressure of 12 GPa and temperature of 900 °C.[25] All reflections in XRD patterns in their work were similar to the report for the corundum crystal structure by Shannon.

For bulk In_2O_3 the cation-anion distances are nearly identical in both bixbyite and corundum crystal structures, and a small difference in density results from tighter packing of the anion layers in the corundum structure.[26] From Figure 1.3 it can be seen that equilibrium volume for rh-In_2O_3 is smaller, however, the total energy is higher than that for bcc-In_2O_3, indicating that bcc-In_2O_3 is more stable than rh-In_2O_3 under ambient conditions in agreement with experimental observations.[10, 27] Furthermore, at lower volumes and higher pressures the dependence of total energy for rh-In_2O_3 crosses that for bcc-In_2O_3. This indicates that upon compression bcc-In_2O_3 can be transformed into rh-In_2O_3.[10, 27] The pressure-induced structural transition is well demonstrated in the total energy variation with volume curves see in Figure 1.3.
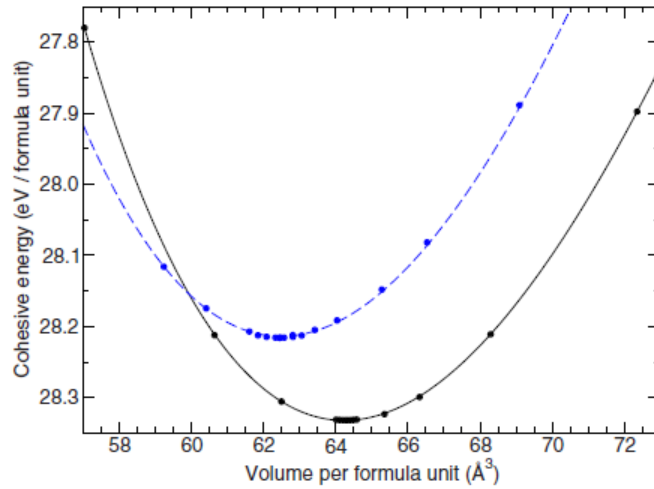
Figure 1.3 Cohesive energy versus volume (both per formula unit, f.u.= In_2O_3). Solid line: bcc-In_2O_3; dashed line: rh-In_2O_3[27]§

The dependence of the cell volume on applied pressure is shown in Figure 1.4. The volume shrinkage is 1.72 $Å^3$ at the transition pressure, which corresponds to an applied pressure of 3.83 GPa. This indicates that phase transition from bcc-In_2O_3 to rh-In_2O_3 is accompanied by reduction in the cell volume under applied pressure.[10]

Even if the rh-In_2O_3 is traditionally thought to be a high pressure In_2O_3 polymorph, recent work show that rh-In_2O_3 can also crystallize at ambient pressure conditions. The stabilization of rh-In_2O_3 under atmospheric pressure has been achieved by annealing of crystalline $In(OH)_3$, [28, 29] or InOOH nanofibers[30] and nanotubes.[31] The size-controlled rh-In_2O_3 nanocubes were reported by dehydration of small InOOH nanoparticles which were prepared by the solution-based surfactant-assisted method. Size of the rh-In_2O_3 nanocubes were modified between 8 and 12.3 nm by changing the surfactant ratios.[32]

Figure 1.4 Calculated cell volume as a function of pressure for bcc-In_2O_3 (open circle) and rh-In_2O_3 (open triangle). The pressure-induced phase transition point is marked with an arrow and the corresponding pressure value at the transition point (in GPa) is also stated.[10]**

1.4 Kinetics of Phase Transformation in NCs

The ability to obtain metastable high-energy structures in a controlled way requires fundamental understanding of the phase transformation mechanisms. A kinetic study of phase transformation provides quantitative information about energetic barriers between different crystal structures. Different nucleation and nuclei growth models have been used to describe the kinetics of solid-state reactions.[33-35]

The nucleation and nuclei growth models for solid state reactions and phase transformations assume that nucleation sites are randomly distributed within the lattice of the original phase.[34, 35] This assumption does not exclude the possibility of preferential nuclei formation at particular sites in the original phase, and only requires that these active sites be randomly distributed. One of the models widely used to describe solid-state phase transformations is the Johnson-Mehl-Avrami-Erofeyev-Kholmogorov (JMAEK) model,[33, 36-38] which correlates the phase transformation kinetics to the

---

** Reprinted with permission from: Karazhanov, S. Z.; Ravindran, P.; Vajeeston, P.; Ulyashin, A.; Finstad, T. G.; Fjellvåg, H. Phys. Rev. B, 76, 075129, 2007. Copyright (2007) by the American Physical Society

nucleation and growth rates of the newly formed phase, taking into account the coalescence and ingestion of the nuclei (Figure 1.5).[33]
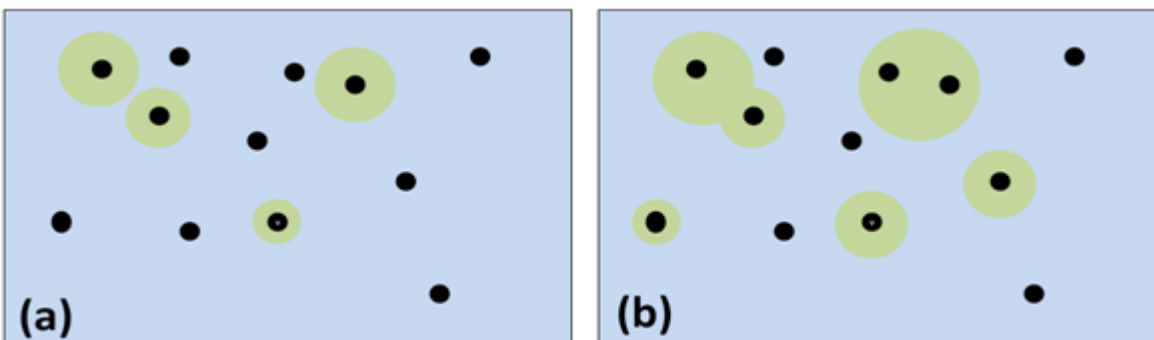
Figure 1.5 (a) Schematic representation of the phase transformation of one phase from another by the growth of nuclei forming randomly in the old phase. (b) Two types of nuclei growth restrictions; coalescence and ingestion. Black dots are nucleation sites, shaded light blue areas are old phase and olive areas are the new phase.

Although the JMAEK model is applicable to many solid-state reactions, it does not consider finite size effect.[39, 40] However other models have been developed to describe phase transformations in NCs based on the known or assumed mechanistic details. Notable examples include surface and interface nucleation models. The common assumption in these models is that defect sites either at the surfaces of NCs or at the interfaces between contacting NCs serve as nucleation sites for the formation of a new phase.[33, 41] However, it has been found that the correct value of the activation energy (E_a) for the isothermal kinetic data can be extracted using any model.[42, 43] Employing conventional models such as JMAEK therefore remains a good approach for obtaining the kinetic parameters from the isothermal measurements for cases in which a precise model is unavailable. The kinetics studies of phase transformation of TiO_2 NCs have suggested a strong size dependence of the phase transformation.[44, 45] Zhang *et al.*[41, 45, 46] proposed interface and surface nucleation models for the phase transformation of TiO_2 NCs under different conditions. The interface nucleation mechanism, for which a new phase is formed at the NC-NC contacts, occurs at low reaction temperatures and high packing density of NCs (Figure 1.6a). For low packing density of NCs the new phase forms at the surfaces of the old phase (surface nucleation mechanism). Once the new phase is nucleated, the transformation can quickly spread through NCs (Figure 1.6b).[41, 46]
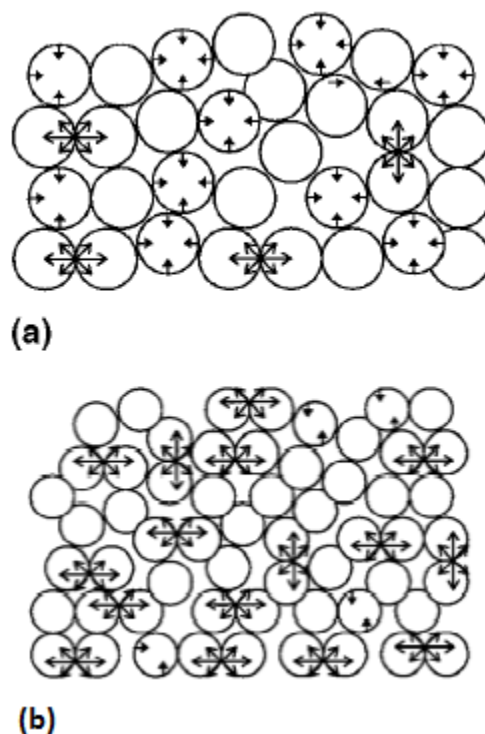
Figure 1.6 Diagram depicting relationship between the particle packing and nucleation mode in (a) 8-nm anatase powder with less dense particle packing and (b) 6 nm anatase powder with denser particle packing. Key: white circle, anatase; anchor arrow, interface nucleation; spike arrows, surface nucleation.**[41]**††

1.4.1 Kinetic Study of Phase Transformation in Indium Oxide NCs

Synthesis of metastable rh-In_2O_3 has been an increasingly active area of research in recent years, and the stabilization of nanocrystalline rh-In_2O_3 under ambient conditons has been related to solvents used for preparing the precursors[17, 28, 47] or the necessity of InOOH formation.[32, 47] Although there are a few reports on phase transformation of In_2O_3 from corundum to bixbyite crystal structure,[17] there has been no quantitative kinetic or mechanistic study of the phase transformation of In_2O_3 NCs in solution. The kinetics of phase transitions in NCs is usually simpler than those in bulk.[48] As such, colloidal NCs offer a unique opportunity to control metastability and manipulate structural transformations in solutions.

---

†† Zhang, H; Banfield, J. F., Phase Transformation of Nanocrystalline Anatase-to-Rutile via Combined Interface and Surface Nucleation, J. Mater. Res, 15, 2, 446, reproduced with permission.

1.5 Doped Semiconductor NCs

Intentional incorporation of impurities, a process known as doping, is central to tailoring electronic, optical, and magnetic properties of semiconductors.[49, 50] Colloidal doped semiconductor nanocrystals have attracted considerable attention in recent years due to their chemical flexibility and interesting multifunctional properties. They have been proposed as biological labels and recombination centers in hybrid organic/inorganic electroluminescent devices.[51] In addition these materials could potentially find application as spin filters in future spin-based information processing device.[52]

Incorporation of impurities into semiconductor lattices can modify electrical conductivity in doped semiconductor materials. A substitutional impurity with one more valence electron than the host atom is capable of providing extra electrons to the semiconductor. This creates an excess of negative (n-type) electron charge carriers to the semiconductor. Similarly, an impurity with one less valence electron can provide an extra hole (p-type). These electrons or holes are then available as carriers of electrical current within the semiconductor.

1.5.1 Magnetic Properties

Diluted magnetic semiconductors (DMSs) are one of the most interesting categories of doped semiconductors where a small percentage of magnetic dopants are uniformly dispersed in a non-magnetic semiconductor, and the resulting materials exhibit magnetic order, especially ferromagnetism.[49, 53] DMSs with Curie temperature (T_C) above room temperature have attracted intense interest in the field of spin-based electronics, or spintronics.[54] This emerging technology has shown promise as an alternative to traditional microelectronics, and relies on using electron spin, alone or in addition to charge, for information manipulation and storage. TCOs, such as ZnO, TiO_2, SnO_2, and In_2O_3 have attracted particular interest as host lattices for high-T_C DMSs, due to their stability, electrical conductivity, and optical transparency.[55-57] The observation of ferromagnetism in cobalt doped TiO_2 holds great promise to initiate the study of ferromagnetism in DMS oxides (DMSOs).[58] The doping concentrations in DMSOs are usually well below the limit required for any conventional ferromagnetic exchange interactions between neighboring ions which is traditionally used to describe magnetic ordering in oxides.[59] However the origin of ferromagnetism in DMSOs is under debate and poorly understood, and recent experimental and theoretical studies consider carrier-mediated ferromagnetism as one possible explanation for the origin of ferromagnetism in these materials.[13, 59]

10

Ferromagnetic exchange coupling in DMSOs was discussed by Coey *et al.* in terms of a simple model in which shallow donor electrons (e.g., oxygen vacancy) form magnetic polarons that mediate magnetic ordering in these materials.[59] At low concentration of donors, the localized impurity band forms, but above critical donor concentration the impurity band states would be delocalized. Interaction between the electronic states of the localized 3d impurity band, below the cation percolation threshold, and delocalized donor states lead to an extended hybridized state (Figure 1.7).[59]
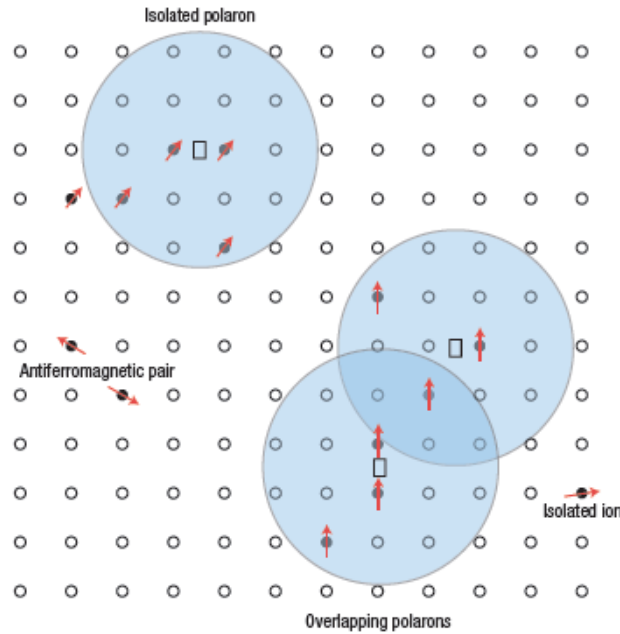
Figure 1.7 Representation of magnetic polarons. A donor electron in its hydrogenic orbit couples with its spin antiparallel to impurities with a 3*d* shell that is half-full or more than half-full. The figure is drawn for *x* (concentration of magnetic cations) = 0.1, γ = 12. Cation sites are represented by small circles. Oxygen is not shown; the unoccupied oxygen sites are represented by squares.[59‡‡]

Long-range magnetic ordering in nanocrystalline Co^{2+}:ZnO,[57] Ni^{2+}:ZnO,[56] and Ni^{2+}:SnO$_2$[55] prepared from analogous colloids has been attributed to an increase in the magnetic domain volumes through interparticle electronic coupling and to the generation of charge carriers through the formation of interfacial defects. The critical role of defects and defect states in mediating dopant ferromagnetic ordering in DMSOs implies the importance of studying nanostructured materials with high surface area and high concentration of defects at the surface and interfaces.

---

‡‡ Reprinted by permission from Macmillan Publishers Ltd: [Nat. Mater.] (Coey, J. M. D.; Venkatesan, M.; Fitzgerald, C. B. 2005, 4, 173-179.), copyright (2005)

1.5.2 Synthesis and Characterization of Doped Semiconductor NCs

A successful colloidal synthesis produces crystalline nanomaterials with controlled size, shape, composition, and crystal phase.[60, 61] Many different approaches to synthesize colloidal doped semiconductor nanocrystals have been explored. Hot-injection method has been used to synthesize colloidal Mn^{2+}-doped CdSe.[62] In this synthesis doping levels can be increased by dropwise addition of injected solution to the hot reaction mixture. Sol–gel method has been used to prepare colloidal Cr^{3+}-doped SnO_2 nanocrystals.[63] Study of nanocrystal surface ligand exchange revealed that even under mild reaction conditions and with a strong dopant preference for the host lattice a significant fraction of the dopant reside on the nanocrystal surfaces.[63] Mn^{2+}-doped CdS nanocrystals were synthesized with inverted micelle method where nanoparticles trapped in sol-gel silica matrices.[64] The most common strategy to incorporate dopants in the host lattice substitutional sites is to include a precursor containing dopants in the synthesis.[62, 63]

In spite of very promising results for doping semiconductor nanocrystals, this field of study has concerns regarding doping concentration level and incorporation of dopant uniformly in the semiconductor. Most studies of doped II-VI NCs, which have been the most widely studied host lattices, have reported low doping concentrations.[65] Thermodynamic and kinetic study of dopant incorporation in the nanocrystal can provide deeper understanding of dopant incorporation mechanism in these materials. In addition, to determine whether or not the dopant is uniformly incorporated in the semiconductor lattice, the resulting nanocrystals must be carefully characterized.[49, 50] Spectroscopic techniques are powerful for proving successful doping.[49] Optical absorption spectroscopy of Co doped CdS and ZnS nanocrystals revealed that electronic transitions are sensitive to environment and used to confirm doping in nanocrystals.[49, 66] Magnetic circular dichroism is another powerful technique. It can reveal whether a magnetic dopant is incorporated by measuring the influence of its magnetic spin on the nanocrystal states.[49, 57]

In addition, X-ray absorption spectroscopy (XAS) studies of dopant at K-edge can provide quantitative information about the local environment of dopant sites in the doped materials.[49, 67] This technique has been used as a dopant specific structural probe to provide accurate information about bond lengths and coordination numbers around dopant even at low doping levels.[68] For example, Extended X-ray absorption fine structure (EXAFS) data analysis of Mn K-edge for the first shell around the Mn for two nanocrystalline and one bulk Mn^{2+}-doped ZnS samples show that the Mn-S bond length has size dependence in Mn^{2+} doped ZnS.[67]

12

1.5.3 Doping Mechanism

Several doping mechanisms have been used to explain doping in semiconductor NCs. One proposed mechanism is known as self-purification.[50, 69] This model is governed by thermodynamic reasons and implies that nanocrystals are hard to dope, as it costs more energy to insert impurities into small nanocrystals than the larger ones.[69] In addition, the distance which a defect or impurity must move to reach the surface of a nanocrystal is very small and that impurities are easily expelled from the NCs.[69] However, a fundamental assumption in this view is thermodynamic equilibrium, which is strongly dependent on the diffusion of impurity atoms. This diffusion of impurities works well for solid or gas phase syntheses at high temperature where most dopants diffuse rapidly, whereas in colloidal synthesis which are performed at relatively lower temperature, diffusion may or may not be facile.[50] This suggests that if thermodynamic equilibrium is not established, then kinetic factors will govern the doping incorporation mechanism. In the trapped dopant model which are carried out based on the kinetic assumption, the adsorption of impurities on the nanocrystal surface during the growth controls the doping incorporation in the NCs (Figure 1.8).[50] These considerations suggest that nanocrystal shape, surface morphology, and surfactants are the main factors that control dopant incorporation. These criteria have been used to explain Mn doping in II-VI nanocrystals. Theoretical studies of colloidal Mn-doped II-VI NCs have suggested that the doping mechanism involves preferential adsorption of impurities on the specific NC surfaces, and that NC surface energies can be used to predict a possibility of doping particular NCs.[65] Also, this model has suggested that CdSe NCs may be more easily doped if they had zinc blende, rather than wurtzite structure, a claim that is still under debate in the literature.[70]
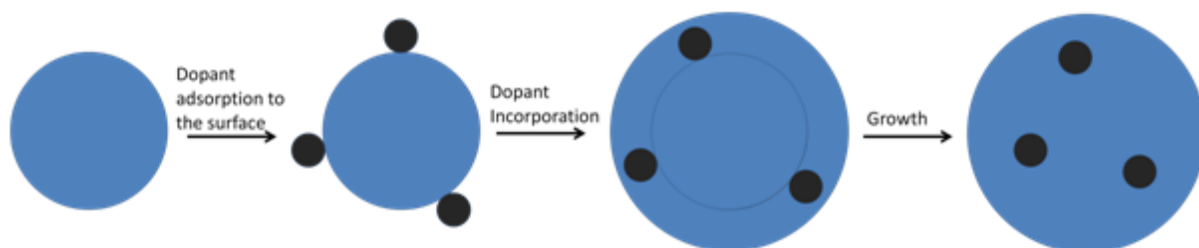
Figure 1.8 Schematic of trapped dopant model.

If semiconductor NCs having distinctly different crystal structures could somehow be synthesized and doped under identical conditions, the dopant incorporation could be systematically studied with respect to the NC structure, morphology, and faceting.

1.6 Doped In_2O_3 NCs

In_2O_3 is a well-known wide band gap semiconductor oxide with high optical transparency and high charge carrier concentrations.[14, 15] Indium oxide exhibits intrinsic n-type semiconductor behavior, which can be further doped to yield low resistivity, such as in indium tin oxide (ITO).[14] The difference of valence between In^{3+} and Sn^{4+} results in donation of a free electron to the host lattice. The synthesis of ITO nanoparticles is of particular technological interest due to the low manufacturing cost and easy processability of nanoparticles into films.[71, 72] Additionally, interest in applying ink-jet printing technology to ITO requires nanoparticles that display high crystallinity with non-agglomeration in solution.[71, 73] In addition, other ternary compounds of In_2O_3 have attracted attention as new materials for TCOs.[74] Some of these materials may exhibit properties that are suitable for specialized applications. For example, gallium indium oxide which is a wide band gap semiconductor with high transparency and conductivity has been employed as thin-film transistor channel layers.[74, 75]

Intrinsic properties of In_2O_3 make this TCO a very promising host lattice for the preparation high T_C magnetic semiconductors.[14, 15] Different magnetic behavior was reported for transition metal ions doped in In_2O_3 based on synthesis conditions and method of preparation. Room temperature ferromagnetism has been reported for Cr, Fe, Co and Ni doped In_2O_3 thin films,[76] Fe doped In_2O_3 nanoparticles[77] and Cr doped In_2O_3 thin film and bulk.[13, 78] However, Berardan *et al*.[79] have shown that Cr, Mn, Fe, Ni and Cu doped nanocrystalline and bulk In_2O_3 is intrinsically paramagnetic and ferromagnetism was observed when magnetic dopant concentrations exceeding the percolation threshold which was linked to the formation of magnetic secondary phase. These discrepancies in the data reported for the nominally same materials by different groups emphasize that a careful correlation between structural studies and magnetism must be established by applying more reliable materials characterization techniques.

1.7 Motivations and Scope of the Thesis

In_2O_3 polymorphs crystallize in the form of bcc-In_2O_3 under normal conditions and rh-In_2O_3 under high-pressure and temperature. In this thesis work, we study phase controlled synthesis of In_2O_3 NCs and show the effect of size, structure, doping and composition on material properties of colloidal In_2O_3 NCs.

We report the study of the morphological and phase transformations of In_2O_3 NCs during their growth in solution, and show that rh-In_2O_3 is a transient structure in the formation of bcc-In_2O_3 NCs. We demonstrate a direct correlation between the nanocrystal size and structure, which allows for the stabilization of rh-In_2O_3 for NCs smaller than 5 nm. These results enable a direct, straightforward and highly selective synthesis of colloidal In_2O_3 NCs having different phases by adjusting the reaction conditions. In addition, a detailed kinetic study of the phase transformation of colloidal rh-In_2O_3 to bcc-In_2O_3 NCs during their growth in solution was investigated. The correlation between the rates of NC growth and phase transformation was established, indicating size-dependent metastable phase stabilization and transformation. The structural information about the reaction products at different times during the synthesis were obtained from the X-ray diffraction (XRD), X-ray absorption spectroscopy measurements, and analyzed using JMAEK and interface nucleation models. The kinetic analysis in conjunction with the electron microscopy results suggests the dominant interface nucleation mechanism at low temperature. The effect of the NC interactions on the phase transformation of In_2O_3 NCs and the role of surface stress in this process are also discussed. The mechanistic results of this work allow for a rational optimization of the reaction conditions for the synthesis of colloidal In_2O_3 NCs as building blocks with a desired crystal structure, and contribute to the general understanding of the structural transformation and property control in the solid state.

Crystal structures of rh-In_2O_3 and bcc-In_2O_3 are characteristic for oxides of a few transition-metals, which are commonly used as magnetic dopants in DMSs. Specifically, Cr_2O_3 has the corundum-, and Mn_2O_3 the bixbyite-type crystal structure. The isostructural nature of Cr_2O_3 and Mn_2O_3 with one of the polymorphs of In_2O_3 and the simpler phase transition mechanism in NCs compared to bulk inspired us to explore the possibility of using Mn^{3+} and Cr^{3+} dopants to manipulate the growth and structure of In_2O_3 NCs, and study directly the mechanism of dopant incorporation. We experimentally identified the structural similarity between the dopant transition-metal oxide and the In_2O_3 host as key components determining the affinity of dopant ions for the incorporation into NCs. In addition, a combination of structural and spectroscopic methods, including XRD, TEM, EXAFS, MCD and electronic absorption, provide a direct correlation between transition metal doped in individual NCs and the magnetic properties of the corresponding TM:In_2O_3 nanocrystalline films.

To demonstrate a broad tunability of the visible emission by manipulating the NC composition and structure in solution, we applied a one-step synthesis of ternary gallium indium oxide ($Ga_{2-x}In_xO_3$, $0 \leq x \leq 2$, further in the text generally referred to as GIO) colloidal NCs throughout the entire

15

composition range. To our knowledge, studies of alloyed colloidal GIO NCs with compositionally-tunable emission have not been reported to date. Ga_2O_3 is chemically related to In_2O_3 since both Ga and In belong to the same group of the periodic table and have the same oxidation state in their respective oxides (+3). This should allow for a controlled incorporation of In^{3+} into Ga_2O_3 and Ga^{3+} into In_2O_3 and the formation of colloidal alloyed NCs, without introducing new defect sites associated with charge compensation. The PL mechanism identified as the donor-acceptor pair (DAP) recombination changes with the NC composition on the basis of the interactions between donors and acceptors. The reported results open the door for rational tuning of the visible PL in TCO-NCs and further expansion of their inherent degrees of freedom.

Chapter 2

Experimental Section

2.1 Materials

All reagents were used as received. Indium acetylacetonate (In(acac)$_3$; 98%), Gallium acetylacetonate (Ga(acac)$_3$, 99.99%), and chromium acetylacetonate (Cr(acac)$_3$; 97.5%) were purchased from Strem Chemicals. Manganese acetylacetonate (Mn(acac)$_3$) was purchased from Alfa Aesar. Oleylamine (70%) and tri-*n*-octylphosphine oxide (TOPO; 90%) were purchased from Sigma-Aldrich Company. Toluene (99.98%, EMD Chemicals), hexane (99.9%, Fischer Scientific) and absolute ethanol were used as solvents without further purification.

2.2 Synthesis and Samples Preparation

2.2.1 Synthesis of In$_2$O$_3$ NCs

In$_2$O$_3$ NCs were synthesized using a single-step procedure similar to the one previously reported.[80] In a typical reaction, 4 mmol of In(acac)$_3$ and 48 mmol of oleylamine were mixed in a 100 ml three-neck round-bottom flask and magnetically stirred for 15 minutes under a flow of argon. The reaction mixture was heated up to the desired temperature in the argon atmosphere. The reaction mixture was then refluxed at the final temperature. For the kinetic study of the phase transformation of In$_2$O$_3$ NCs portions of the obtained product were taken at different times during the reaction. For nonisothermal kinetic investigations in solution the reaction mixture was allowed to reach 240 °C while stirring for 1 h, and with the heating continuing at the rate of 1 °C/min, the aliquots were taken in the temperature range 250-280 °C. The obtained samples were cooled to room temperature, and the NCs were precipitated and washed three times with ethanol.

For *in situ* nonisothermal XRD study of the phase transformation of larger (ca. 5 nm) rh-In$_2$O$_3$ NCs, the sample was prepared in the powder form by the alcoholysis method, according to the previously reported procedure.[35] In this synthesis, 1 mmol of In(NO$_3$)$_3$ was dissolved in 50 ml of ethanol and stirred for 30 min. The same volume of 0.15 M NaOH solution in ethanol was added to the reaction mixture and the obtained In(OH)$_3$ precipitate was washed with ethanol, dried in air, and finally calcined to obtain rh-In$_2$O$_3$ NCs.

2.2.2 Synthesis of Chromium and Manganese Doped In_2O_3 NCs

Doped In_2O_3 NCs are prepared using the same methods described for the synthesis of pure In_2O_3 NCs, but in the presence of various amounts of dopant precursor ($Cr(acac)_3$ or $Mn(acac)_3$) in the precursor mixture. The doped NCs were dispersed and heated in TOPO, followed by re-precipitation with ethanol. This procedure was repeated three times to ensure the removal of surface-bound dopant ions. The obtained NCs were suspended in hexane or toluene.

2.2.3 Synthesis of Gallium Indium Oxide NCs

All reactions were carried out using argon protection. In a typical synthesis, $Ga(acac)_3$ and $In(acac)_3$ were mixed in a 100 ml three-neck round-bottom flask with 9 g of oleylamine, and magnetically stirred under a flow of argon at 80 °C until the precursors were fully dissolved. The synthesis of pristine γ-Ga_2O_3 NCs was performed utilizing 1.2 g of $Ga(acac)_3$, and for the syntheses of gallium indium oxide NCs a certain amount of $Ga(acac)_3$ was systematically replaced with $In(acac)_3$ to obtain alloyed NC samples throughout the full composition range. A solution was degassed and heated to 200 °C (290 °C) at an average rate of ca. 3 °C/min. The reaction mixture was then refluxed in the argon atmosphere for 30 hours. The obtained product was cooled to room temperature, and the NCs were precipitated by the addition of 20 ml of ethanol followed by centrifugation at 3000 rpm for 5 minutes. The isolated fine white powder was washed 3 times with ethanol and centrifuged. Finally, NCs were capped with TOPO and dispersed in hexane or toluene.

2.2.4 Synthesis of Nanocrystalline Cr_2O_3

Nanocrystalline Cr_2O_3, the most common oxide of chromium, was prepared by a different method[81] in order to compare its structural and magnetization properties with the analogous properties of Cr^{3+}:In_2O_3 NCs. Nanocrystalline Cr_2O_3 was prepared by calcinations of a dried gel of $Cr(OH)_3$ precipitate. The $Cr(OH)_3$ was precipitated from a solution of 0.05 M $CrCl_3 \cdot 6H_2O$ with 0.18 M NaOH. The resulting gel was filtered and washed several times with deionized water. The obtained amorphous $Cr(OH)_3 \cdot xH_2O$ precursor was dried overnight at 60 °C, and calcined in air for 3 h at 350 °C.

2.2.5 Size Selective Precipitation

In addition to narrow the size distribution and separate rh- In_2O_3 and bcc- In_2O_3 NCs we applied size selective precipitation method. In this method, viscous suspension of NCs including both large

and small particles was first centrifuged at 3000 rpm for 5 min. Large In_2O_3 NCs with bixbyite-type crystal structure were first precipitated. Small NCs with rh-In_2O_3 phase were then precipitated from the supernatant by adding 20 mL of ethanol and centrifuging for 10 min at 3000 rpm.

2.3 Measurements and Data Analysis

2.3.1 Powder X-ray Diffraction

X-ray diffraction (XRD) is a powerful tool to determine the structures of unknown materials and find the unit cell parameters of crystals. Powder XRD is perhaps the most widely used x-ray diffraction technique for characterizing materials. Besides determining the structure of unknown materials, the crystallite size can also be estimated from the XRD peak width using the Debye-Scherrer equation which is

$$\text{Crystallite size (average value)} = \frac{K \lambda}{B \cos(\theta)} \qquad \textbf{Equation 1}$$

where K is the Scherrer constant, λ is wavelength of radiation, and B is the line broadening at half the maximum intensity (FWHM) in radians, θ is the peak position.

Powder XRD patterns were collected with an INEL powder diffractometer equipped with a position-sensitive detector, using monochromatic Cu Kα radiation. For XRD measurements, the NCs were precipitated with ethanol, air-dried, and loaded as powders into an aluminum XRD sample holder.

2.3.1.1 *In-situ* XRD Measurements

The *in-situ* nonisothermal phase transformation was investigated by XRD measurements in the argon atmosphere, using the same diffractometer fitted with a high temperature reactor chamber. The samples were preheated in the chamber to 240 ˚C with a heating rate of 5 ˚C /min. Upon temperature stabilization the sample was heated at the same rate to different temperatures, and upon reaching the desired temperature the XRD pattern was recorded for 15 minutes.

2.3.1.2 Linear Combination and Deconvolution Analyses of XRD patterns

We performed the linear combination and deconvolution analyses to determine the phase contents of In_2O_3 NC samples synthesized between 0 and 30 h in the temperature range 210-260 ˚C. For the linear combination analysis we used rh-In_2O_3 and bcc-In_2O_3 NCs obtained with high purity in the 30 h

reaction at 200 ˚C and 7 h reaction at 230 ˚C, respectively, as references. The phase contents of the samples synthesized in the temperature range 210-260 ˚C for different durations were determined by matching their XRD patterns to the linear combination of the reference XRD patterns. For the deconvolution method, the phase contents of In_2O_3 NCs were calculated by fitting the overlapped bcc-In_2O_3 (222) and (400), and rh-In_2O_3 (104) and (110) peaks. The intensities of the four peaks were set proportionally to their standard intensities based on the JCPDS cards of these two phases. The weight fraction of bcc-In_2O_3 (W_{bcc}) can be calculated from:

$$W_{bcc} = \frac{A_{bcc}}{A_{bcc} + 3.4A_{rh}} \qquad \textbf{Equation 2}$$

where A_{bcc} and A_{rh} are the integrated intensities of the bcc-In_2O_3 (222) and rh-In_2O_3 (104) peaks, respectively. The integrated intensity ratio for the bcc-In_2O_3 (222) peak to the rh-In_2O_3 (104) peak obtained from the XRD pattern of the two references is 3.4.

2.3.2 Raman Spectroscopy

Raman spectroscopy is a spectroscopic technique based on inelastic scattering of monochromatic light, usually from a laser source. The laser light interacts with molecular vibrations, phonons or other excitations in the system, resulting in shifts in the laser photon energy. These shifts provide information about the vibrational modes in the system. The Raman spectrum is more sensitive to the lengths, strengths, and arrangement of chemical bonds in a material, rather than to the chemical composition. Raman spectra were recorded at room temperature using a Renishaw 1000 spectrometer using a He-Ne laser with ~10 % of the maximum laser output power (40 mW). The spectrometer was calibrated using a silicon standard. For Raman measurements, the NCs powder were transferred to the glass slide and excited at wavelength of 632.8 nm.

2.3.3 Electron Microscopy

Transmission electron microscopy (TEM) imaging was performed with a JEOL-2010F microscope operating at 200 kV. The specimens were prepared by dropping dilute suspensions of colloidal NCs in toluene on copper grids with lacey formvar/carbon support films purchased from Ted Pella, Inc. Gatan Digital Micrograph software was used to measure d-spacing from TEM images.

2.3.4 X-ray Absorption Spectroscopy

There are three main regions found on the X-ray absorption spectrum (Figure 2.1). Depending on the photon energy, different processes will occur that lead to different features in the X-ray absorption spectrum. At low energy, before the ionization energy, the transition of the electron from a core electronic level is not possible, because the incident photon has low energy to allow the electron to reach the first available electronic levels. This region is named the pre-edge. In a very narrow domain of a few eV around the absorption edge, the absorption coefficient increases drastically, which indicates that the energy transferred from the photon to the electron is sufficiently high to allow this electron to reach the first available energy levels. This leads to more or less complex features in the absorption edge, and this region is called the X-ray absorption near edge structure (XANES). Analysis of this part of the spectrum provides information about the electronic structure, such as spin state and oxidation state.

When the energy is slightly larger the ionization energy, the absorption coefficient exhibits modulations with decreasing amplitude. In this region, the electron is expelled from the absorbing atom and goes on to explore the environment with a residual kinetic energy equal to the energy of the incident photon minus the energy required to transfer the electron from its ground level to the first available energy levels. This region is called EXAFS. The analysis of this part of the absorption spectrum gives information regarding the nature and number of neighbors and bond distances.

XAS measurements were performed at the beamline 06ID-1 at the Canadian Light Source (CLS). For the In K-edge the energy was scanned in the range of 27690-28797.2 eV. For Cr K-edge the energy was scanned in the range of 5739-6869.2 eV. The scan started from 250 eV below the edge (for indium at 27940 eV and for chromium at 5989 eV) to 50 eV below the edge in 10 eV steps. Between 50 eV below the edge and 50 eV above the edge, the step size was 0.2 eV. Above 50 eV of the edge the step size was 0.05 Å^{-1} until the end of the scan was reached at $15k$ (where $k = [0.2625\ (E-E_0)]^{\frac{1}{2}}$).
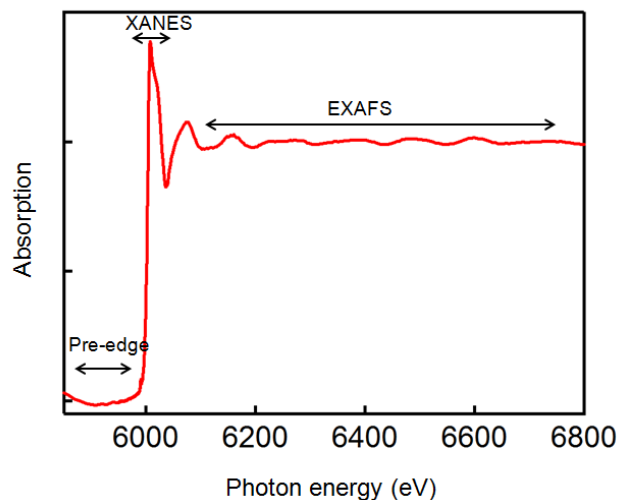
Figure 2.1 X-ray absorption spectra showing three main regions: pre-edge, XANES, and EXAFS.

2.3.4.1 Indium K-edge XAS Measurements

To measure indium K-edge XAS, the Si (220) crystal was used as an X-ray beam monochromator, and the harmonics rejection was achieved by detuning the second monochromator crystal by 60 %. Indium K-edge energy calibration was carried out by using the Sn foil standard (K-edge at 29200 eV). For In_2O_3 NC samples, the spectra were recorded in the transmission mode with three ionization chambers. The first and second ionization chambers were used to monitor the incident and transmitted X-ray intensities, respectively. The third ionization chamber was used in conjunction with the Sn foil standard to provide internal calibration for the In K-edge position. For GIO NC samples, the spectra were collected in the fluorescence mode with a 32-element germanium array detector. In this setup, the samples were positioned at 45° angle to the incident beam, while the fluorescence signal was detected at 90° with respect to the incident beam.

2.3.4.2 Chromium K-edge XAS Measurements

To measure Chromium K-edge XAS the Si (111) double-crystal was used to monochromatize the radiation. Chromium K-edge energy calibration was carried out by using chromium foil standard (K-edge at 5989 eV). For Cr_2O_3 standard sample the spectra were recorded in the transmission mode while for $Cr^{3+}:In_2O_3$ NC samples, the spectra were collected in the fluorescence mode.

2.3.4.3 EXAFS Data Analysis

EXAFS data analysis was performed with the Cherokee and RoundMidnight codes from the Multiplatform Applications for XAFS (MAX) package.[35] EXAFS data were analyzed according to the single scattering theory. Firstly, the background below the edge jump was removed by extrapolation of the pre-edge absorption using Lengeler-Eisenberger method, and the post-edge background was modeled by interpolation of the atomic-absorption background by a fifth- or sixth-degree polynomial. The extracted EXAFS spectra were converted from energy (E) to wave-vector (k), and then Fourier transformed from k-space to R-space by using a Kaiser-Bassel window ($\tau = 2.5$). The peaks corresponding to the first oxygen and second cation shells were filtered and back-Fourier transformed to k-space for further fitting. Fitting of the Fourier-filtered spectra was performed using the EXAFS expression based on the single scattering theory:

$$k.\chi(k) = S_0^2 \sum_i \frac{N_i}{R_i^2} A_i(k) e^{-2\sigma_i^2 k^2} e^{\frac{-2R_i}{\lambda(k)}} \sin(2kR_i + \Phi_i(k)) \qquad \textbf{Equation 3}$$

where $\chi(k)$ is the EXAFS amplitude, $A_i(k)$ and $\Phi_i(k)$ respectively, are back scattering amplitude from and phase shift between absorber and each of the back scattering atoms (N_j), R_j is the distance of jth atom from the absorber, $\lambda(k)$ is the photoelectron mean-free path, σ_j^2 is the Debye-Waller factor, and S_0^2 is an amplitude reduction factor. EXAFS structural parameters were obtained by least-squares analysis of the Fourier filtered data using phase and amplitude functions generated from FEFF6 code with input data based on the crystallographic information for In-O and metal-metal bond distances.

The weighted residual factor (ρ) was calculated using the following formula:

$$\rho = \frac{\sum_k k[k\chi_{\exp}(k) - k\chi_{calc}(k)]^2}{\sum_k k[k\chi_{\exp}(k)]^2} \qquad \textbf{Equation 4}$$

2.3.5 Photoluminescence Spectroscopy

Photoluminescence spectra were recorded with a Varian Cary Eclipse fluorescence spectrometer. For the delayed PL measurements, the samples were excited in the maximum of the excitation band

with a pulsed Xenon flash lamp, and the emission intensity at each point was recorded 0.1 ms after excitation (delay time) for 0.04 ms (gate time).

2.3.5.1 Relative Quantum Yield Measurements

Relative quantum yields of the NC samples were calculated using quinine bisulfate (QBS) as the reference substance, based on the following expression:

$$\Phi = \Phi_R \frac{I}{I_R} \frac{A_R}{A} \frac{n^2}{n_R^2}$$ **Equation 5**

where Φ is the quantum yield, I is the area under the emission peak (wavelength scale), A is absorbance at the excitation wavelength, and n is the refractive index of the sample. The subscript R denotes the analogous quantities of the reference. A solution of QBS was prepared in 1 N H_2SO_4 as previously described.[82] The quantum yield of QBS under these conditions was determined to be 0.55.

2.3.6 UV-Vis Absorption Spectroscopy

Ultraviolet-visible (UV-Vis) spectroscopy involves the spectroscopy of photons in the UV-visible region. Electronic absorption spectroscopy has played a key role in the development of methods for synthesizing semiconductor nanocrystals including nanocrystal sizes, growth kinetics, growth mechanisms, and electronic structures.

The electronic absorption spectra of doped semiconductor nanocrystals contain considerably more features than those of the pure host nanocrystals. The transitions observed may be grouped into three general classes: (a) the band gap transition which corresponds to the valence band to the conduction band transitions of the semiconductor host lattice, (b) the d–d transitions of the dopant ions in the lattice environment, and (c) charge transfer transitions. These make this spectroscopy a valuable technique to determine the doping speciation.

The optical absorption spectra of colloidal NCs were collected on a Varian Cary 5000 UV-vis-NIR spectrophotometer using 1cm path-length quartz cell.

2.3.7 Magnetic Circular Dichroism

Magnetic circular dichroism (MCD) spectroscopy measures the difference in absorption of left circularly polarized (LCP) and right circularly polarized (RCP) light between Zeeman-split ground and excited states in a magnetic field (Figure 2.2). The difference in absorption is defined by

24

convention as $\Delta A = A_- - A_+$, where A_- is LCP absorption and A_+ is RCP absorption. In addition, it is necessary that the ground and/or excited state possess non-zero angular momentum (j).[83, 84]

The most important use of MCD spectra is to assist in the interpretation of electronic spectra and provide experimentally based information about the electronic states involved in the observed transitions. MCD spectra showed improved resolution in the observed electronic transitions compared to absorption measurements (particularly for transition metals). In addition, MCD spectroscopy provides selective investigation of magnetic properties of individual metal centers via temperature and magnetic field dependence studies of discrete transitions (optical detection of magnetization).
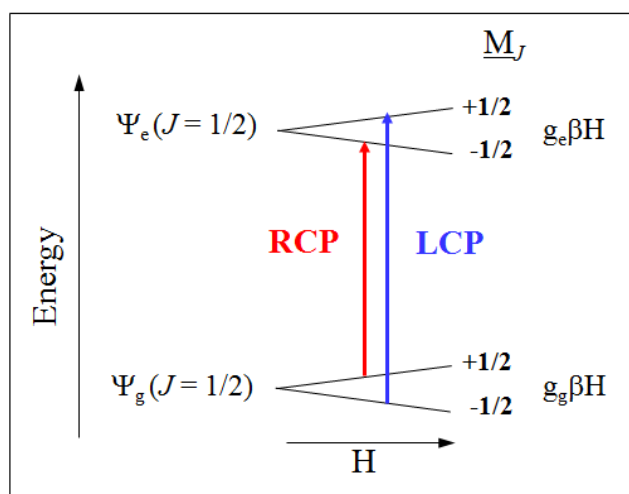
Figure 2.2 Schematic representation of the MCD selection rules.

MCD spectra were measured with Jasco J-815 spectropolarimeter using a high-field superconducting magneto-optical cryostat (SM4000-8, Oxford) with a variable-temperature (1.5-300 K) and variable magnetic field (0-8 T) compartment positioned in the Faraday configuration. For MCD measurements, the colloidal suspensions were deposited on high quality quartz disks and mounted in the appropriate cryostats.

2.3.8 Magnetic Measurements

The magnetization was measured with the physical property measurement system (PPMS, Quantum Design) in ACMS mode, with a helium cooling system, allowing a wide range of temperatures from 2 to 400 K and magnetic fields up to $\pm$ 9 Tesla. The overall effective magnetic moment can be measured as a function of temperature, or the applied magnetic field from a positive to a negative one, monitoring magnetic properties. For magnetization measurements of free-standing

NCs, the NC powders were precipitated with ethanol, air-dried, and loaded as powders into measurement capsules. For magnetization measurements of nanocrystalline films, the colloidal NCs were spin-coated multiple times on the clean sapphire substrates, followed by mild annealing at 300º C for 1 minute between consecutive coatings (Figure 2.3). The final nanocrystalline films were weighed again on an analytical balance in order to determine the magnetization per unit mass of the samples. All samples were handled identically under carefully controlled magnetic contamination-free conditions. For each sample, three to five films were prepared. Although the magnetic moment varies, the data was generally in good agreement from one film to another.
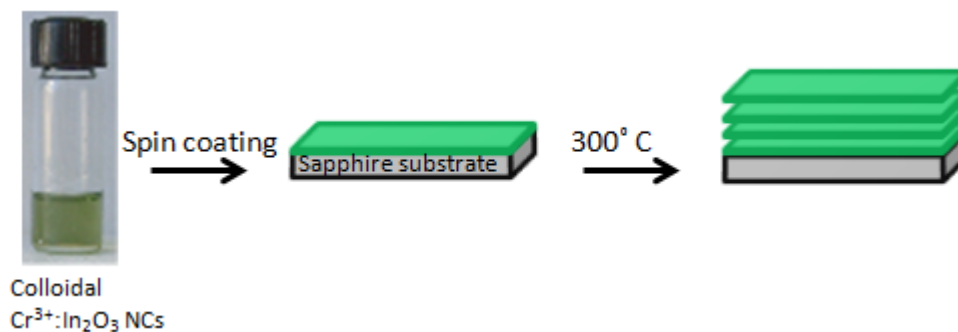
Figure 2.3 Schematic representation of preparation of films from colloidal Cr^{3+}:In_2O_3 NCs for magnetic measurements.

The saturation magnetization per dopant ion in the nanocrystalline film was estimated based on the unit mass magnetization and the elemental composition of the sample. The NCs have a significant amount of TOPO ligands, which must be taken into account when calculating the magnetic moment per dopant ion in NCs. From the phosphorus inductively coupled plasma atomic emission spectroscopy (ICP-AES) analysis, we determined the amount of TOPO ligands associated with the NCs in the nanocrystalline film after additional drying. The mass of the dried doped NCs in the film was then corrected for this amount of TOPO. Then, this corrected mass, is used to determine the magnetization per dopant ion.

Chapter 3

Phase-Controlled Synthesis of Colloidal In$_2$O$_3$ Nanocrystals and a Kinetic Study of Phase Transformation

In this part of my thesis we studied phase-controlled synthesis of In$_2$O$_3$ NCs during their growth in solution. This chapter presents a detailed kinetic study of the phase transformation of colloidal rh-In$_2$O$_3$ to bcc-In$_2$O$_3$ NCs during their growth in solution by a combination of structural and spectroscopic methods, including XRD, TEM and EXAFS spectroscopy. These results enable a direct, straightforward and highly selective synthesis of colloidal In$_2$O$_3$ NCs having different phases by adjusting the reaction conditions.

3.1 Phase-Controlled Synthesis of Colloidal In$_2$O$_3$ NCs via Size-Structure Correlations

3.1.1 Synthesis of In$_2$O$_3$ NCs during Growth in Solution

TEM images of the In$_2$O$_3$ NCs obtained at 250 ˚C at different reaction times during the synthesis are shown in Figure 3.1. Immediately upon reaching the final reaction temperature the samples have a network-like structure with a few sub-5 nm particles imbedded in the network (Figure 3.1a). After 10 minutes the number of nanoparticles increases with respect to the nanostructured network, and they become larger and faceted (Figure 3.1b). This process continues over time (30 minutes, Figure 3.1c), and after 1 h the network completely disappears, leaving behind only nanoparticles, which are much more uniform in size (Figure 3.1d). XRD patterns of several representative samples collected at different times during the synthesis are shown in Figure 3.1e. All samples are crystalline, although broadening of the XRD peaks decreases for products obtained at longer reaction times due to an increase in the size of the crystalline domains. Surprisingly, a change in the crystal structure was observed during the reaction.

27
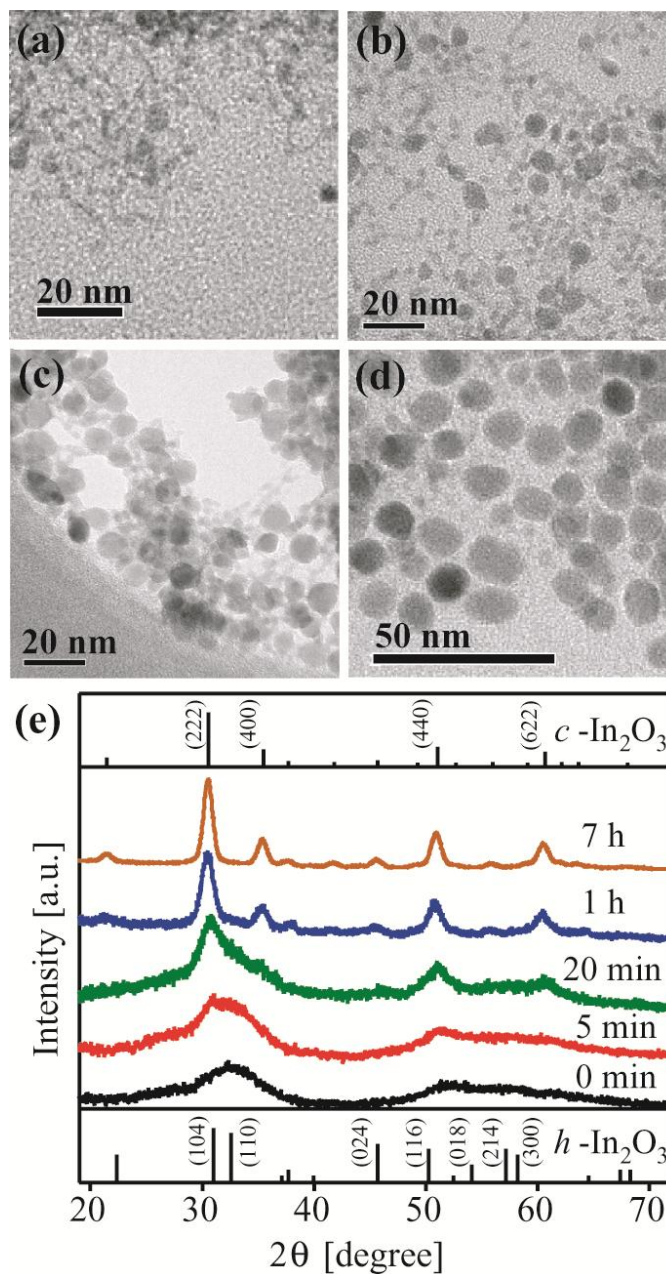
Figure 3.1 (a-d) TEM images of nanocrystalline In_2O_3 during the synthesis at 250° C: 0 (a), 10 (b), 30 (c), and 60 min (d) upon reaching the reaction temperature. (e) XRD patterns of In_2O_3 at different times during the synthesis at 250° C. Vertical lines at the top and bottom represent the patterns of bulk bixbyite bcc-In_2O_3 (JCPDS 06-0416) and rh-In_2O_3 (JCPDS 21-0406), respectively, with major reflections assigned.

The XRD pattern of the initially formed thin-walled networks is in good agreement with that of bulk rh-In_2O_3. As the reaction proceeds, the peaks corresponding to bcc-In_2O_3 become apparent. These peaks are significantly narrower than the peaks corresponding to rh-In_2O_3, indicating that the change in NC structure from rhombohedral to cubic accompanies an increase in NC size. These observations strongly suggest that metastable rh-In_2O_3 is an intermediate structure in the formation of bcc-In_2O_3 during NC growth. Due to surface energy contribution to the phase transformation free energy (ΔG), the relative stability of different polymorphs can be reversed at small grain sizes.[3, 85] Furthermore, for a NC with a small radius (R) the surface stress (g) is related to an average fractional decrease in atomic volume (Ω_0):

$$\frac{\Delta \Omega}{\Omega_0} = \beta \frac{2g}{R}$$
Equation 6

where β is the isothermal bulk compressibility.[86] This reduction in volume is equivalent to an excess pressure which favors the stabilization of higher density rh-In_2O_3 (63.22 and 64.89 Å^3 per In_2O_3 unit for rh- and bcc-In_2O_3, respectively).[5] Given the relatively small ΔG between rh- and bcc-In_2O_3,[5] surface stress could be a particularly important effect causing an excess pressure and favoring the stabilization of rh-In_2O_3 NCs due to a slightly higher density of corundum relative to cubic bixbyite phase .

3.1.2 Indium K-edge XAS Measurements: Evidence of Surface Stress

X-ray absorption spectroscopy can provide quantitative element-specific information about the local electronic structure environment, including surface sites,[87] and was used here to study the structure of In_2O_3 NCs in the process of phase transformation. The local environment of In^{3+} sites during the phase transformation of In_2O_3 NCs was systematically studied by In K-edge EXAFS method. Figure 3.2a shows Fourier-filtered EXAFS spectra of the sample synthesized at 250 ˚C, during the course of the reaction. These EXAFS spectra were derived for the In-O and In-In shells by the inverse Fourier transform of the pseudoradial functions (Figure 3.3) in the range R=1.15-3.37 Å.
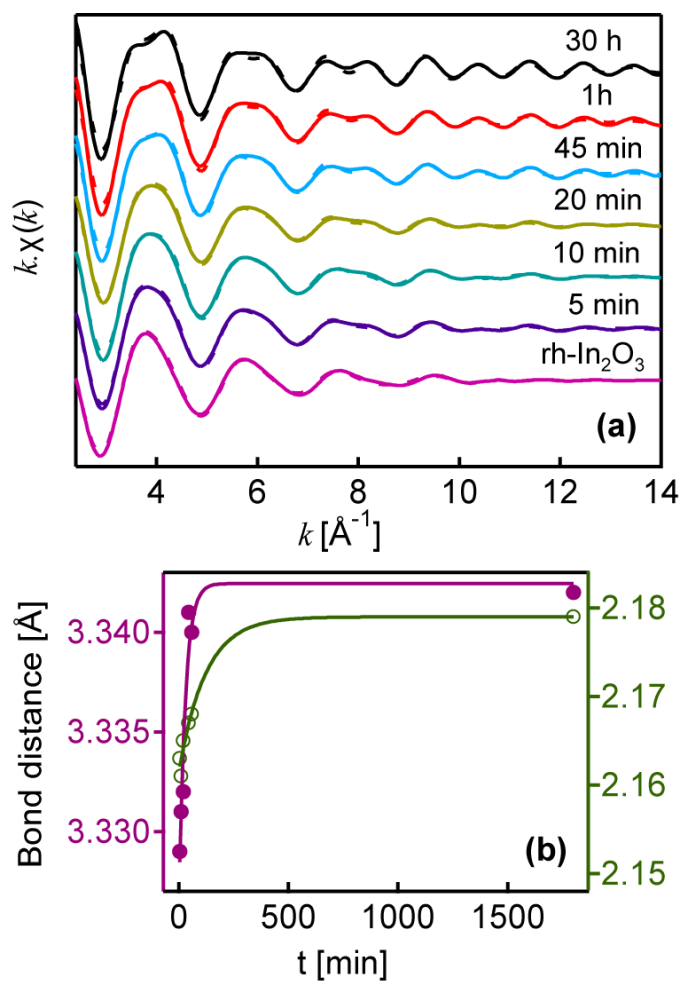
Figure 3.2 Fourier-filtered In K-edge EXAFS spectra of In_2O_3 NC samples synthesized at 250 ˚C (solid lines), and the resulting curve fits (dashed lines) used to calculate structural parameters. The reaction times corresponding to each spectrum are shown in the graph. (b) In-O (green) and In-In (purple) bond distances calculated from the EXAFS analysis for NCs synthesized for different reaction times.
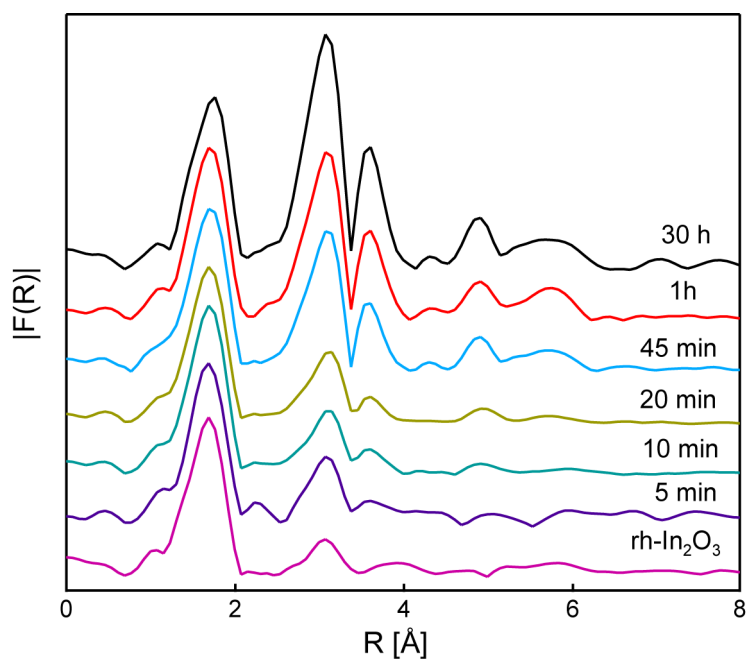
Figure 3.3 Fourier transform EXAFS spectra of In_2O_3 NCs synthesized at 250˚C for different reaction times. The sample synthesized at 200 ˚C for 30 h (purple) was used as a reference of pure rh-In_2O_3 NCs.

The structural parameters obtained from the fitting of the EXAFS spectra are summarized in Table 3.1. For bulk In_2O_3 the cation-anion distances are nearly identical in both dimorphs, and a small difference in density results from tighter packing of the anion layers in the corundum structure.[26] The average In-O bond length based on crystallographic data is 2.17-2.18 Å. In bulk rh-In_2O_3 the In-In distance is 3.243 Å with the second shell coordination number (CN) of 3, while in bulk bcc-In_2O_3 the In-In distance and CN are 3.35 Å and 6, respectively.[22, 26, 88] The average In-O and In-In bond distances for the samples isolated at different times during the synthesis are shown in Figure 3.2b.

Both In-O and In-In distances expand as the reaction proceeds. The increase in the average In-In distance can be attributed to the phase transformation from rh-In_2O_3 to bcc-In_2O_3, based on the bulk values of this parameter. This conclusion is supported by the change in the second shell (In-In) CN from 3.3 to 6 (Table 3.1).

Table 3.1 Fitting Parameters Determined from the Analysis of EXAFS Spectra of In_2O_3 NCs Synthesized at 250 ˚C.

	In-O			In-In$_1$			
t (min)	N	R (Å)	$\sigma^{2\,a}$ (Å^2)	N	R (Å)	σ^2 (Å^2)	ρ^b (%)
5	6.0	2.163±0.005	0.007	3.3	3.329±0.023	0.010	0.6
10	6.0	2.161±0.005	0.006	3.8	3.331±0.027	0.012	0.6
20	6.0	2.165±0.005	0.007	3.2	3.332±0.020	0.009	0.5
45	6.0	2.167±0.007	0.006	5.1	3.341±0.017	0.008	1.3
60	6.0	2.168±0.006	0.005	5.9	3.340±0.012	0.008	2.0
1800	6.0	2.179±0.007	0.006	6.0	3.342±0.009	0.005	2.5

[a] Debye-Waller factor. [b] Weighted residual factor(Refer to the experimental section 2.3.4.3).

However, In-O bond distance is much shorter in NCs at the beginning of the reaction than in bulk, and expands significantly in the early stage of NC growth. Over the course of the reaction the In-O bond distance reaches the value characteristic for the bulk In_2O_3. These results are consistent with an increase in surface stress with decreasing NC size, which is equivalent to an excess pressure, and compresses In-O bonds at NC surfaces. The increase in NC size with phase transformation reduces the surface stress and results in an expansion of In-O distances.

3.1.3 Formation of InOOH NCs

To verify the role of other intermediates in this single step procedure, we performed the reaction at lower temperatures. The formation of nanocrystalline InOOH at temperatures as low as 150 ˚C was observed in XRD patterns (Figure 3.4). The formation of InOOH has been signified as the key step in obtaining rh-In_2O_3 at ambient pressure.[31, 32, 47] The presence of $In(OH)_3$[47] or the absence of added water,[32] on the other hand, were suggested to prevent rh-In_2O_3 stabilization, although $In(OH)_3$ has been identified by other authors[17, 28] as a precursor from which both bcc-In_2O_3 and rh-In_2O_3 can form. Corundum-type In_2O_3 has not been observed or reported when $In(acac)_3$ was used as a precursor.[80] These discrepancies indicate a sensitivity of the obtained product to the reaction conditions and point out the importance of systematic studies of the In_2O_3 NC formation in solution. Here we used

In(acac)$_3$ precursor and showed that both rh- and bcc-In$_2$O$_3$ are derived from InOOH, which is formed by dehydration of In(OH)$_3$.
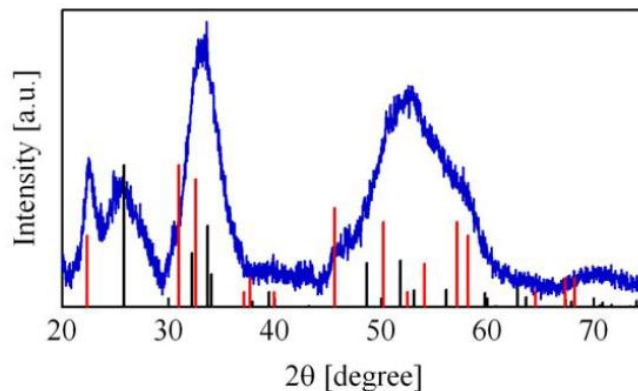
Figure 3.4 XRD pattern of the reaction mixture for the synthesis of In$_2$O$_3$ nanocrystals after heating at 150° C for 30 hours. Black lines represent the XRD pattern of bulk InOOH (JCPDS 71-2277) and red lines the XRD pattern of rh-In$_2$O$_3$ JCPDS (21-0406). Based on the reflection angles and peak intensities we conclude that the XRD pattern of the sample corresponds mostly to InOOH indicating its role as an intermediate in this synthesis. The XRD pattern of the sample also contains a contribution from nanocrystalline rh-In$_2$O$_3$ obtained by dehydration of InOOH.

Water-free synthesis in nonbasic organic solvents did not yield any NCs indicating that controlled presence of small amounts H$_2$O in oleylamine is needed for In(OH)$_3$ and InOOH formation by hydrolysis. Control experiments using In(NO$_3$)$_3$ precursor showed the same trend suggesting that In$_2$O$_3$ NCs are generally formed by hydrolysis mechanisms in solution phase preparations involving In^{3+} salt precursors.[89] Understanding the growth mechanism and the structural transformation should allow for the rational and controlled preparation of colloidal In$_2$O$_3$ NCs having specific sizes and structures by simply adjusting the reaction conditions, including temperature, precursors, solvents, coordinating ligands, and reaction time.

3.1.4 Optimized Reaction Conditions for the Synthesis High Purity rh-In$_2$O$_3$ and bcc-In$_2$O$_3$ NCs

We hypothesized that a rapid NC growth would lead to fast transformation of rh-In$_2$O$_3$, resulting in bcc-In$_2$O$_3$ NCs. A decrease in the growth rate would lead to formation of small NCs and the stabilization of rh-In$_2$O$_3$. Starting from this premise, we optimized the reaction temperatures and

times to selectively obtain high purity rh-In$_2$O$_3$ and bcc-In$_2$O$_3$ NCs while keeping all other parameters the same. Figure 3.5a shows a TEM image of In$_2$O$_3$ NCs synthesized at 200 ˚C for 30 h.
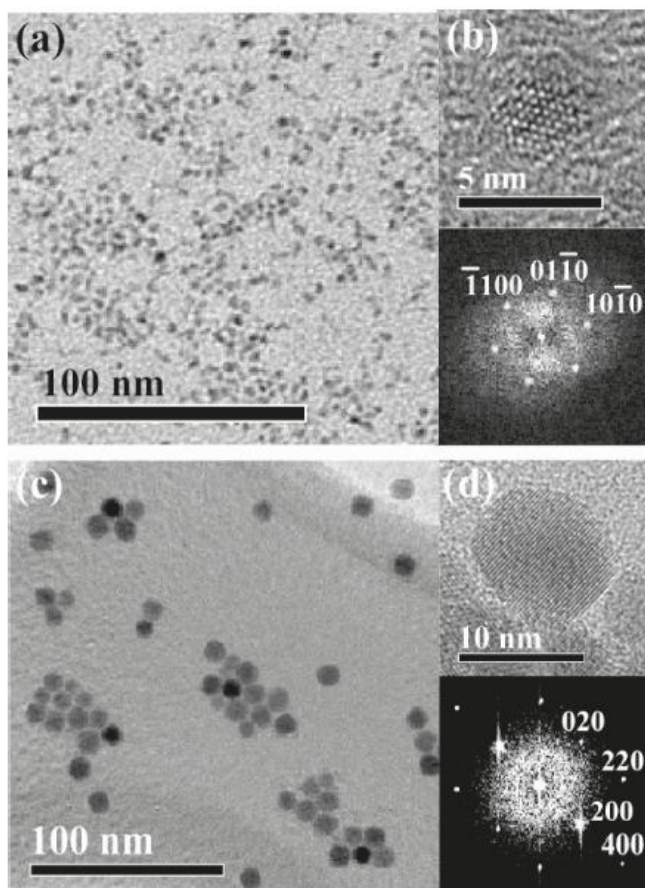
Figure 3.5 (a, c) Overview TEM images of (a) rh-In$_2$O$_3$NCs synthesized at 200 ˚C for 30 h, and (c) bcc-In$_2$O$_3$ NCs synthesized at 250 ˚C for 30 h. (b,d) Lattice-resolved TEM (top) and the corresponding FFT images (bottom) of (b) a single rh-In$_2$O$_3$, and (d) bcc-In$_2$O$_3$ NC.

Well-defined NCs having an average size of ca. 3.5 nm and the corundum-type crystal structure (XRD in Figure 3.6a, bottom) are observed. High-resolution TEM and the corresponding fast Fourier transform (FFT) images (Figure 3.5b) confirm the crystal structure at the single NC level. Figure 3.5c,d shows TEM images of a sample synthesized at 250 ˚C for 30 h. The resulting NCs have an average size of ca. 9.5 nm and cubic bixbyite-type structure, evidenced by TEM/FFT images (Figure 3.5c,d) and the XRD pattern (Figure 3.6a,top). The purity of the obtained NC phases was confirmed by Raman spectroscopy. The spectrum of NCs from Figure 3.5a shows the dominant peak characteristic for rh-In$_2$O$_3$ (Figure 3.6b, bottom), with no evidence of the presence of bcc-In$_2$O$_3$.

34

Raman spectrum of NCs from Figure 3.5c is in excellent agreement with that documented for the bixbyite phase,[90] suggesting purely bcc-In_2O_3 NCs (Figure 3.6b, top). The transformation of rh- to bcc-In_2O_3 NCs is determined by the NC growth kinetics. At 250 °C NCs grow rapidly and the transient rh-In_2O_3 could be isolated only after short times (Figure 3.1a,b).
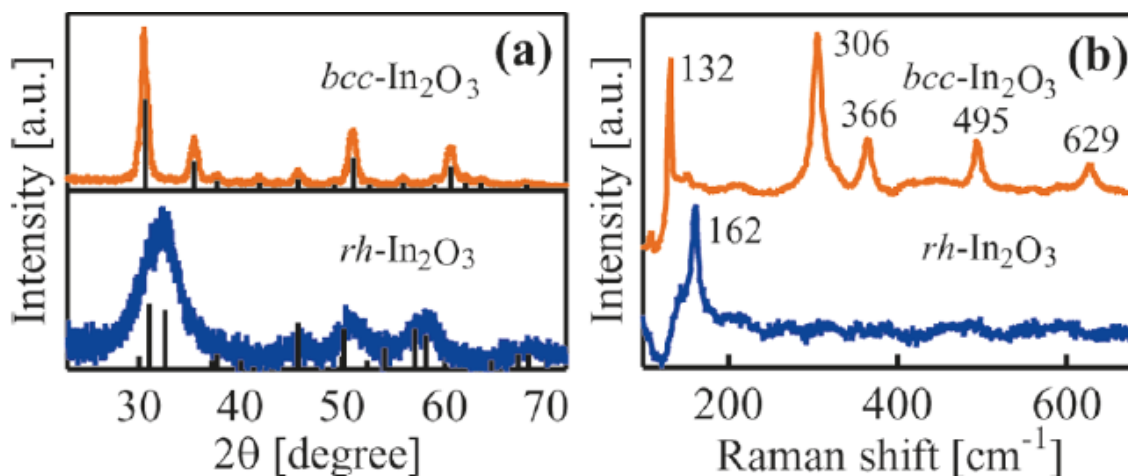
Figure 3.6 (a) XRD patterns of rh-In_2O_3 NCs synthesized at 200 °C for 30 h (bottom), and bcc-In_2O_3 NCs synthesized at 250 °C for 30 h (top). Black lines represent the XRD patterns of the corresponding bulk phases. (b) Raman spectra of rh-In_2O_3 (bottom) and bcc-In_2O_3 NCs (top).

Similarly, the addition of water, a reactant in hydrolysis, to the reaction mixture at 200 °C, which otherwise yielded only rh-In_2O_3 NCs, resulted in an increase in the NC growth rate and the formation of bcc-In_2O_3 NCs (Appendix A. 1).
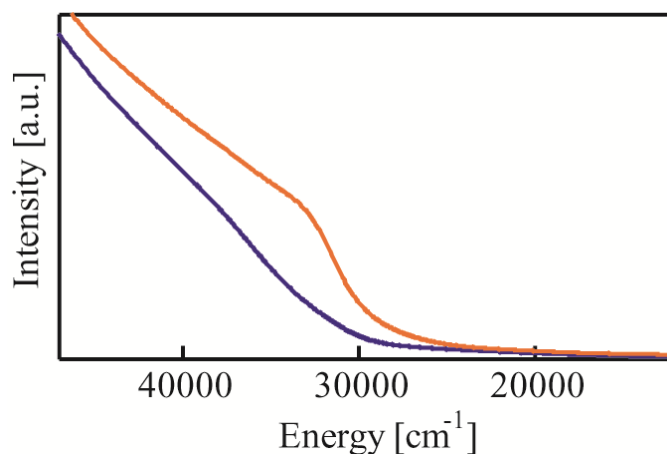
Figure 3.7 UV absorption spectra of 9.5 nm bcc-In_2O_3 (orange) and 3.5 nm rh-In_2O_3 NCs (blue), showing the band gap transitions.

35

In the methodology used in this work, the largest rh-In_2O_3 NCs that could be stabilized are ca. 5 nm, which can be compared to 6.5 GPa at 1250 ˚C needed to convert bulk bcc-In_2O_3 to rh-In_2O_3. The optical absorption spectra of these bcc- and rh-In_2O_3 NCs are shown in Figure 3.7. Strong transitions with the shoulder like maxima at ca. 32,500 and 37,500 cm^{-1} are observed for bcc-In_2O_3 and rh-In_2O_3 NCs, respectively. These transitions are assigned to the band gap absorptions. The blue shift in the rh-In_2O_3 NC band gap transition is suggestive of a strong quantum confinement.

3.2 A Kinetic Study of Phase Transformation of In_2O_3 NCs

3.2.1 Quantitative Analysis of the Kinetics of Phase Transformation of In_2O_3 NCs

Figure 3.8 shows XRD patterns and the corresponding NC size distribution histograms derived from the TEM images of the samples synthesized at 230 (a) and 260 ˚C (b) for different reaction times. Broadening of the XRD peaks is evident for short reaction times at both temperatures. For longer reaction times XRD peak broadening decreases, indicating an increase in the average NC size. From the TEM images of NCs synthesized at 230 ˚C (Figure 3.9), the average NC sizes immediately upon reaching the final temperature (0 min) and after 7 h of heating were determined to be ca. 2.5 and 7.3 nm, respectively. The increase in NC size occurs concurrently with a change in the crystal structure from rh-In_2O_3 to bcc-In_2O_3. For the reaction times up to 10 min only NCs smaller than 5 nm were observed, which are largely stabilized as rh-In_2O_3. On the other hand, the NC product isolated after 7 h has predominantly bcc-In_2O_3 structure. The XRD peaks of the sample synthesized at 260 ˚C (Figure 3.8b) indicate a mixture of the two crystal structures at the beginning of the reaction. In addition, the size distribution histogram at 0 min shows a bimodal NC size distribution, with small NCs having an average size of ca. 3.3 nm, and large NCs of ca. 5.6 nm. Increase in the reaction time results in an increase in the ratio of large-to-small NCs, and a more dominant presence of the bcc-In_2O_3 phase. After 1 h bcc-In_2O_3 NCs having an average size of ca. 8.2 nm were isolated. At both temperatures an increase in the reaction time causes an increase in the fraction of large NCs at the expense of the small ones. Faster NC growth at higher temperature is accompanied by an increase in the rate of phase transformation from rh-In_2O_3 to bcc-In_2O_3 phase.
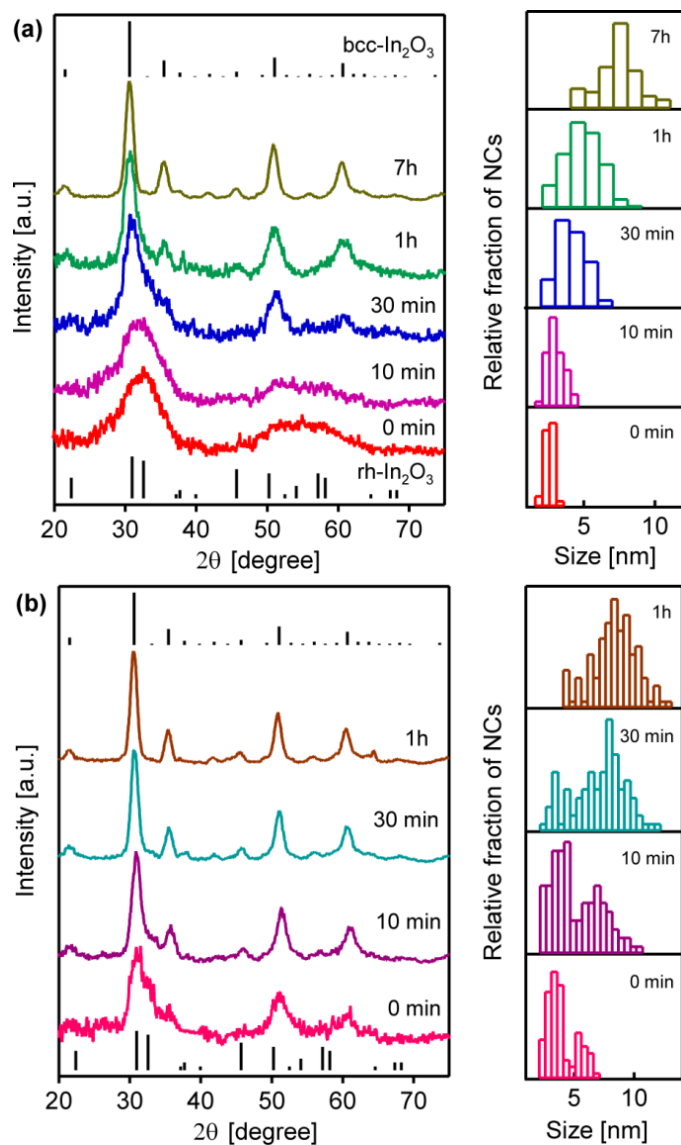
Figure 3.8 XRD patterns (left) and the corresponding size distribution histograms (right) of the samples synthesized at (a) 230 ˚C and (b) 260 ˚C for different reaction times (indicated in the graphs). The vertical lines are XRD peak positions of bulk rh-In_2O_3 (bottom, JCPDS 21-0406) and bcc-In_2O_3 (top, JCPDS 06-0416).
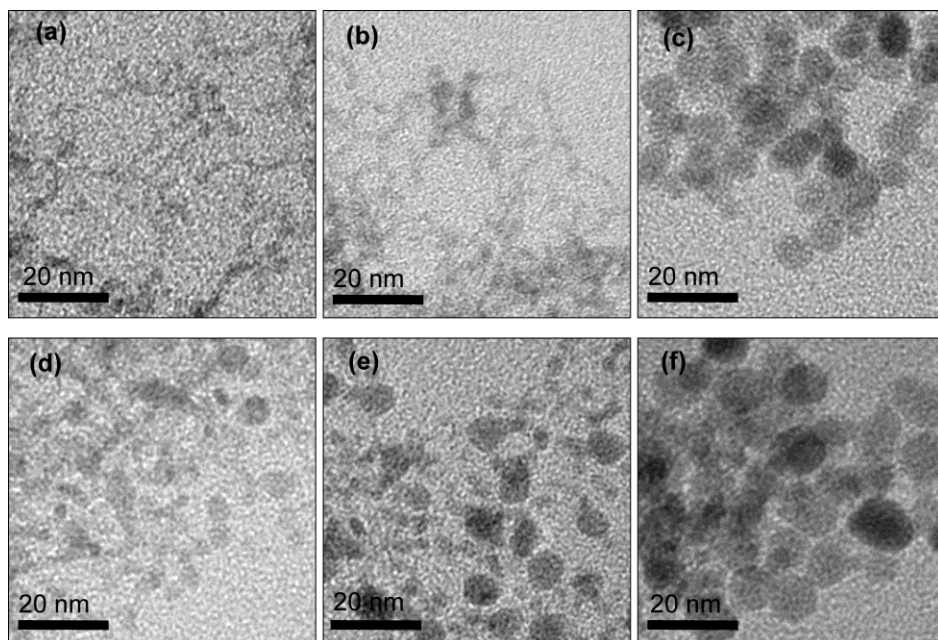
Figure 3.9 TEM images of In_2O_3 NC samples synthesized at (a-c) 230 $^\circ$C for 0 min (a), 10 min (b) and 7 h (c), and (d-f) 260 $^\circ$C for 0 min (d), 10 min (e) and 1 h (f).

The quantitative analysis of the kinetics of phase transformation was performed using the most pronounced XRD peaks in the region $2\theta\approx25$-$40°$. In this range the XRD patterns consist of a mixture of bcc-In_2O_3 (222) and (400), and rh-In_2O_3 (104) and (110) reflections. The deconvolution of the XRD peaks of the sample synthesized at 250 $^\circ$C for 20 min is shown in Figure 3.10a, as an example. The best fit to the experimental data in Figure 3.10a corresponds to 86 % rh-In_2O_3 and 14 % bcc-In_2O_3 phase.

The phase content determination was also performed by linear combination analysis using XRD patterns of pure phase NC samples. The linear combinations of the XRD patterns of the reference samples were well-matched with the experimental patterns obtained for the analogous mixtures of these references based on their weight percentage, justifying this complementary approach to the analysis of XRD data (Appendix A. 2).
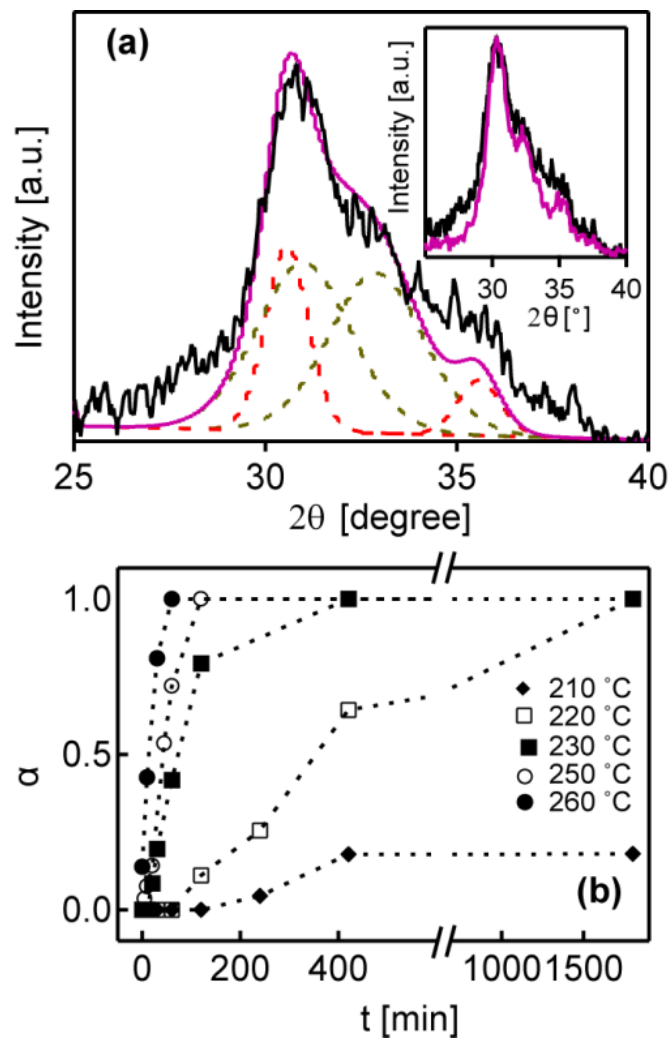
Figure 3.10 (a) Narrow-range XRD pattern of the sample synthesized at 250 ˚C for 20 min (solid black trace), and the deconvoluted (222) and (400) peaks of bcc-In_2O_3 (dashed red trace), and (104) and (110) peaks of rh-In_2O_3 (dashed olive trace). The pink trace is the superposition of the deconvoluted peaks. Inset: linear combination fitting (solid pink line) for the same XRD range. (b) Average content of bcc-In_2O_3 followed over 30 h for the reactions at different temperatures from 210 to 260 ˚C.
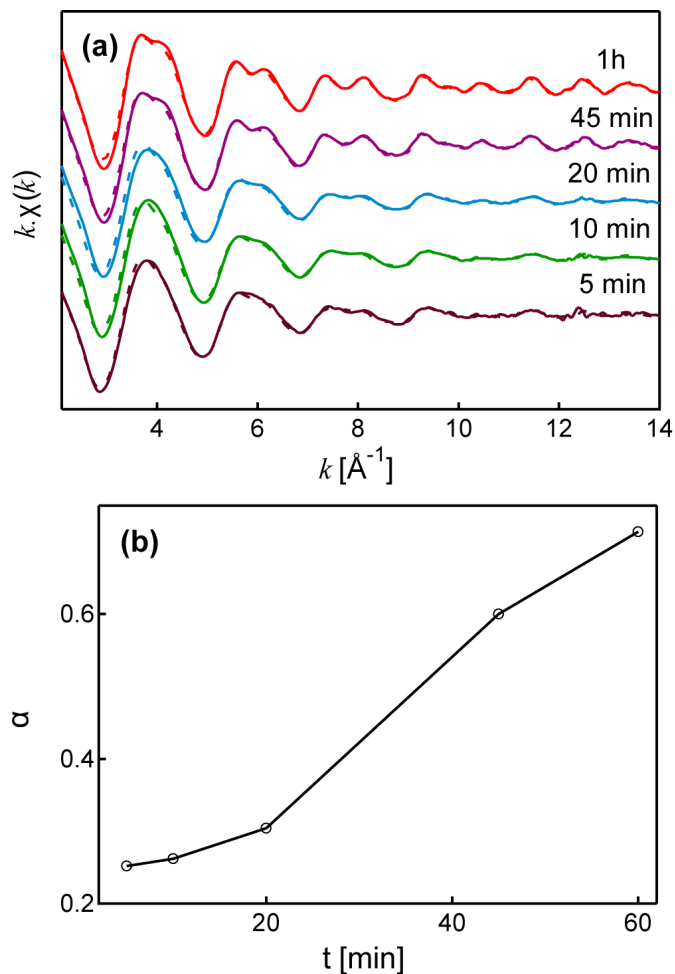
Figure 3.11 (a) EXAFS spectra of In_2O_3 NCs synthesized at 250°C for different reaction times (solid lines) and the best fit to the EXAFS spectra based on the linear combination of the rh-In_2O_3 and bcc-In_2O_3 NC references (dashed lines). (b) Content of the bcc-In_2O_3 phase for the samples in (a) determined by the EXAFS linear combination fitting.

The inset in Figure 3.10a shows the best linear combination fit for the same XRD data. The results of the peak deconvolution and linear combination were in a very good agreement for all samples, and the phase content for the kinetic analysis was derived as an average content from the two approaches. These phase content results were also confirmed by the EXAFS linear combination fitting (Figure 3.11). Figure 3.10b shows the content of bcc-In_2O_3 (α) over 30 h in the temperature range 210-260 °C.
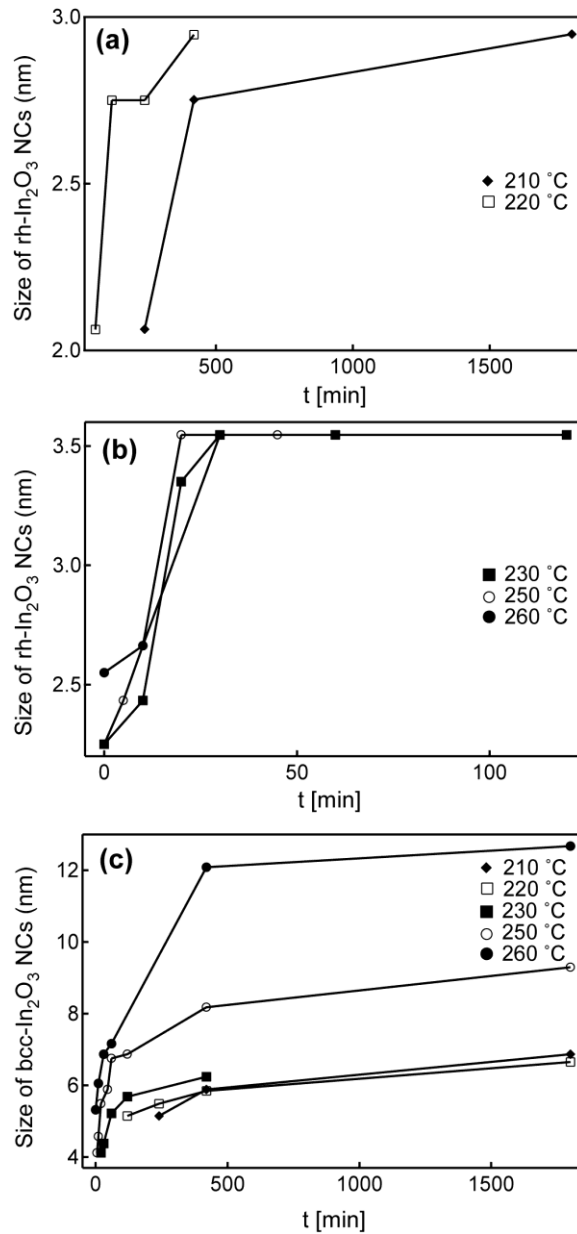
Figure 3.12 Sizes of In_2O_3 NCs at different reaction times: (a) rh-In_2O_3 NCs synthesized at 210 and 220 ˚C, (b) rh-In_2O_3 NCs synthesized at 230, 250 and 260 ˚C, and (c) bcc-In_2O_3 NCs synthesized in the temperature range 210-260 ˚C. The NC sizes were calculated based on the XRD peak deconvolution method.

The average sizes of rh-In_2O_3 and bcc-In_2O_3 NCs of the same samples, determined from the full width at half maximum (FWHM) of the peaks obtained by the deconvolution method, are shown in

41

Figure 3.12. A qualitative comparison of the kinetic behavior of NC growth and phase transformation reveals the same trend, indicating a correlation between these two processes.

3.2.2 Kinetics of Phase Transformation: JMAEK Model

The phase transformation kinetics was studied by a generic JMAEK model, which is frequently used to describe solid-state phase transformations.[33, 36] In this model the reaction progress (α) has a sigmoidal dependence on time,[33] as the reaction at first has a slow rate, followed by a faster one, and then slow again.[36] As a consequence there is a bell-shaped relationship between the reaction rate ($d\alpha/dt$) and α. The JMAEK equation can be written as:

$$-\ln(1-\alpha) = (kt)^n \hspace{3cm} \textbf{Equation 7}$$

where k is the rate constant of the reaction at time (t) and n is an exponent.[33] Figure 3.13 shows the rate of formation of the bcc-In_2O_3 phase as a function of α at various reaction temperatures. The bell-shaped functional forms are consistent with the sigmoidal α-t curves, and justify the use of JMAEK model.[33]
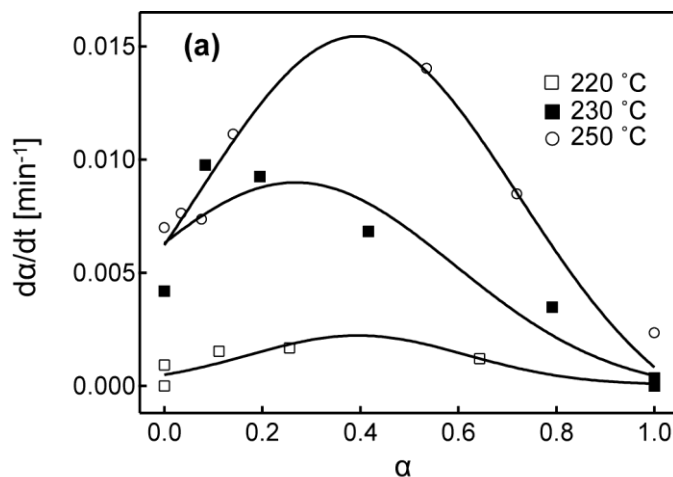
Figure 3.13 Rate of formation of the bcc-In_2O_3 phase as a function of α (phase content) at different reaction temperatures.

Figure 3.14a plots the phase content data for In_2O_3 NCs (the left hand side of Equation 7) as a function of time for five different temperatures.

42
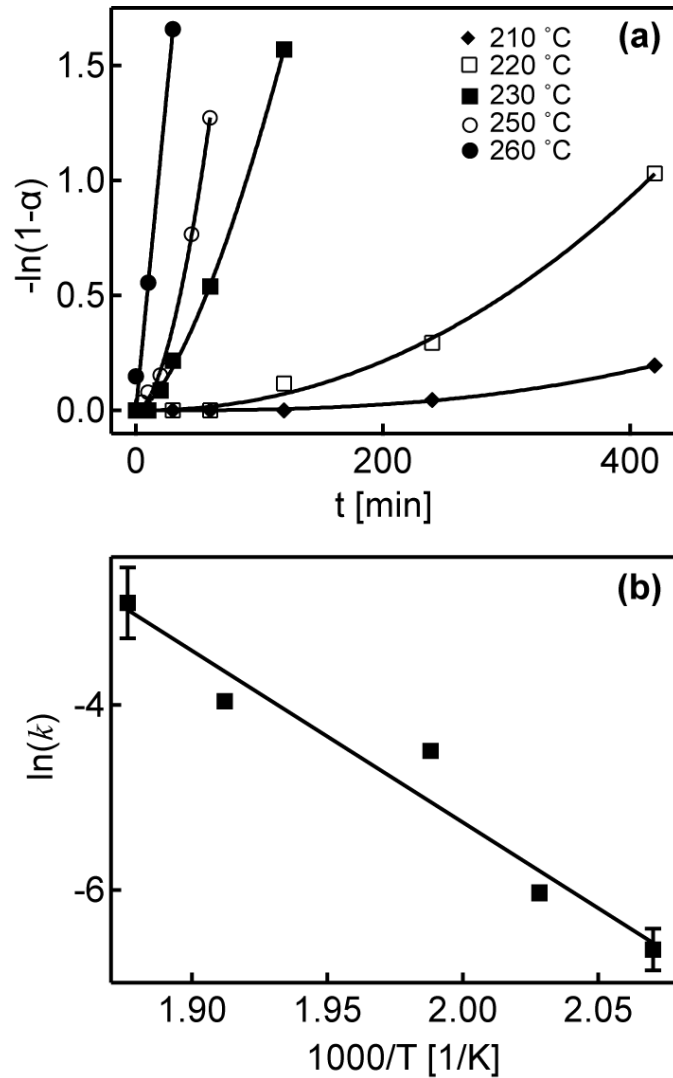
Figure 3.14 (a) JMAEK plots generated from the fraction of the bcc-In_2O_3 phase (α) present at different points in time in the samples synthesized at different temperatures. (b) Arrhenius plot based on the rate constants obtained from the JMAEK plot.

The data are well fit to JMAEK equation (solid black lines), with the rate constant k and the exponent n as adjustable parameters. The plots of $\ln[-\ln(1-\alpha)]$ versus $\ln(t)$ show linear behavior (Appendix A. 3), allowing for the extraction of the same parameters, and the confirmation of the obtained results. The values of the exponents and rate constants are summarized in Table 3.2.

43

Table 3.2 Values of *n* and *k* Obtained from the JMAEK Plot. The Standard deviation for *k* is shown as error bars in Figure 3.14b.

$T (˚C)$	n	$k (min^{-1})$
210	2.6	0.0013
220	1.7	0.0024
230	1.6	0.0112
250	1.4	0.0190
260	1.0	0.0552

   The exponent *n* decreases with increasing temperature from 2.6 to 1, in the studied temperature range (210-260 ˚C). According to the nuclei growth models *n* is a function of the geometry of nuclei (dimensional factor) and the nucleation probability (nucleation factor).[37] Non-integer values of *n* in the range of 1.5-2.5 have been attributed to the diffusion-controlled mechanism for three-dimensional (quasi-spherical particle) growth, with decreasing nucleation rate over the course of the reaction.[34, 35] Lower *n* values are characteristic for the zero nucleation rate mechanism, or a process in which all nucleation events occur very rapidly at the initial stage, followed by the nuclei growth. In the context of these considerations the *n* values calculated in this study suggest that the nucleation of bcc-In$_2$O$_3$ phase occurs uniformly on quasi-spherical rh-In$_2$O$_3$ NCs, and that the nucleation rate reaches a maximum at the beginning of the reaction and decreases as the reaction progresses. In the low temperature regime (i.e. below ca. 230 °C) the nucleation rate of bcc-In$_2$O$_3$ decreases gradually throughout the course of the synthesis, concurrently with the growth of the nucleated bcc-In$_2$O$_3$ phase. At temperatures above ca. 230 °C the rate of bcc-In$_2$O$_3$ nucleation drops very rapidly after initial nuclei formation, and the mechanism of phase transformation is governed only by the growth of the new phase in the course of the reaction. The kinetics of phase transformation is correlated with the NC size (or the kinetics of NC growth), as evident from the size distribution histograms (Figure 3.8). It is very likely that defect sites at NC surfaces play a key role in the phase transformation process, due to their lower reaction activation energies.[33] The activation energy (E_a) of the rh- to bcc-In$_2$O$_3$ NC phase transformation can be determined from the calculated rate constant values for different temperatures, using the Arrhenius equation:

$$k = Ae^{-E_a / RT}$$ **Equation 8**

where A is the pre-exponential factor and R is the gas constant. The plot of $\ln(k)$ versus $1/T$ (Figure 3.14b) gives a value of 153±20 kJ/mol for the activation energy of the phase transformation in In_2O_3 NCs.

Although the JMAEK model is applicable to many solid-state reactions, it is based on the assumption that samples have infinite sizes in addition to randomly distributed nucleation sites.[39, 40] However, studies of phase transformation of TiO_2 polymorphs have revealed a strong dependence of the phase transformation rate on the grain size.[44, 45] Furthermore, the nucleation mechanism responsible for the formation of a new phase is dependent on temperature and the nature of the sample. Therefore, for detailed understanding of the phase transformation mechanism of nanocrystalline materials, which are finite in size, more precise models are needed. The choice of the suitable model often requires complementary structural information, particularly due to the fact that different models can often be fit to the same set of kinetic data.[42, 43]

3.2.3 Kinetics of Phase Transformation: Interface and Surface Nucleation Model

High-resolution TEM (HRTEM) images of In_2O_3 NCs at different reaction times during the synthesis at 230 ˚C are shown in Figure 3.15. Upon reaching 230 ˚C the aliquots from the reaction mixture were removed and dispersed in toluene without any further treatment. The HRTEM image of the sample collected immediately upon reaching the reaction temperature (Figure 3.15a) shows that the sample has a network (polymer-like) morphology, which relatively quickly transforms into well-defined NCs with rh-In_2O_3 crystal structure. As the reaction continues rh-In_2O_3 NCs begin to interact, forming particle-particle interfaces (Figure 3.15b). At later stages of the reaction the interacting NCs completely merge (Figure 3.15c) and eventually transform from elliptical to faceted quasi-spherical shape (Figure 3.15d). The process of NC interactions, observed by HRTEM, is accompanied by the transformation from rh-In_2O_3 to bcc-In_2O_3 phase, as demonstrated in Figure 3.8. Furthermore, the measured lattice spacing of NCs in Figure 3.15b, c and d (d≈ 2.92 Å) corresponds to (222) plane of bcc-In_2O_3 phase.
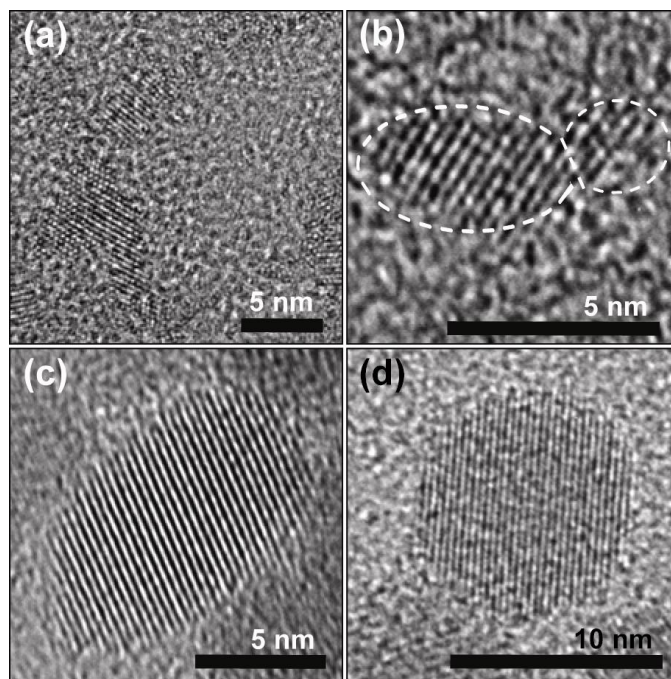
Figure 3.15 HRTEM images of In_2O_3 NCs synthesized at 230 ˚C for (a) 0 min, (b) 10 min, (c) 1 h and (d) 7 h. The boundaries of NCs in (b) are indicated with dashed line for clarity.

To account for the role of surfaces and interfaces in nanocrystalline TiO_2 anatase to rutile phase transformation, the surface and interface nucleation kinetic models have been developed.[41, 45, 46] Which of the two mechanisms prevails depends largely on the concentration of particles.[41] For low-density particle packing high free surface area is available, and the surface nucleation is a dominant mechanism. As the density of particle packing increases the rate of interface nucleation at particle-particle contacts increases relative to the rate of surface nucleation. Smaller particles which have a larger number of particle-particle contacts per unit volume exhibit higher interface nucleation rate. The rate of phase transformation for the interface nucleation model is therefore ultimately determined by the probability of the contact formation between two particles.[41] Investigation of the size dependence of phase transformation of TiO_2 polymorphs using the interface nucleation model shows that the activation energy changes very slightly with particle size, but the pre-exponential factor increases significantly with decreasing particle size.[45] The activation energy for interface nucleation is generally lower than that for surface nucleation. For example, for anatase TiO_2 particles having an average size of 7.9 nm, E_a values for interface and surface nucleation are 167 and 466 kJ/mol, respectively, for the temperature range 620-690 ˚C.[41]

46

Based on the TEM images showing particle contact formation (Figure 3.15), we examined the kinetics of NC phase transformation in the framework of the interface nucleation model. The interface nucleation model for the kinetics of phase transformation can be expressed as:

$$\frac{(D_{rh}/D_0)^3}{(1-\alpha)} - 1 = (k_{IN}N_0)t \qquad \textbf{Equation 9}$$

where D_{rh} is the average diameter of rh-In_2O_3 NCs (Figure 3.12), α is the fraction of bcc-In_2O_3 phase (*vide supra*), and k_{IN} is the kinetic constant for interface nucleation. N_0 and D_0 are the initial number and average diameter of rh-In_2O_3 NCs, respectively. Figure 3.16a shows the linear fit of the interface nucleation model to the experimental data for the phase transformation of rh-In_2O_3 to bcc-In_2O_3 NCs.
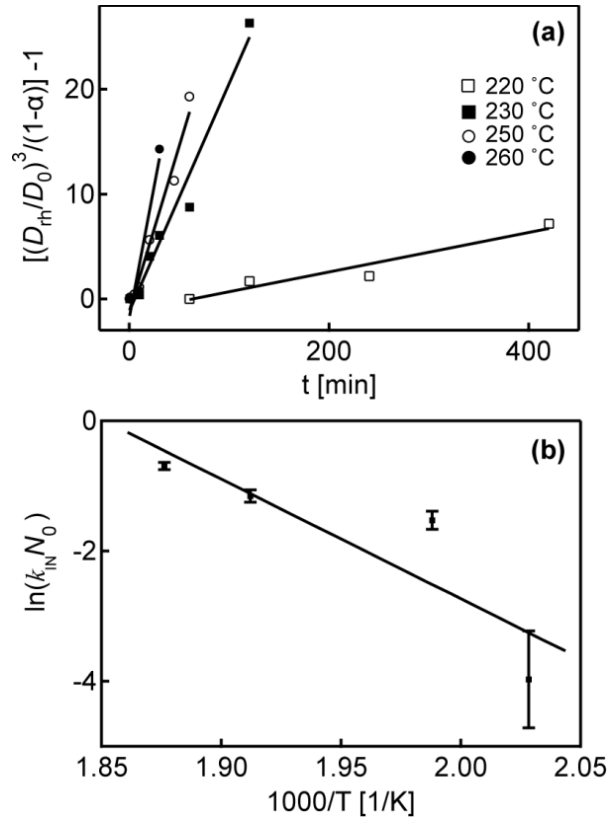
Figure 3.16 (a) Kinetic plots based on the interface nucleation model, generated from the fraction of the bcc-In_2O_3 phase (α) present at different points in time in the samples synthesized at different temperatures. (b) Arrhenius plot based on the rate constants (k_{IN}) obtained from the interface nucleation plot in (a).

The values of k_{IN} obtained as fitting parameters for different temperatures are given in Table 3.3.

Table 3.3 Values of $k_{IN}N_0$ obtained from the interface nucleation plot. The Standard deviation for $k_{IN}N_0$ is shown as error bars in Figure 3.16b.

T (˚C)	$k_{IN}N_0$ (min^{-1})
220	0.0087
230	0.0371
250	0.3321
260	0.2921

The activation energy of the interface nucleation mechanism (E_{aIN}) was determined to be 152±60 kJ/mol from the Arrhenius fitting of $\ln(k_{IN}N_0)$ vs $1/T$ dependence (Figure 3.16b). This value is in good agreement with the activation energy calculated using the JMAEK model, and is close to the values obtained for the anatase to rutile TiO_2 phase transformation.[41, 91]

3.2.4 The Choice of Suitable Kinetic Model

Typically, the mechanism of a solid state process is inferred by determining which model provides the best fit to the experimental kinetic data (model-fitting approach). Although each kinetic model is related to the specific type of process, it is often possible to apply more than one model to fit the experimental results. For isothermal solid-state processes different models can be fit to the same experimental data and used to calculate the activation energy,[42, 43] allowing for deeper analysis of the role of different parameters in a given process. Consequently, the choice of the most suitable model should be supported by other complementary structural techniques. Electron microscopy imaging in conjunction with the interface nucleation model analysis suggests that phase transformation of colloidal In_2O_3 NCs occurs by the formation of interfaces between metastable rh-In_2O_3 NCs stabilized in an early stage of the reaction. According to this interface nucleation model, the transformation rate is determined by the nucleation of bcc-In_2O_3 at the interface of two contacting rh-In_2O_3 NCs. The nucleation of bcc-In_2O_3 phase occurs rapidly at the beginning of the reaction, and the nucleation rate decreases as the reaction progresses and the concentration of small rh-In_2O_3 NCs diminishes. Higher reaction temperature enhances the probability of NC contact formation in addition to their growth, increasing the phase transformation rate (Figure 3.17a). At high reaction temperatures (above 250 °C) the phase transformation is completed within a short period of time, due to the rapid decrease in the

number of small NCs. The NC size distribution results (Figure 3.8) support the conclusion that the fraction of small NCs in the reaction mixture decreases more dramatically at higher reaction temperatures. An increase in the concentration of rh-In_2O_3 NCs also leads to an increase in the number of particle-particle contacts per unit volume, which speeds up the rate of the phase transformation (Figure 3.17b).
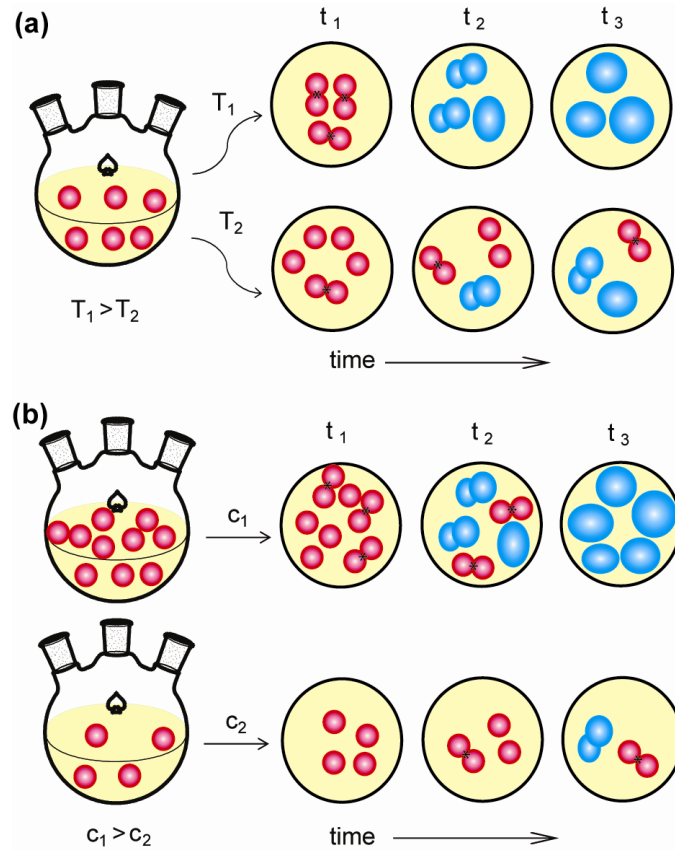
Figure 3.17 Schematic representation of the influence of (a) temperature (T) and (b) NC concentration (c) on the rate of phase transformation of In_2O_3 NCs by the interface nucleation mechanism. Red and blue spheres indicate rh-In_2O_3 and bcc-In_2O_3 NCs, respectively, and asterisks (*) indicate interface nucleation sites. The phase transformation rate is determined by the probability of contact formation between rh-In_2O_3 NCs.

   Importantly, all NCs imaged by TEM exhibit only a single phase, without multiple domains or phase boundaries, indicating a very fast propagation of bcc-In_2O_3 phase upon nucleation, which is consistent with recent theoretical investigations.[92] The nucleation of the bcc-In_2O_3 phase is most likely initiated by the interfacial defect sites. The similarity of the activation energy of phase

transformation of TiO_2 nanocrystalline powder and colloidal In_2O_3 NCs suggests that the nucleation of a thermodynamically stable phase in TCO NCs is determined by the interactions at a local or molecular level (which should be similar for TCO NCs), rather than by macroscopic property of a material.

3.2.5 *In situ* Nonisothermal X-ray Diffraction Analysis

To further study the effect of NC size on the phase transformation of In_2O_3 we performed *in situ* nonisothermal XRD analysis. For these measurements the samples having different NC sizes were prepared, precipitated and dried in the air. The resulting powder was heated in the X-ray diffractometer to different temperatures from 240 to 350 °C, and the XRD patterns were collected at each temperature. Figure 3.18a shows *in situ* XRD patterns of the sample prepared by the colloidal method at 150 °C for 30 h. At the initial temperature of 240 °C, the NCs have corundum crystal structure and an average size of ca. 3 nm. Heating the sample at higher temperatures decreases the broadening of the XRD peaks, attesting to an increase in NC size, and induces a gradual phase transformation to bcc-In_2O_3 NCs. At 350 °C the cubic bixbyite phase becomes dominant. *In situ* phase transformation of larger rh-In_2O_3 NCs, which were synthesized in ethanol by the alcoholysis method,[17] is shown in Figure 3.18b. These rh-In_2O_3 NCs have an average size of ca. 5 nm at 240 °C, as calculated from the XRD peak broadening, although the sample contains some nanocrystalline InOOH intermediate.[17] Unlike smaller NCs in Figure 3.18a, this sample retains rh-In_2O_3 structure throughout the studied temperature range (up to 350 °C), although NCs clearly increase in size during *in situ* heating. A comparison between the nonisothermal XRD results in Figure 3.18a and b suggests that the phase transformation rate is faster and requires less thermal energy for smaller NCs. This observation contrasts thermodynamic effects on the phase stabilization of NCs. Thermodynamically, a decrease in size of In_2O_3 NCs leads to increased stabilization of rh-In_2O_3 phase, owing to the surface energy and/or surface stress contributions. The excess pressure caused by the surface stress increases with decreasing NC size, demanding more thermal energy to break and rearrange bonds in order to nucleate a new phase at NC surfaces.[45] An increase in the activation energy with decreasing NC size has been reported for the phase transformation of TiO_2 polymorphs.[45] The discrepancy between these thermodynamic predictions and the results of Figure 3.18 can be explained assuming that at low temperatures and for small initial NC sizes the dominant phase transformation mechanism is the interface nucleation, as discussed above. Smaller NCs have higher packing density relative to the

larger ones, which increases the probability of particle-particle interactions and speeds up the phase transformation rate.
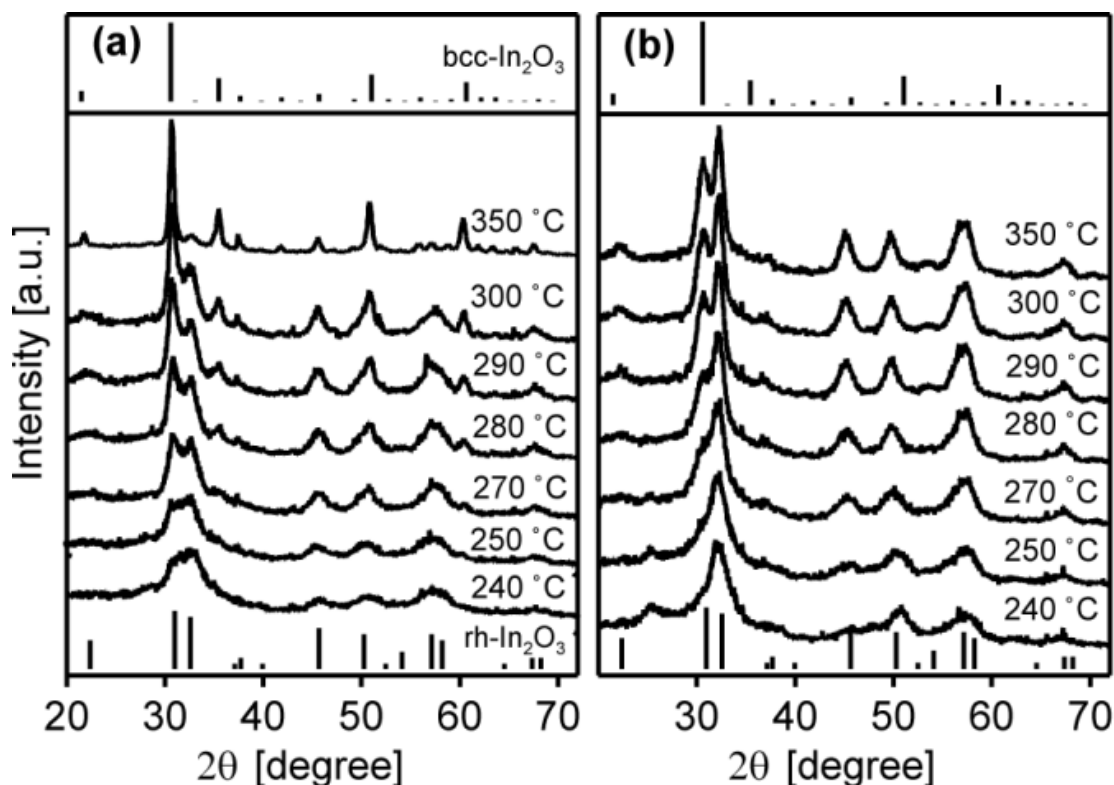
Figure 3.18 *In situ* variable-temperature XRD patterns of In$_2$O$_3$ NCs synthesized by (a) colloidal method at 150 ˚C for 30 h, and (b) alcoholysis method in ethanol. Both samples were preheated at 240 ˚C in the diffractometer. The vertical lines are XRD peak positions of bulk rh-In$_2$O$_3$ (bottom, JCPDS 21-0406) and bcc-In$_2$O$_3$ (top, JCPDS 06-0416).

Although metastable rh-In$_2$O$_3$ phase is thermodynamically stabilized in NCs below ca. 5 nm in size, the phase transformation is kinetically controlled by the interface nucleation mechanism (i.e. probability of NC interaction), allowing smaller NCs to undergo phase transformation faster and at lower temperatures relative to larger NCs. Phase transformation under nonisothermal conditions was also studied in the solution phase by recording XRD patterns of the precipitated aliquots as the reaction mixture is heated at a rate of 1 °C/minute (Figure 3.19).
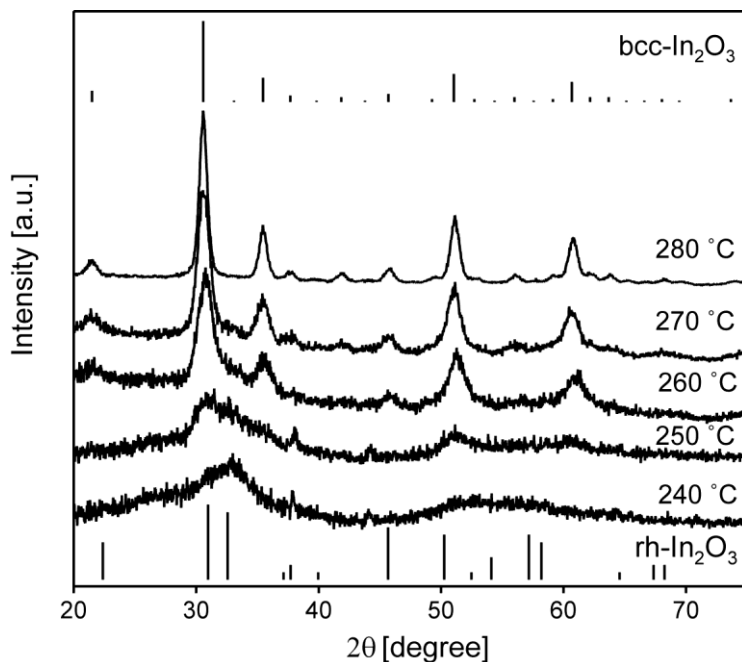
Figure 3.19 XRD patterns of In_2O_3 NCs synthesized under nonisothermal conditions, with the heating rate of 1 °C/min. The aliquots of the sample were taken upon reaching the desired temperatures indicated in the graph.

Comparison with *in situ* XRD measurements of powder samples showed in Figure 3.18a reveals that the phase transformation of In_2O_3 NCs in solution occurs at a lower temperature and a faster rate. This difference may be a consequence of increased probability of NC contact formation in solution, owing to their mobility. The synthesis and processing conditions may modify NC interactions and change the thermal energy of the phase transformation.

Chapter 4

Dopant-Induced Manipulation of the Growth and Structural Metastability of Colloidal Indium Oxide NCs

This chapter explores the effect of dopant ions on the growth and structure of colloidal In_2O_3 NCs, and factors governing the dopant incorporation during NC growth. Cr_2O_3 with the corundum-and Mn_2O_3 with the bixbyite-type crystal structure are isostructural with rh-In_2O_3 and bcc-In_2O_3, respectively. The isostructural nature of Cr_2O_3 and Mn_2O_3 with one of the polymorphs of In_2O_3, and the simpler phase transition mechanism in NCs compared to their bulk counterparts motivated us to study the effect of Mn^{3+} and Cr^{3+} dopants on the growth and structural metastability of In_2O_3 NCs, and study the mechanism of dopant incorporation.

4.1 Changes in the In_2O_3 NCs Structure and Size in the Presence of Dopant

TEM images and the corresponding size distribution histograms of Mn^{3+}-doped In_2O_3 ($Mn^{3+}:In_2O_3$) NCs synthesized at 250 °C for 1h with different concentrations of Mn^{3+} precursor are shown in Figure 4.1.

The starting molar ratio of $Mn(acac)_3$ to $In(acac)_3$ ([Mn]/[In]) was varied from 0 to 0.15. Pure In_2O_3 NCs have the average diameter of 8.6 nm and a relatively narrow size distribution (Figure 4.1a). With [Mn]/[In]=0.05, the NC sizes and their distribution become dramatically different (Figure 4.1b). Bimodal size distribution is observed, with small NCs having an average size of ca. 4 nm, and large NCs of ca. 8.5 nm. Further increase in the concentration of Mn^{3+} precursor leads to an increase in the fraction of small NCs at the expense of the large ones (Figure 4.1c). At [Mn]/[In]=0.15 only the NCs with an average size of ~4.5 nm are observed (Figure 4.1d). The reduction in the NC size due to an increase in the dopant precursor concentration is accompanied by the change in In_2O_3 crystal structure (Figure 4.2). The XRD pattern of pure In_2O_3 NCs shows a bixbyite-type structure. As the fraction of small NCs increases, the formation of corundum-type In_2O_3 becomes evident in XRD patterns. The decrease in the NC size also leads to broadening of the XRD peaks for samples synthesized with [Mn]/[In] of 0.10 and 0.15.
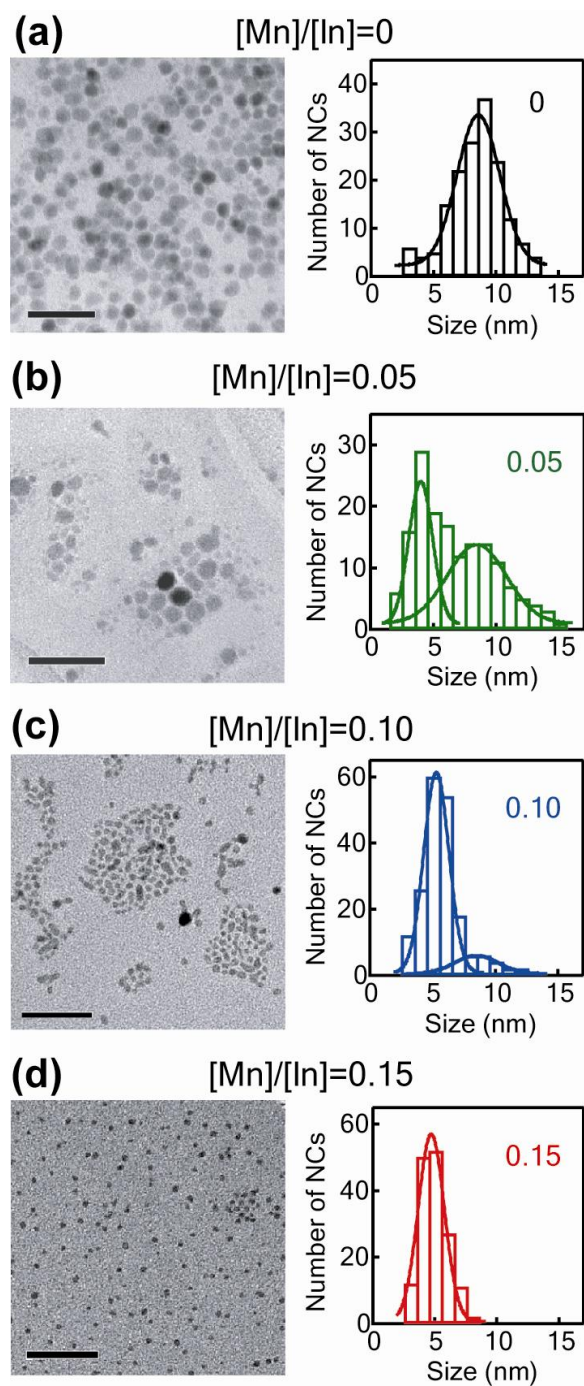
Figure 4.1 TEM images (left) and size distribution histograms (right) of Mn^{3+}-doped In_2O_3 nanocrystals synthesized with Mn vs In precursor molar ratios ([Mn]/[In]) of 0 (a), 0.05 (b), 0.10 (c), and 0.15 (d). The lines in histograms are Gaussian fits. Scale bars in TEM images are 50 nm.
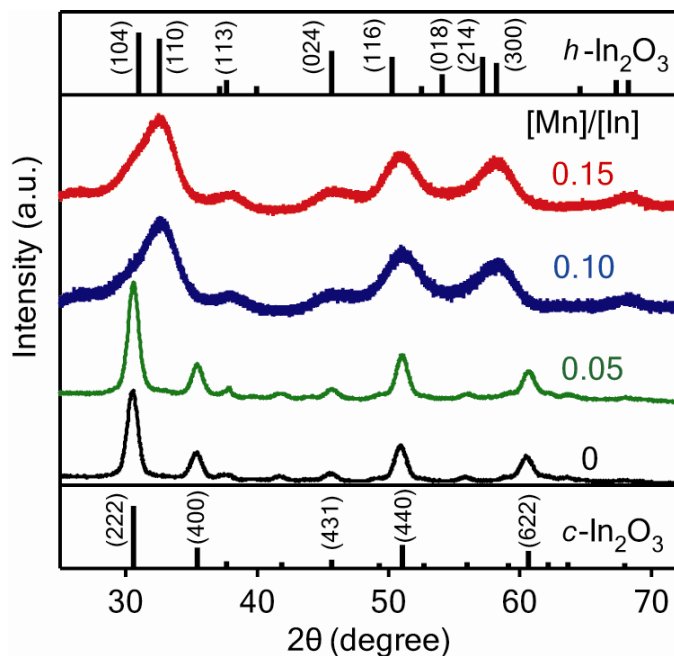
Figure 4.2 XRD patterns of Mn^{3+}-doped In_2O_3 nanocrystals in Figure 4.1 synthesized with different Mn vs In precursor molar ratios ([Mn]/[In]). The black lines are the patterns of bulk bcc-In_2O_3 (bottom, JCPDS 06-0416) and rh-In_2O_3 (top, JCPDS 21-0406) with major reflections assigned.

The same trends were observed for Cr^{3+}-doped In_2O_3 (Cr^{3+}:In_2O_3) NCs. Figure 4.3 shows TEM images of Cr^{3+}:In_2O_3 NCs synthesized at 250 °C for 1h with different ratios of chromium and indium precursor concentrations ([Cr]/[In]) in the reaction mixtures and the corresponding size distribution histograms. The staring dopant concentration varied from 0.05 to 0.20. As the starting concentration of Cr^{3+} increases with respect to In^{3+}, the ratio of small to large NCs increases and the NCs size distribution shifts to smaller sizes. At [Cr]/[In]=0.2 the population of large NCs completely disappears, and the average NC size is only ca. 3 nm.
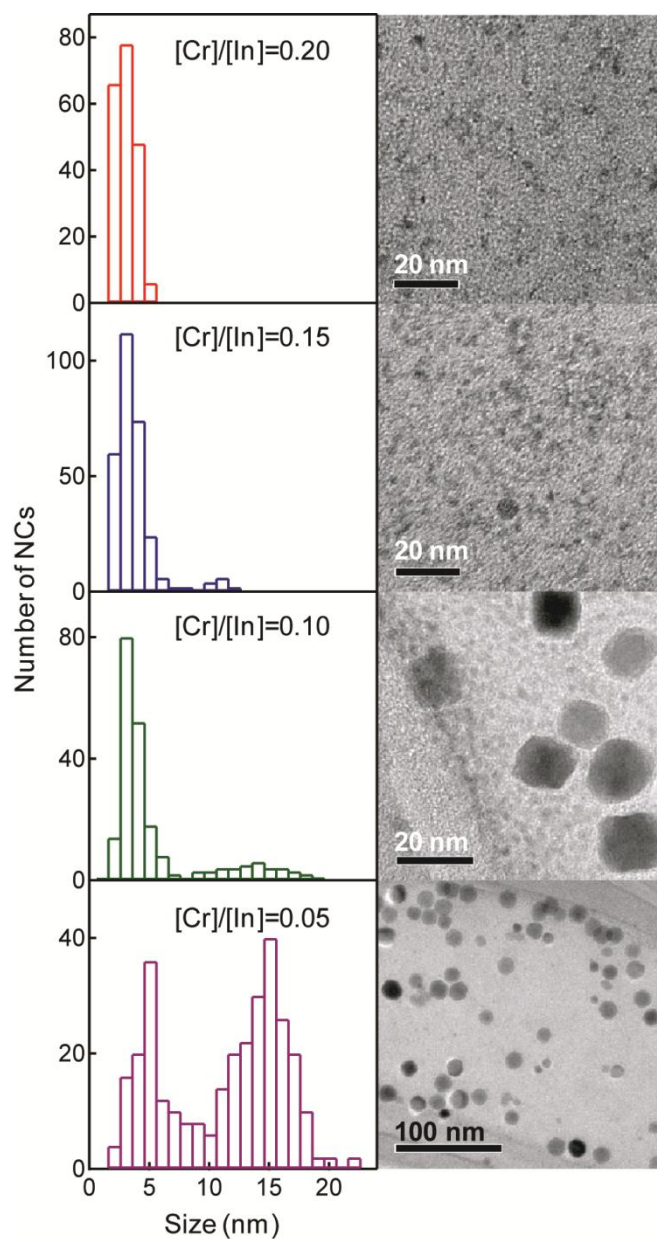
Figure 4.3 TEM images (right) and the corresponding size distribution histograms (left) of Cr^{3+}:In_2O_3 synthesized with different ratios of chromium and indium precursor concentrations.

XRD patterns corresponding to the samples in Figure 4.3 are shown in Figure 4.4. All XRD peaks of Cr^{3+}:In_2O_3 NCs prepared with [Cr]/[In]=0.05 (purple trace) match those of bulk bcc-In_2O_3 (black lines, JCPDS 06-0416).
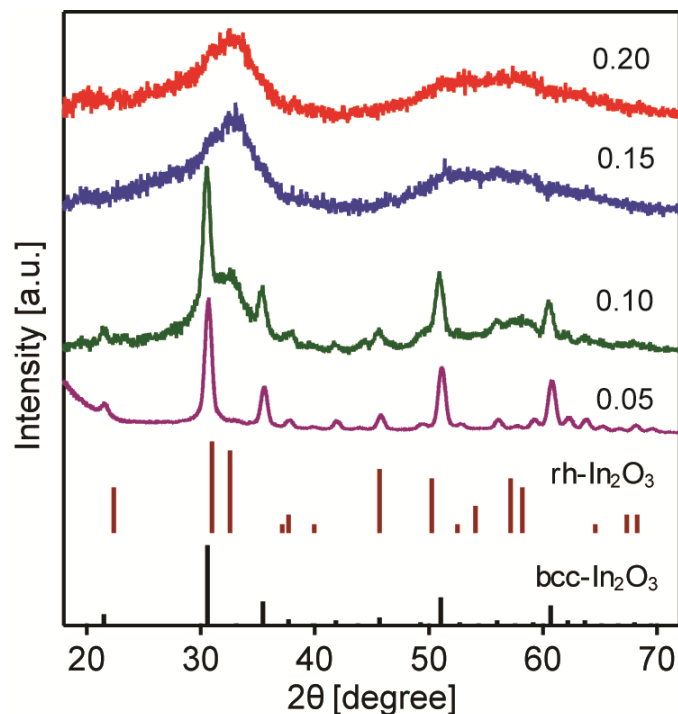
Figure 4.4 XRD patterns of Cr^{3+}:In_2O_3 synthesized with different ratios of chromium and indium precursor concentrations ([Cr]/[In]). The vertical lines are XRD peak positions of bulk bcc-In_2O_3 (black) and rh-In_2O_3 (brown).

As the concentration of the Cr^{3+} precursor increases the peaks corresponding to rh-In_2O_3 (brown lines, JCPDS 21-0406) appear. For the starting precursor mixture of [Cr]/[In]=0.10 (green trace) broad peaks centered at ca. 32.5 and 58 degrees are readily assigned to (110) and (214)/(300) reflections, respectively, of rh-In_2O_3, and at [Cr]/[In]=0.20 (red trace) only the NCs with corundum crystal structure are present. A large broadening of the XRD peaks with increasing Cr^{3+} precursor concentration is indicative of a strong reduction in NC size, and is consistent with the change in the NC size distribution observed in TEM images for increasing dopant precursor concentration.

To further explore the change in nanocrystal structure in the presence of dopant ions, we performed high-resolution TEM studies (Figure 4.5a-d). In all samples studied, the vast majority of NCs smaller than 5 nm have corundum crystal structure, while those larger particles have cubic crystal structure, indicating that the critical size for NC transformation is ca. 5 nm.

57
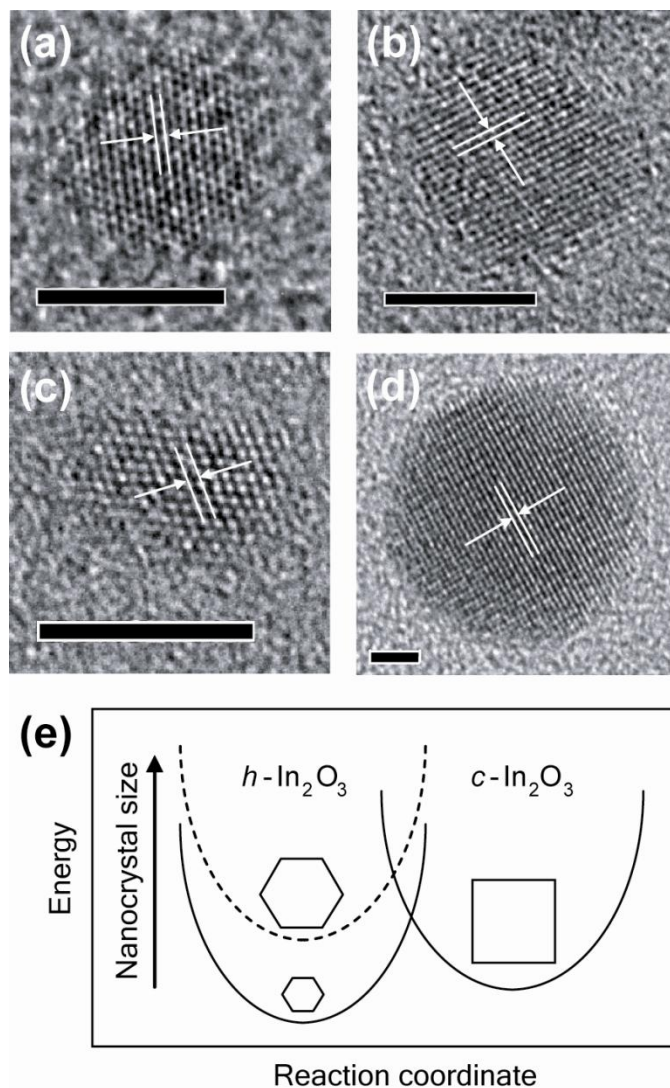
Figure 4.5 Phase transformation of colloidal Mn^{3+}- and Cr^{3+}-doped In_2O_3 nanocrystals. (a-d) High resolution TEM images of Mn^{3+}-doped In_2O_3 nanocrystals synthesized with [Mn]/[In]=0.10 (a, b), and Cr^{3+}-doped In_2O_3 nanocrystals synthesized with [Cr]/[In]=0.10 (c, d). Lines and arrows indicate the d-spacings. The d-spacings of ca. 2.74 Å (a, c) correspond to {110} lattice plane of rh-In_2O_3, and the d-spacings of 2.91 Å (b) and 2.54 Å (d) correspond respectively to {222} and {400} lattice planes of bcc-In_2O_3. The critical size for nanocrystal transformation from rh-In_2O_3 (a, c) to bcc-In_2O_3 (b, d) is ca. 5 nm. Scale bars: 5 nm (a-c), 2 nm (d). (e) Schematic representation of the change in the potential energy curve of rh-In_2O_3 NCs with increasing NC size.

For small Mn^{3+}:In_2O_3 NC (Figure 4.5a) the average d-spacing of 2.74 Å can be assigned to {110} plane of rh-In_2O_3. The NC in Figure 4.5b has the average d-spacing of 2.91 Å, which corresponds

58

to{222} plane of bcc-In_2O_3. The same is observed for Cr^{3+}:In_2O_3 NCs (Figure 4.5c, d). These findings indicate that a decrease in NC size due to the presence of dopant ions stabilizes the metastable rh-In_2O_3 (Figure 4.5e).

4.2 Difference in Incorporation of Chromium(III) and Manganese(III) Dopants in In_2O_3 NCs

The measurements of the doping concentrations with ICPAES reveal very different incorporation of Mn^{3+} and Cr^{3+} dopant ions. The average Mn^{3+} concentrations for the samples synthesized with [Mn]/[In] of 0.05, 0.10, and 0.15 are 5.0, 8.8, and 12.3 mol % ([Mn]/([In] + [Mn])), respectively. The fraction of Mn^{3+} incorporated from its precursor into NCs decreases with increasing precursor concentration, suggesting higher concentrations of Mn^{3+} in bcc-In_2O_3 than in rh-In_2O_3 NCs.

This conclusion was clearly confirmed by size selective precipitation of the sample prepared with [Mn]/[In]) 0.05 (Figure 4.6), revealing the average Mn^{3+} doping concentration of 5.7 mol % in bcc-In_2O_3 and 4.2 mol % in rh-In_2O_3 NCs. On the other hand, the fraction of incorporated Cr^{3+} increases with increasing precursor concentration. For [Cr]/[In]=0.05 the average doping concentration is 3.0 mol % and for [Cr]/[In]=0.15, 13.8 mol %, which indicates lower incorporation rate into bcc-In_2O_3 and higher into rh-In_2O_3 NCs. These trends are confirmed at the single NC level using EDX (Figure 4.7a, b). Clearly, the NC size alone is not responsible for lower doping concentration of Mn^{3+} in rh-In_2O_3 NCs due to exclusion of dopants from the initially formed nuclei. Figure 4.7c shows EDX elemental line scan profiles of In and Mn in a representative Mn^{3+}:bcc-In_2O_3 NC having cubic morphology (Figure 4.7c, inset). In and Mn profiles have nearly identical forms, indicating a homogeneous distribution of dopants throughout the NC. This conclusion was quantitatively supported with a geometrical model designed to simulate the profiles of NCs having cubic morphology. Both In and Mn line scan profiles are fit well to the same functional form (Figure 4.7c, black line), confirming that dopants are homogeneously distributed across the NC, and are not segregated in an outer shell

59
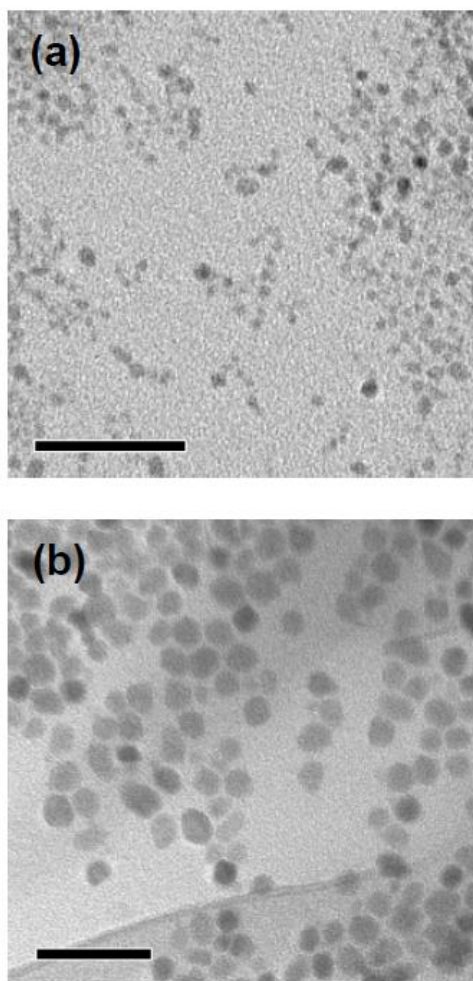
Figure 4.6 TEM images of Mn^{3+}-doped In_2O_3 nanocrystals prepared with [Mn]/[In]=0.05 after size selective precipitation. (a) Small nanocrystals having corundum crystal structure with average doping concentration of 4.2 mol %. (b) Large nanocrystals having cubic-bixbyite crystal structure with average doping concentration of 5.7 mol %. Scale bars: 50 nm.
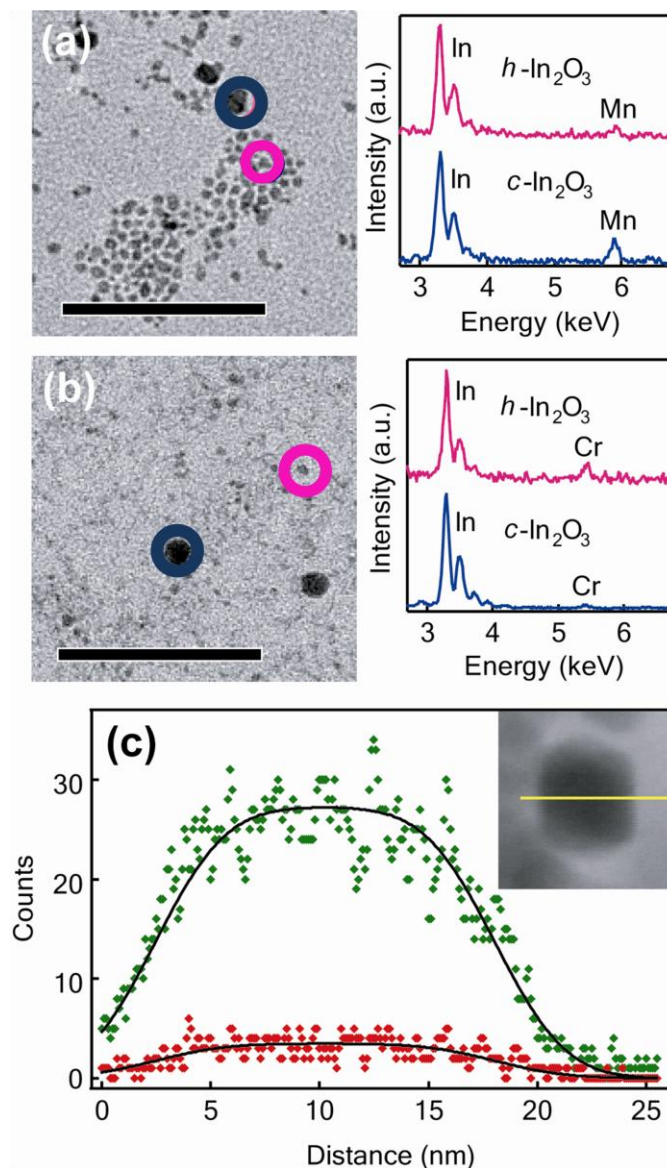
Figure 4.7 (a, b) TEM images (left) and EDX spectra (right) of Mn^{3+}-doped In_2O_3 (a) and Cr^{3+}-doped In_2O_3 nanocrystals. (b) Nanocrystals analyzed by EDX spectroscopy are circled with the corresponding colors in associated TEM images. Both samples were synthesized with dopant to In^{3+} precursor ratio of 0.10. (c) EDX elemental line scan profile of the Mn^{3+}-doped In_2O_3 nanocrystal shown in inset. Mn (red) and In (green) profiles can be fit to the same scaled function (black line), indicating a homogeneous distribution of Mn dopants.

For doped In_2O_3 it has been suggested that some dopant ions, such as Sn^{4+} and Fe^{3+}, can stabilize rh-In_2O_3 due to their smaller sizes in comparison to In^{3+}.[93, 94] In this work all samples were prepared

identically, but with different starting concentrations of dopant ions. The doping concentrations of Mn^{3+} and Cr^{3+} in $rh\text{-}In_2O_3$ NCs are different, although both ions have similar ionic radii in octahedral coordination ($r(Mn^{3+})$=0.65 Å, $r(Cr^{3+})$=0.62 Å). Furthermore, higher doping concentrations of Mn^{3+} in $bcc\text{-}In_2O_3$ than in $rh\text{-}In_2O_3$ NCs suggest that dopant incorporation is not the main factor for the stabilization of corundum-type In_2O_3 NCs.

4.3 Mechanism of Inhibition of the Growth of NCs in the Presence of Dopant Ions

Formation of NCs smaller than 5 nm allows for the spontaneous stabilization of $rh\text{-}In_2O_3$ proving that dopants do not have to be incorporated into NCs to induce the phase transformation. Instead, the dopant ions inhibit the NC growth as they bind to the surfaces of NCs during incorporation, leading to the stabilization of metastable In_2O_3. We believe that this adsorption-driven inhibition of the NC growth accompanied by the stabilization of metastable structures is a general phenomenon for the polymorphic materials having sufficiently small differences between the potential energy minima of different crystal structures. The dopant incorporation is then determined by the average residence time (τ) of dopant ions on the NC surfaces, which is directly related to their heat of adsorption (ΔH_{ads}):

$$\tau = \tau_0 \exp\left(\frac{\Delta H_{ads}}{RT}\right)$$
<div align="right">**Equation 10**</div>

where τ_0 is correlated with the adsorbed dopant vibration times.[95] The key parameter in Equation 10 is the heat of adsorption released upon trapping of the dopant ions on the NC surfaces. From the mechanistic point of view ΔH_{ads} depends on different factors influencing the interaction of dopant ions with NC surfaces. Specifically, in order for a dopant ion to be adsorbed to the NC surfaces and eventually incorporated into the NC lattice it has to undergo ligand substitution and a change in coordination (i.e., coordinated ligands in the solution have to be replaced by surface binding sites). The relationship between the stabilization of a dopant ion by the coordinating ligands and the dopant affinity for a particular NC surface site will determine ΔH_{ads}. In this study the NCs of the same material having two different crystal structures were doped under identical conditions with transition-metal ions that have nearly identical size and the same oxidation state. The oxides of Cr^{3+} and Mn^{3+} (Cr_2O_3 and $\alpha\text{-}Mn_2O_3$) are, however, structurally closely related to $rh\text{-}In_2O_3$ and $bcc\text{-}In_2O_3$, respectively. These observations suggest that the affinity of a dopant ion binding to NC surface sites

and the incorporation of surface-bound dopants depend on the relationship between the surface structure of the NC host lattice and the nature of the dopant ion. The NC surface structure is to a large extent defined by the crystal lattice structure. Microscopically, however, the NC surfaces are heterogeneous and contain different types of defect sites. While dopant ions have different ΔH_{ads} on different surface sites, the average value of ΔH_{ads} should reflect the binding affinity of a dopant ion on the surfaces of particular NCs. We believe that this affinity is strongly affected by how closely the crystal structures of dopant transition-metal oxides (TM_2O_3) are related to the structure of a given host In_2O_3 polymorph in this work. In case of structurally similar lattices the structure and geometry of NC host lattice surface sites would generally closely resemble those that dopant ions would encounter during the growth of their own lattice of the analogous material. Incidentally, in the case of Co^{2+}:ZnO NCs for which very high doping concentrations have been reported,[96] CoO and ZnO NCs are isostructural under applied synthetic conditions and have very similar lattice parameters, both of which are expected to contribute to a high doping concentration limit. The growth of polymorphic NCs in the presence of dopant impurities is complex and consists of at least three major steps: (1) nucleation, which is very fast and generally excludes the dopant ions, (2) stabilization and growth of metastable NCs whose size and doping concentration are determined by the amount of dopant precursor and ΔH_{ads} , and (3) transformation of metastable NCs upon reaching the critical size, followed by a change in the rate of dopant incorporation based on the change in ΔH_{ads}. This mechanism contrasts the stabilization of bulk corundum-type In_2O_3 by dopant ions, which is according to many accounts determined by incorporation of smaller dopant ions. Interestingly, our results indicate that in the kinetic mechanism of doping colloidal NCs the dopant incorporation is determined by the NC structure, which can be manipulated by changing the NC size. The NC size, structure, and composition are inherently connected, and all critically depend on the relative concentration of precursors in the reaction mixture. This mutual dependence is shown for Mn^{3+}:In_2O_3 NCs as a three dimensional plot (Figure 4.8), which can be used to predict the expected size, structure, and doping concentration for particular preparation conditions.
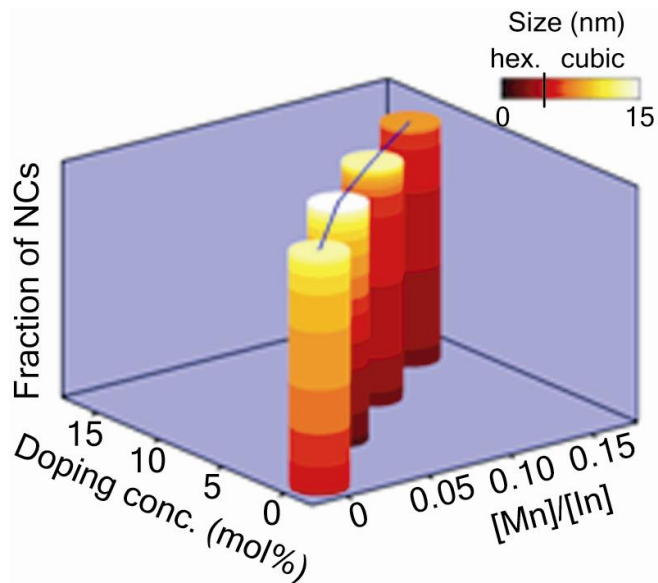
Figure 4.8 Three-dimensional plot of interdependence between Mn vs In precursor ratio ([Mn]/[In]), nanocrystal doping concentration, and the nanocrystal size distribution (*x*, *y*, and *z* axes, respectively). The nanocrystal sizes are shown as colors in the color coded bar with the black line indicating the critical size for transformation of hexagonal to cubic In_2O_3 nanocrystals. The blue line in the graph shows the dependence of the starting precursor ratio on the doping concentration (*x-y* data).

Chapter 5

Optical and Magnetic Properties of Transition Metal Ions Doped In$_2$O$_3$ NCs

In this chapter we study the spectroscopic and magnetic properties of TM ions doped into In$_2$O$_3$ colloidal NCs, and their films. Magnetic properties of these nanocrystals were studied by magnetic susceptibility and MCD. We demonstrate the appearance of ferromagnetism in nanocrystalline films prepared from paramagnetic free-standing NCs, which can be associated with extended NC interfacial defects in such films.

5.1 Chromium Doped In$_2$O$_3$ NCs

5.1.1 Chromium K-edge XAS Measurements

To obtain quantitative information about the local environment of chromium sites, we conducted a systematic XAS study of Cr^{3+}:In$_2$O$_3$ NC samples having different Cr^{3+} concentrations. The average concentration of chromium in Cr^{3+}:In$_2$O$_3$ NCs for different starting concentration of chromium after doing size selective precipitation were measured with ICP. At low starting concentrations of Cr^{3+} ([Cr^{3+}]/[In^{3+}]=0.05), the fraction of Cr^{3+} incorporated from its precursor to bcc-In$_2$O$_3$ NCs is 3 at% (bcc-In$_{1.942}$Cr$_{0.058}$O$_2$). The average concentration of Cr^{3+} incorporated from its precursor to rh-In$_2$O$_3$ for the starting precursor mixture of [Cr]/[In]=0.20 was 20 at% (rh-In$_{1.667}$Cr$_{0.333}$O$_2$).

Normalized Cr K-edge X-ray absorption spectra of Cr^{3+}:In$_2$O$_3$ and Cr$_2$O$_3$ standard in the full spectral range are shown in Figure 5.1 a. A direct comparison between the spectra of Cr^{3+}:In$_2$O$_3$ and Cr$_2$O$_3$ standard in the near edge region confirms that chromium ions have 3+ oxidation state in Cr^{3+}:In$_2$O$_3$ NCs. Figure 5.1b shows the *k*-weighted Cr K-edge EXAFS spectra of samples shown in Figure 5.1a. The spectra were Fourier transformed in the region of 2.6-15.0 Å^{-1} from *k*-space to *R*-space. The resulting pseudo-radial distribution functions are shown in Appendix A. 4. The first prominent peak centered at ca. 1.5 Å is due to backscattering of the ejected photoelectron from the first coordination shell of the neighboring oxygen atoms (Cr-O).
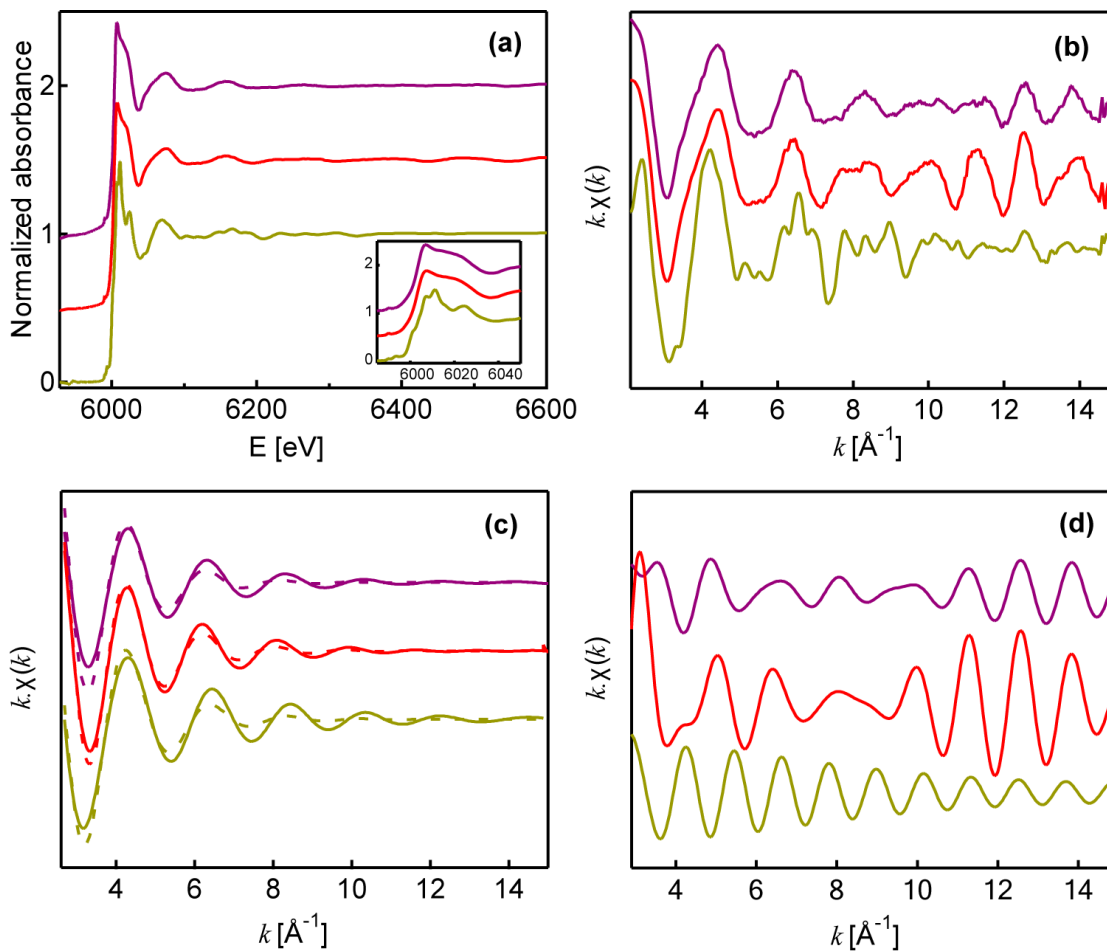
Figure 5.1 (a) Chromium K-edge absorption spectra, (b) k-weighted Cr K-edge EXAFS spectra, (c) Fourier-filtered EXAFS spectra for the In-O shell, and (d) Fourier-filtered EXAFS spectra for the (Cr-In and/or Cr-Cr) shell correspond to the Cr_2O_3 (olive line), rh-$In_{1.667}Cr_{0.333}O_2$ (red line), and bcc-$In_{1.942}Cr_{0.058}O_2$ (purple line).

The inverse Fourier transform of the first (R=1.1-2.0 Å) shell of the pseudo-radial distribution functions gives the Fourier-filtered EXAFS spectra which are shown in Figure 5.1c. The Fourier-filtered curves were fit well in the k-range of 2.6-15.0 Å^{-1} with one In-O shell (Figure 5.1c, dashed lines). Table 5.1 summarizes the structural parameters for the In-O shell obtained from the curve-fitting.

The EXAFS spectra of Cr_2O_3 and Cr^{3+}:In_2O_3, are very different from each other, which indicates a different local environment for chromium atoms in Cr_2O_3 and In_2O_3 lattices. Fitting results for Cr_2O_3 standard suggest that Cr^{3+} coordinates with 6 oxygen atoms, with an average Cr-O bond distance of

1.99±0.01 Å. These results are in good agreement with the crystallographic data, from which the average Cr-O bond length was determined to be 1.99 Å.[68] The average bond distance for the In-O shell in In_2O_3 was reported to be 2.17-2.18 Å.[22, 88] EXAFS analysis presented in Table 5.1 shows that the average Cr-O bond distances in all Cr^{3+}:In_2O_3 NC samples are longer than those in pure Cr_2O_3, but shorter than the In-O bond distances in pure In_2O_3. This suggests that due to substitution of Cr in In_2O_3 the average Cr-O bond distances increase in compared to the pure Cr_2O_3.

Table 5.1 Results of the fits of EXAFS spectra for the first Cr-O shell.

Sample	N	R(Å)	$^a\sigma^2$(Å^2)	$^b\rho$% ^{b}
bcc-$In_{1.942}Cr_{0.058}O_2$	6	2.043±0.051	0.020	8.24
rh-$In_{1.667}Cr_{0.333}O_2$	6	2.081±0.017	0.015	2.45
Cr_2O_3	6	1.991±0.016	0.016	6.36

^{a} Debye-Waller factor. ^{b} Weighted residual factor.

Fourier-filtered EXAFS spectra of the second shell (Cr-In and/or Cr-Cr) for R-space in the region of 2.0-3.0 Å, are shown in Figure 5d. In the k range 9.0-15.0 Å^{-1}, by substitution of chromium atoms by indium atoms the back scattering amplitude increased. This could be due to the indium atoms having a higher back scattering amplitude compared with the chromium atoms.

5.1.2 Electronic Absorption and Magnetic Circular Dichroism Spectroscopies

The ground state of free Cr^{3+} (d^3) ion is described by ^{4}F term. In octahedral ligand field, this term splits into three terms giving rise to two characteristic spin-allowed quartet-quartet transitions where, spectrum generally shows two broad bands in the visible region.[84, 97] The low energy transition, $^4A_{2g}\rightarrow{}^4T_{2g}$, was known as U-band, and higher energy transition, $^4A_{2g}\rightarrow{}^4T_{1g}$, was known as Y-band.[98, 99] The spin-allowed transitions of Cr^{3+} are electric-dipole transitions and are parity-forbidden transitions due to Laporte selection rule.[84, 99] The forbidding of these transitions can be relaxed under certain circumstances including the situation where the inversion center is removed due to lower symmetry site of Cr^{3+} ion and/or vibronic coupling. [84, 99] The weak absorption bands below the transition to $^4T_2$ are associated with the spin-forbidden transitions ($^4A_{2g}\rightarrow{}^2E$, $^2T_2$).[84, 98] The intensity of spin-forbidden bands increases due to the spin-orbit coupling between spin-forbidden transitions and $^4T_2$ state, enabled by vibrational modes.[84, 100] In low-symmetry sites of distorted octahedral, U and Y-bands subject to the splitting due to the removing of the degeneracy of the T states. In trigonally

67

distorted octahedral fields (e.g. C_{3v}), $^4T_2$ split into ^4E and $^4A_1$ terms, and $^4T_1$ split into ^4E and $^4A_2$ terms. As symmetry decrease further to C_2, E term split to B_1 and B_2 terms.[101]

The average concentration of Cr^{3+} incorporated from its precursor to rh-In_2O_3 NCs after size selective precipitation for the starting precursor mixture of [Cr]/[In]=0.10 was 9.5 at% (further in the text generally referred to as rh-$In_{1.827}Cr_{0.173}O_3$). The ligand-field electronic absorption spectrum of rh-$In_{1.827}Cr_{0.173}O_2$ NCs at 300 K is shown in Figure 5.2a. The two peaks at ~ 16639 cm^{-1} and ~23256 cm^{-1} can be assigned to the corresponding $^4A_2$→$^4T_2$ and $^4A_2$→$^4T_1$ d-d transitions, respectively, of pseudo-octahedral of Cr^{3+}. A small but observable shoulder at ~14440 cm^{-1} can be assigned to the formally $^4A_2$→^2E, $^2T_2$ spin-forbidden transitions. The band gap transition of the host bcc-In_2O_3 NCs is observed as a broad shoulder at ~37500 cm^{-1}. The band gap energy is estimated from the absorption spectrum to be ~4.2 eV. This corresponds to the band gap energy which was mentioned for rh-In_2O_3 NCs (section3.1.4). Figure 5.2b shows 4.5 K MCD spectra of the same NCs collected in a variable magnetic field from 1 to 7 T. The 16639 cm^{-1} absorption band correlates to a structured feature in the MCD spectra at the same energy. The second spin-allowed transition is likely mixed with a charge transfer transition involving the NC host lattice, leading to the asymmetric peak centered at 28209 cm^{-1}. The spin-forbidden transitions are readily identified in the MCD spectra which shown as the inset in Figure 5.2b. Figure 5.2c shows the MCD intensities at 14440 and 16639 cm^{-1} plotted as a function of the applied magnetic field, along with the fit to the spin-only Brillouin function for the spin state S=3/2, using the g value of 1.96.[102]

$$M_s = \frac{1}{2} N g \mu_B \left[(2S+1) \coth \left((2S+1) \left(\frac{g\mu_B H}{2k_B T} \right) \right) - \coth \left(\frac{g\mu_B H}{2k_B T} \right) \right] \qquad \textbf{Equation 11}$$

Where N, μ_B and k are the total number of dopants per unit volume, the Bohr magneton and the Boltzmann constant, respectively, T is the temperature, and H is the applied magnetic field. The intensity saturates at high filed and low temperatures, consistent with the C-term MCD behavior. The spin-only Brillouin function fits for the only-spin state of 3/2 is a result of the absence of the orbital angular momentum in the $^4A_2$ ground state of Cr^{3+}. For higher energy spectral position at 28209 cm^{-1}, fits for the spin-only Brillouin function slightly deviated from the S=3/2 which is likely a consequence of mixing of Y-band with a charge transfer transition involving the NC host lattice. A fit to the spin-only Brillouin function demonstrate that, these MCD intensities arise from magnetically isolated Cr^{3+} ions in In_2O_3 NCs.
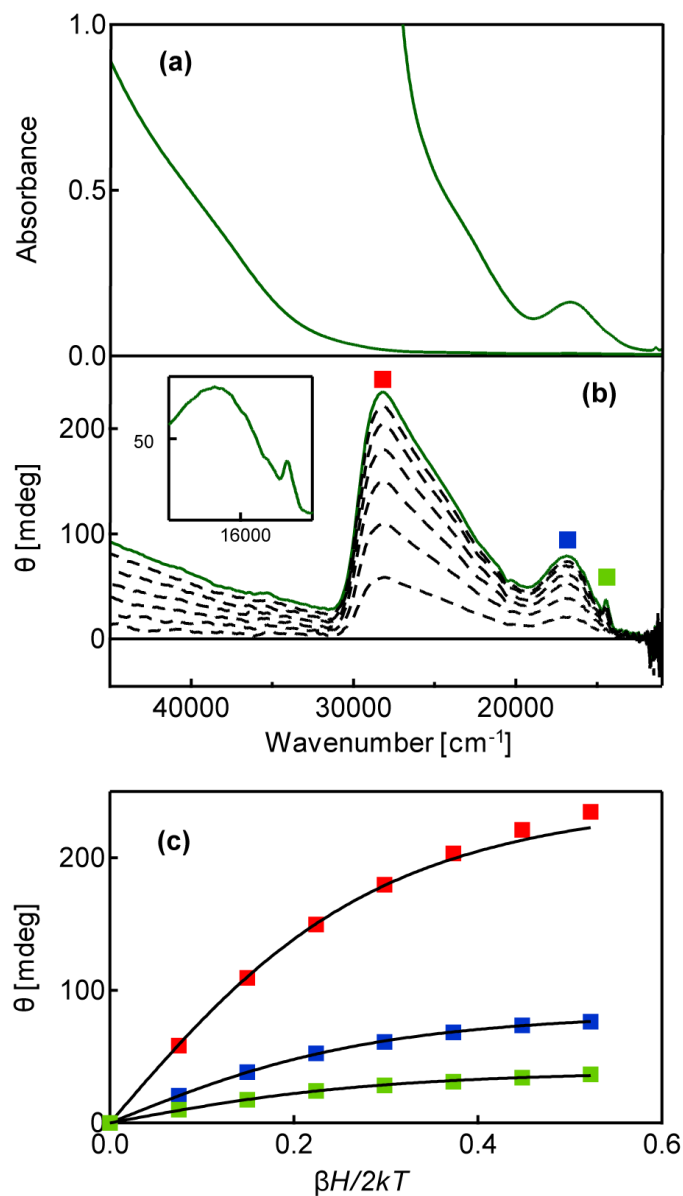
Figure 5.2 (a) 300 K electronic absorption spectrum of rh-$In_{1.827}Cr_{0.173}O_2$ NCs. (b) MCD spectra of the same sample at 4.5 K, collected in variable magnetic field (1-7 T). (c) Variable field MCD intensities at 4.5 K from the spectra in (b) with the corresponding labels. The black lines are fits to the Brillouin function.

The ligand-field electronic absorption spectrum of bcc-$In_{1.942}Cr_{0.058}O_2$ NCs is shown in Figure 5.3a. Two characteristic ligand-field bands at $\sim$16570 cm^{-1} and $\sim$21119 cm^{-1} can be assigned to the peaks corresponding to $^4A_2 \rightarrow ^4T_2$ and $^4A_2 \rightarrow ^4T_1$ transitions. A small but observable shoulder at 14440 cm^{-1} can be assigned to the formally $^4A_2 \rightarrow ^2E, ^2T_2$ spin-forbidden transitions. The band gap transition of the

69

host In_2O_3 NCs is observed as a broad shoulder at $\sim$32500 cm^{-1}. The band gap energy was estimated from the absorption spectrum to be $\sim$3.7 eV, similar to the band gap energy of bulk and nanocrystal of bcc-In_2O_3.[103]
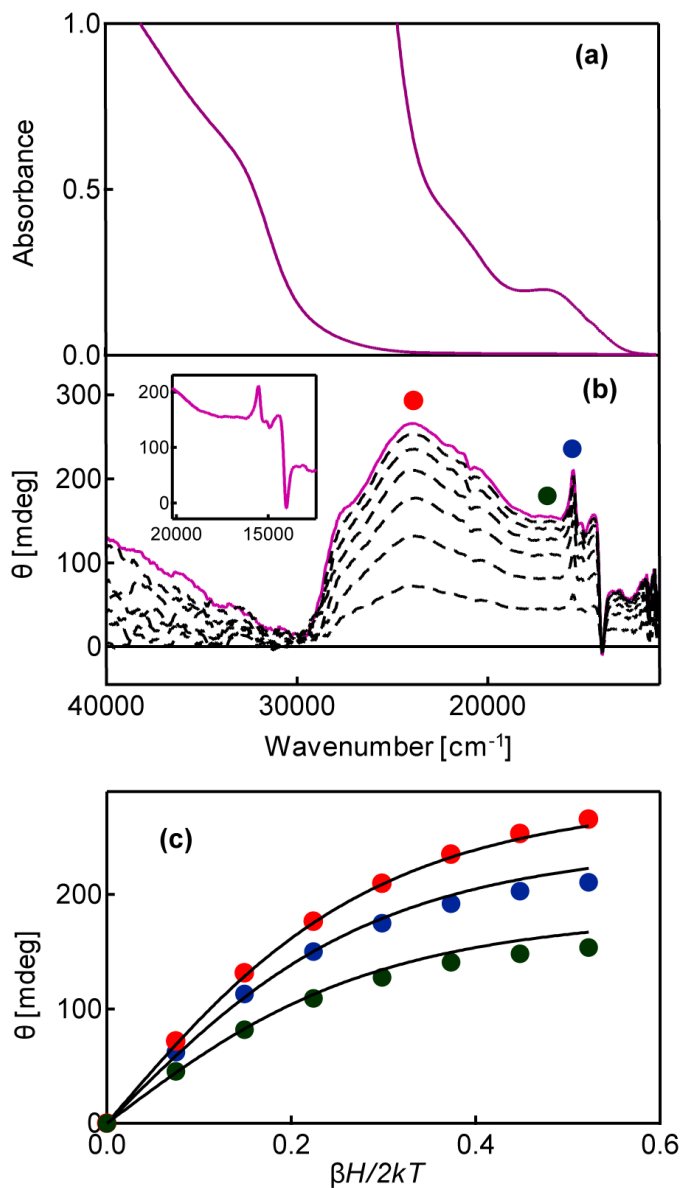
Figure 5.3 (a) Electronic absorption spectrum of bcc-$In_{1.942}Cr_{0.058}O_2$ at 300 K. (b) MCD spectra at 4.5 K for the same sample, collected in variable magnetic field (1-7 T). (c) Variable field MCD intensities at 4.5 K from the spectra in (b) with the corresponding labels. The black lines are fits to the Brillouin function.

70

As is the case with the absorption spectra, only a limited amount of information can be obtained from broad absorption bands. In fact, the splitting is small and was not observable in the absorption spectra, which closely resemble those of similar octahedral complexes. The MCD spectra (Figure 5.3b) clearly show the distinct difference with the absorption spectrum. The MCD spectra reveal three sharp peaks at 14440, 15094 and, 15528 cm^{-1}. The broad feature at $\sim$16570 cm^{-1} corresponds to the absorption peak at the same energy superimposed by these three sharp transitions. MCD spectra can greatly aid in the detection and assignment of spin-forbidden Cr^{3+} transitions hidden in the absorption spectra under the red tail of the U-band. The study of polarized absorption spectra of Cr^{3+} in diopside with C_2 symmetry site for cation has revealed that the U-band ($^4A_{2g} \rightarrow {}^4T_{2g}$) is superimposed by three sharp spin-forbidden transitions, similar to the result that we see in MCD spectra of bcc-$In_{1.942}Cr_{0.058}O_2$ NCs.[99] The difference in the MCD spectra of Cr^{3+}-doped bcc-In_2O_3 and Cr^{3+}-doped rh-In_2O_3 reveal that Cr^{3+} ions distinctly occupy different symmetry sites in corundum and bixbyite crystal structure of In_2O_3. This is in agreement with this fact that Cr^{3+} with ionic radius smaller than the ionic radius of In^{3+} is preferred to occupy C_2 symmetry site. In the higher energy part of the spectra second spin allowed transition likely mixed with charge transfer raising a peak which centered at 23923 cm^{-1}. The fitting of the MCD intensities at 14440, and, 16570 cm^{-1} to the spin-only Brillouin function using g=1.96 shows the deviation from the S=3/2. The $^4A_2$ ground state of Cr^{3+} in an octahedral crystal field has no orbital angular momentum while the spin-orbit coupling within the low symmetry split $^4T_1$ state likely gives rise to the deviation from the spin-only magnetization.[57] In fact, finding the magnetic moment of a term subject to the influence of both spin-orbit coupling and low symmetry ligand filed components is one of some complexity.[97] For higher energy spectral position at 23923 cm^{-1}, fits for the spin-only Brillouin function slightly deviated from the S=3/2 which is likely a consequence of mixing of Y-band with a charge transfer transition involving the NC host lattice. The study of polarized spectra of Cr^{3+} in ruby reveled that most of the intensity of spin-allowed transitions is due to an overcoming of the symmetry selection rule by coupling of the electronic transition with an odd vibration.[99] Whereas for Cr^{3+} in diopside with C_2 symmetry site for Cr^{3+} the spin-allowed transitions gained intensity due to lower symmetry site of cation.[99] The differences in the origin of the mechanism to gain intensity in the absorption spectra increase the complexity of the spectroscopy study of Cr^{3+} in different site symmetries.

71

5.1.3 Magnetism

The magnetization properties of 2.7% Cr^{3+} doped bcc-In_2O_3 NCs measured from 5 to 300 K are shown in Figure 5.4. Free-standing NCs show only paramagnetism (Figure 5.4a, green squares).
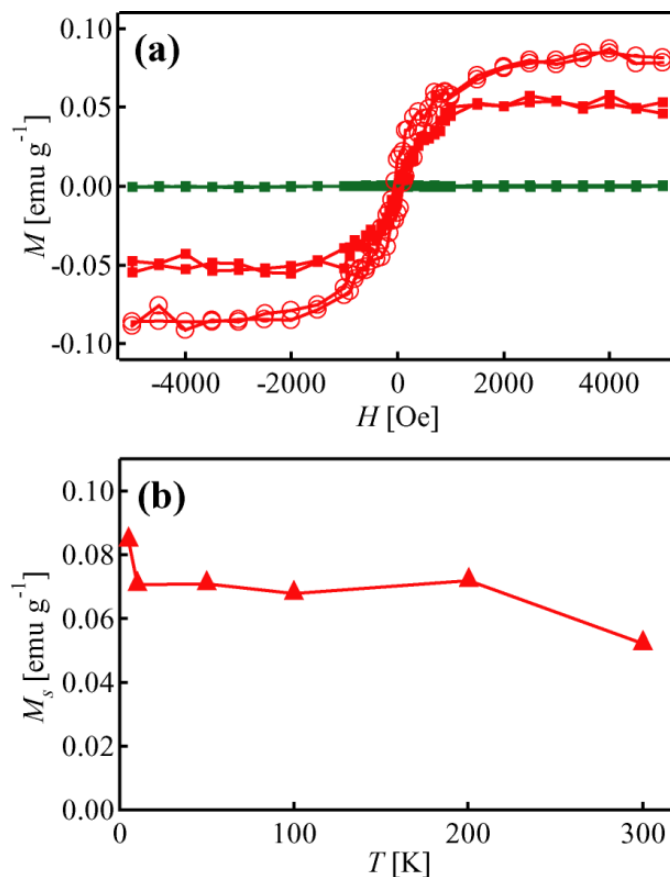
Figure 5.4 (a) *M* vs *H* data for free-standing 2.7% Cr^{3+}:In_2O_3 NCs measured at 300 K (green squares), and the corresponding nanocrystalline films measured at 5 K (red circles) and 300 K (red squares). All loops are corrected for diamagnetic contribution. (b) Temperature dependence of M_s for Cr^{3+}:In_2O_3 nanocrystalline films.

Nanocrystalline films fabricated from the same NCs exhibit rapid magnetization (*M*) saturation and small hysteresis coercivity, indicating ferromagnetic ordering. Hysteresis loops for nanocrystalline films at 5 and 300 K are shown in Figure 5.4a as red circles and squares, respectively. A decrease in magnetization and hysteresis coercivity with increase in temperature is observed. The temperature dependence of the ferromagnetic saturation magnetization (*M*s) is plotted in Figure 5.4b. The ferromagnetic phase transition is not observed indicating T_C above 300 K. The saturation

magnetization of the nanocrystalline film in Figure 5.4 is estimated to be 0.17 Bohr magneton (µB) per Cr^{3+} at 300 K and 0.27 µB/ Cr^{3+} at 5 K. The magnetic moments per dopant ion were quantified based on the unit mass magnetization and the elemental composition of the sample.

The origin of ferromagnetism in nanocrystalline TCOs is of great fundamental and practical importance. Recent experimental and theoretical studies to discover the origin of ferromagnetism in DMSOs have shown that long-range ferromagnetic interactions in these materials can be mediated by charge carriers.[13, 59] This means a change in the carrier concentration has effect on the observed ferromagnetism. The absence of ferromagnetism in the free standing Cr^{3+}:In_2O_3 NCs and appearance of ferromagnetism only in Cr^{3+}:In_2O_3 films prepared from colloidal NCs is consistent with the pervious findings of ferromagnetism in DMSO NCs films prepared from free standing DMSO NCs in which the existence of extended structural defects, proposed to be oxygen vacancies at the NC interfaces, play a key role in mediating magnetic ordering of dopant ions and is responsible for the long range magnetic ordering in these materials.[104-106] In fact, in DMSO NCs with high surface to volume ratios, likely more oxygen vacancies are present at the surface of NCs and networking of NCs in the prepared film causes an increase grain-boundary defects at interfaces (e.g. oxygen vacancies).

Philip *et al.* [13] have shown magnetic behavior in Cr^{3+} doped bcc-In_2O_3 films can be controllably tuned by defect concentration. They observed that the Cr^{3+} doped bcc-In_2O_3 films exhibit ferromagnetism when the films are highly oxygen deficient, and are paramagnetic otherwise. In addition, Xing *et al.*[107] have found a strong correlation between ferromagnetism and oxygen deficiency in Cr^{3+} doped bcc-In_2O_3 nanostructures. Observation of ferromagnetism in our Cr^{3+}:In_2O_3 nanocrystalline films imply the important role of interfacial defects for manipulating the long-range magnetic ordering in DMSOs.

In addition, in our experiments ferromagnetism is not evident in In_2O_3 nanocrystalline films prepared under similar conditions as Cr^{3+}:In_2O_3 films (Figure 5.5). The magnetization observed in pure oxide dielectrics, such as HfO_2 thin films, has also been associated with magnetic contamination resulting from handling the substrates with inadequate tools.[108] We handled identically all of our samples (doped and undoped) in a carefully controlled nonmagnetic environment.
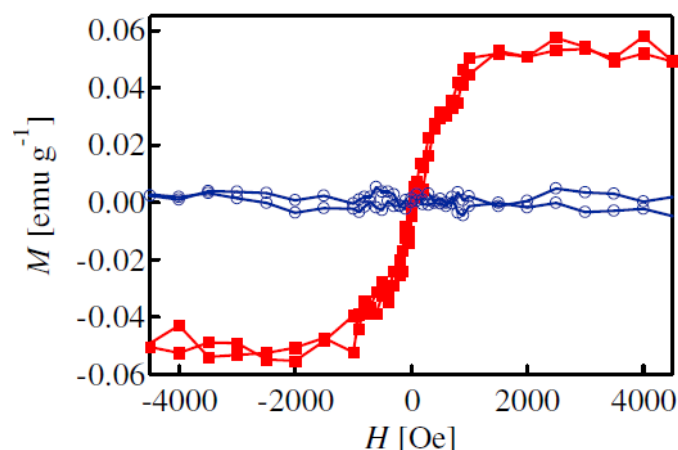
Figure 5.5 *M* vs. *H* data for In$_2$O$_3$ nanocrystalline film (blue circles) measured at 300 K, showing no ferromagnetic ordering. Hysteresis loop for 2.7 % Cr^{3+}:In$_2$O$_3$ nanocrystalline film (red circles) recorded at 300 K is shown for comparison. Both loops were corrected for diamagnetic contribution.

It should be also noted that nanocrystalline antiferromagnetic materials, such as Cr$_2$O$_3$, can generate spontaneous magnetic ordering at high temperatures owing to the spins at nanoparticle surfaces.[81, 109] Nanocrystalline Cr$_2$O$_3$ has a distinctly different magnetic behavior from Cr^{3+}:In$_2$O$_3$ nanocrystalline film, showing no ferromagnetism at room temperature, and only superparamagnetic behavior at low temperatures (Appendix A. 5). Taken together, our results suggest the intrinsic ferromagnetism in Cr^{3+}:In$_2$O$_3$ nanocrystalline structures fabricated from colloidal Cr^{3+}:In$_2$O$_3$ NCs as building blocks.

5.2 Manganese Doped In$_2$O$_3$ NCs

5.2.1 Electronic Absorption Spectroscopy

The ground-state term in high-spin Mn^{3+}(d^4) ion is 5D (Figure 5.6a). In the ideal octahedral (O$_h$) coordination this term splits into ^{5}E$_g$ and ^{5}T$_{2g}$ terms, giving a characteristic spin allowed transition ^{5}E$_g$ → ^{5}T$_{2g}$. In a reduced symmetry, the ^{5}T$_{2g}$ transforms into additional components (i.e. ^{5}A$_1$ and ^{5}E terms in trigonal crystal fields).[110] In many six-coordinate Mn^{3+} complexes Jahn-Teller distortions lead to additional ground state (^{5}E$_g$) splitting, resulting in low-energy absorption features. This effect has been particularly studied in tetragonally distorted octahedral fields.[84]
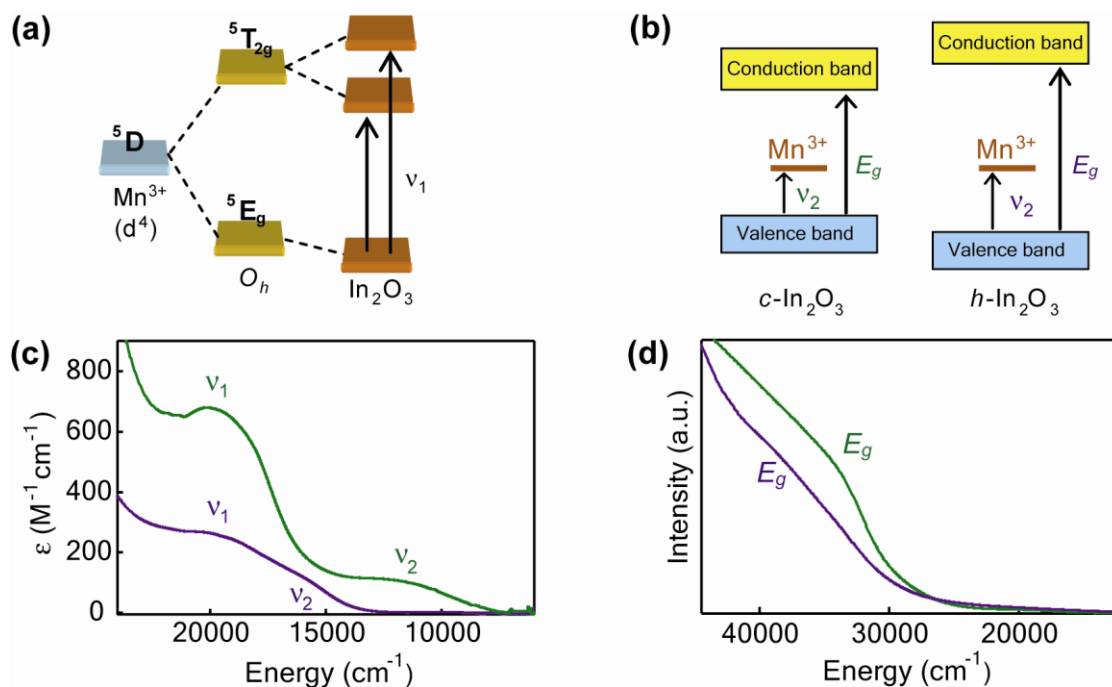
Figure 5.6 Electronic structure of Mn^{3+}-doped In_2O_3 nanocrystals. (a) Ligand-field energy state splitting pattern of Mn^{3+} (d^4 system) in distorted octahedral coordination. (b) A schematic representation of the difference in the electronic structure between Mn^{3+}-doped bcc-In_2O_3 and rh-In_2O_3 nanocrystals. (c) Ligand-field electronic absorption spectra of Mn^{3+} dopants in bcc-In_2O_3 (green) and rh-In_2O_3 (purple) nanocrystals showing the transitions indicated in (a) and (b). (d) The band gap absorption spectra of selectively precipitated Mn^{3+}-doped bcc-In_2O_3 (green) and rh-In_2O_3 nanocrystals (purple) prepared with [Mn]/[In]=0.05. The band gap energy of rh-In_2O_3 nanocrystals is blue-shifted with respect to the band gap energy of bcc-In_2O_3 nanocrystals together with ν_2 transition.

We used the ligand-field electronic absorption (LFEA) spectroscopy as a direct probe of Mn^{3+} ligand-field transitions in In_2O_3 NCs. The LFEA spectrum of Mn^{3+} in rh-In_2O_3 NCs is distinctly different from that of Mn^{3+} in bcc-In_2O_3 NCs, indicating a change in the electronic structure (Figure 5.6c). In both spectra the higher energy band at ca. 20 000 cm^{-1} can be readily assigned to possibly unresolved $^5T_{2g}$ components (ν_1). The lower energy transition (ν_2) is, however, significantly different for the two samples. The origin of this transition has been discussed over the years as spin-forbidden transition,[111] low energy charge-transfer band,[112, 113] or ground-state split transition.[114] The energy and intensity of ν_2 argue against its assignment to the spin-forbidden transition ($^5E \rightarrow {}^3T_1$). On the other hand, the charge transfer transitions should depend on the energy of the valence and conduction bands and therefore should be sensitive to the NC size and structure. We observed a blue shift in the band

75

gap absorption (E_g) of rh-In_2O_3 NCs with respect to bcc-In_2O_3 NCs concurrently with the shift in ν_2 (Figure 5.6d). We therefore believe that the most likely assignment of ν_2 is the low-energy ligand-to-metal charge transfer transition (Figure 5.6b). This assignment is supported by the recently reported charge transfer energy shift with size in Co^{2+}:ZnSe NCs.[115] While ^5E_g splitting should be less pronounced in strictly trigonal fields, such as C_3 and D_3, it is possible that the second order ground state splitting presumably due to Jahn-Teller type distortion may also contribute to ν_2 transition.

Although the exact origin of this transition may still be somewhat in question, these data unambiguously show that the NC host lattice structure strongly influences the electronic configuration of the dopant ions. Furthermore, the experimentally determined extinction coefficients (ε) indicate lower intensity of ligand-field transitions in rh-In_2O_3 than in bcc-In_2O_3 NCs. The charge-transfer processes involving dopant ions have been suggested to be crucial for ferromagnetism in oxide DMSs. Tuning the electronic structure and properties of dopant ions by changing the NC size and structure allows for the investigations of the origin of dilute magnetic ordering in oxides, and the expansion and optimization of the available multifunctional semiconductors.

5.2.2 Magnetism

Room temperature ferromagnetism was observed in nanocrystalline films fabricated from colloidal 8.8% Mn^{3+} doped rh-In_2O_3 NCs (Figure 5.7). In contrast to the nanocrystalline films, the TOPO-capped free-standing NCs show only paramagnetism. The observation of ferromagnetic ordering of different dopant ions in In_2O_3 NCs, only upon their incorporation into nanocrystalline films, suggests that the defect induced dilute magnetic ordering is a general phenomenon dependent on the post-synthesis processing of NC building blocks. These results support an intrinsic origin of ferromagnetism in defective transition-metal doped TCOs.
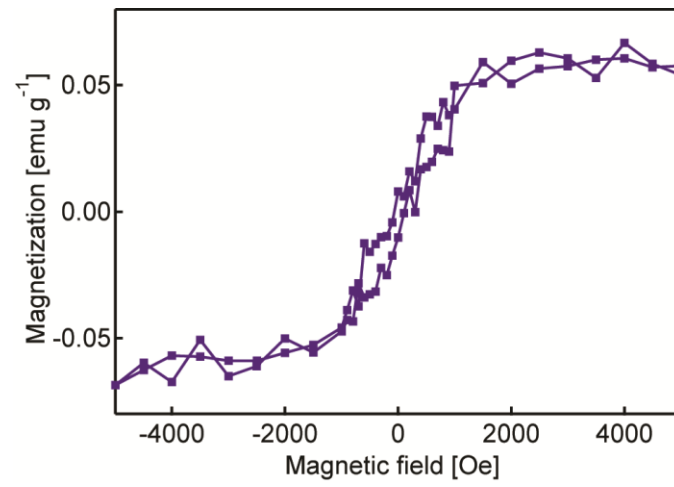
Figure 5.7 Magnetization data at 300 K collected on films of 8.8% Mn^{3+} doped rh-In_2O_3 NCs.

Chapter 6

Colloidal Gallium Indium Oxide Nanocrystals: A Multifunctional Light Emitting Phosphor Broadly-Tunable by Alloy Composition

Gallium oxide (Ga_2O_3) is a polymorphic wide band gap ($E_g \approx 4.9$ eV) material with high n-type conductivity and charge carrier mobility, which originate from the presence of structural defects, particularly oxygen vacancies.[116] Ga_2O_3 occurs in five different allotropic modifications. Colloidal metastable γ-Ga_2O_3 NCs with spinel-type crystal structure can be tuned in the blue part of the spectrum by controlling their size via the synthesis temperature.[6] The fact that both Ga_2O_3 and In_2O_3 are polymorphic materials and have different crystal and electronic structures provides a large number of potential emission-tuning parameters, and the possibility of examining the relationship between size, structure, composition and emission properties of TCO-NCs. In this chapter, we demonstrate a broad tunability of the visible emission by synthesis of ternary gallium indium oxide colloidal NCs throughout the entire composition range.

6.1 Structural Study of Gallium Indium Oxide NCs

The synthesis conditions were developed and optimized to obtain alloyed GIO NCs with Ga_2O_3 and In_2O_3 crystal structures. Figure 6.1 shows X-ray diffraction (XRD) patterns of GIO NCs with different compositions synthesized at 200 °C for 30h. The compositions of GIO NCs were determined by EDX spectroscopy, and are shown in Figure 6.1 as atomic percent (at%) of In. XRD pattern of pure Ga_2O_3 NCs (0 at% of In) matches very well the pattern of metastable γ-Ga_2O_3. Similarly, the NC sample synthesized with $In(acac)_3$ as the only precursor in the reaction mixture (100 at% of In) exhibits crystal structure characteristic for metastable rh-In_2O_3 (corundum-type In_2O_3). XRD peaks for pure In_2O_3 and Ga_2O_3 NCs are narrower and better defined than those for GIO NCs synthesized under identical conditions, which is consistent with an impurity-induced NC lattice disorder and a decrease in average NC size, suggesting that the presence of foreign ions inhibits NC growth even for ions that have similar chemical behavior. As the concentration of In in the reaction mixture approaches that of Ga, the formation of GIO NCs with rh-In_2O_3 structure, in addition to those with γ-Ga_2O_3 structure, becomes evident.

78
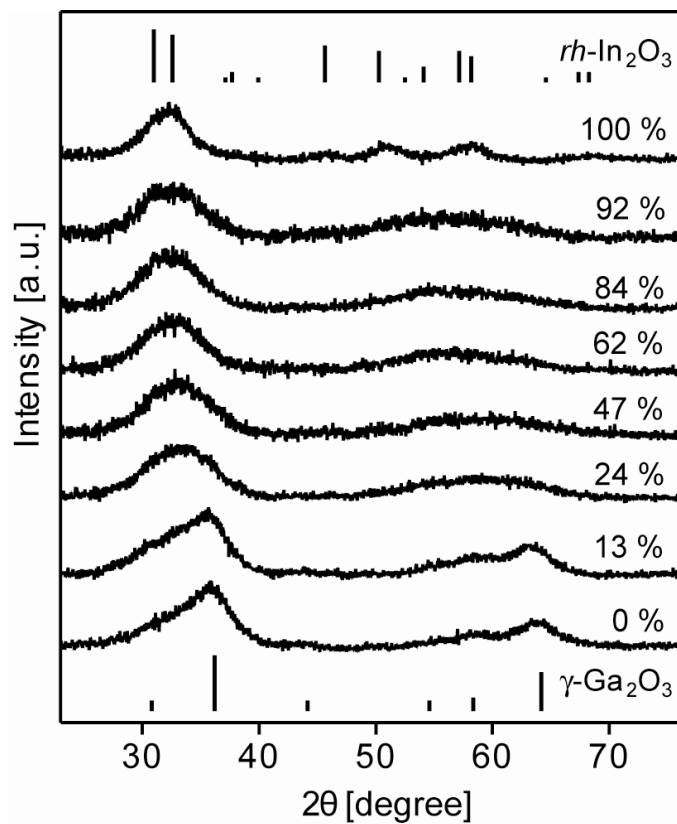
Figure 6.1 XRD patterns of GIO NCs synthesized with different ratios of Ga(acac)$_3$ and In(acac)$_3$ precursors. The percentages indicate the final concentrations of In. The vertical lines represent XRD patterns of bulk γ-Ga$_2$O$_3$ (bottom, JCPDS 20-0426) and rh-In$_2$O$_3$ (top, JCPDS 21-0406).

The presence of GIO NCs with rh-In$_2$O$_3$ structure can be identified in samples with the final In concentration of ca. 25 at%, and they become dominant when In concentration reaches about 50 at%. In this intermediate composition range GIO NCs with both γ-Ga$_2$O$_3$ and rh-In$_2$O$_3$ structures can contribute to PL properties.

6.2 Optical Study of Gallium Indium Oxide

In order to study the optical behavior of GIO NCs with respect to their crystal structure and to distinguish PL of the two metastable phases of mixed oxide NCs, we used the difference in kinetics of In$_2$O$_3$ and Ga$_2$O$_3$ colloidal NCs growth. Synthesis of In$_2$O$_3$ NCs at high temperatures (ca. 250 °C and above) leads to the formation of larger NCs ($\geq$ 10 nm in diameter) with bcc-In$_2$O$_3$ structure, while at lower temperatures (ca. 200 °C) the slower growth favors the formation of small-sized (ca. 3.5 nm) metastable rh-In$_2$O$_3$ NCs (Figure 3.6). On the other hand, Ga$_2$O$_3$ NCs, which grow much slower, are

stabilized in γ-Ga$_2$O$_3$ phase throughout the same temperature range.[6] The XRD patterns of GIO NCs synthesized at 290 °C reflect this difference in the kinetics of In$_2$O$_3$ and Ga$_2$O$_3$ NC growth. The presence of larger In-rich GIO NCs with bcc-In$_2$O$_3$ structure is observed in the samples prepared at 290 °C with higher concentrations of In(acac)$_3$ precursor (Appendix A. 6). However, NCs with bcc-In$_2$O$_3$ structure show negligible emission and the PL properties of these samples arise only from GIO NCs with γ-Ga$_2$O$_3$ structure (*vide infra*).
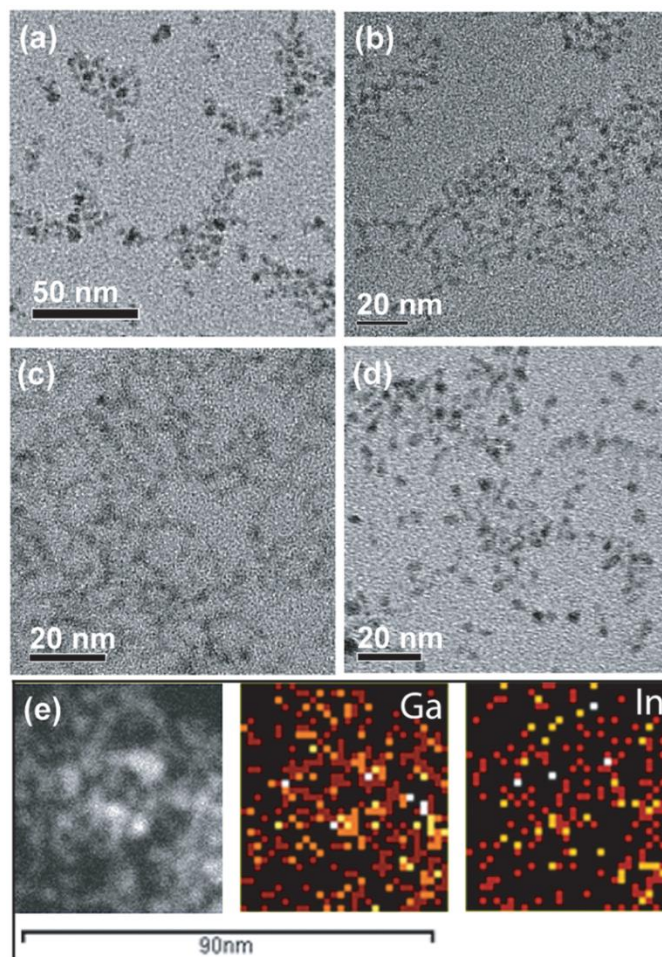
Figure 6.2 (a-d) TEM images of GIO NCs with (a) 5, (b) 24, (c) 47 and (d) 92 at% of In. (e) Scanning TEM (STEM) image of GIO NCs containing 47 at% of In (left panel), and the corresponding EDX elemental maps of Ga (middle panel) and In (right panel) obtained in the STEM mode.

Figure 6.2 shows transmission electron microscopy (TEM) images of GIO NCs with In contents of 5 (a), 24 (b), 47 (c) and 92 at% (d). For similar concentrations of In and Ga, the obtained NCs are

smaller and tend to form a network-like structure, similar to In_2O_3 NCs at the early growth stages. This reduction in size is associated with the suppression of the NC growth in the presence of impurity ions, and is consistent with the XRD data in Figure 6.1. The distribution of constituent elements was examined by EDX elemental mapping. Figure 6.2e shows EDX elemental maps of GIO NCs with 47 at% of In. The images indicate a homogeneous distribution of elements in NCs. This finding was confirmed for other samples regardless of the NC structure.

Absorption spectra of GIO NCs with different compositions are shown in Figure 6.3a. Ga_2O_3 has a larger band gap than In_2O_3. As the amount of In in GIO NCs increases, the onset of the band gap absorption shifts to longer wavelengths, indicating an electronic structure dependence on the NC composition. Ga_2O_3 is a wide band gap semiconductor with a large effective mass of an electron ($m^*_e \approx 0.34m_0$),[117] and as such its band gap energy is independent on the NC size.[6] Substitutional incorporation of In into Ga_2O_3 narrows its band gap, leading to a red shift in band gap absorption. This observation is in agreement with previous findings about alloyed semiconductor NCs.[118] Conversely, GIO NCs having rh-In_2O_3 structure exhibit higher band gap energy compared to pure rh-In_2O_3 NCs (red trace in Figure 6.3a). The electronic band structure is determined by the size of the constituent cations, allowing for band gap and optical property engineering of the NC systems that are not subject to quantum confinement in the experimentally achievable sizes. When excited into band gap, Ga_2O_3 NCs exhibit a broad PL band with a significant Stokes shift.[6] A large Stokes shift suggests a localized (non-band gap) nature of the PL transition, which is in sharp contrast with a typical excitonic recombination transition in quantum dots.[9] This transition has been assigned predominantly to the DAP recombination, where a donor is an oxygen vacancy, and an acceptor is a gallium vacancy or gallium-oxygen vacancy pair.[6] The observed PL band red-shifts as the concentration of In increases in GIO NCs, reaching the lowest emission energy for pure rh-In_2O_3 NCs (Figure 6.3b). This composition dependence allows for continuous tuning of the emission throughout most of the visible spectrum, rendering alloyed GIO NCs promising materials for tunable LEDs. The PL peak energy dependence on the NC composition is plotted in Figure 6.3c. This dependence follows a horizontal sigmoidal shape. The emission energy of GIO NCs initially drops sharply with increasing concentration of In in γ-Ga_2O_3 and then saturates when In content reaches ca. 30 at%. Indium-rich GIO NCs with rh-In_2O_3 structure behave as a mirror image with increasing Ga concentration, although with a narrower tuning range (ca. 2.28-2.45 eV). For similar concentrations of both cations the energies of the PL peaks are essentially the same regardless of the NC structure. The color changes from purple for γ-Ga_2O_3 NCs, via different nuances of blue-green for GIO NCs, to orange for

and rh-In_2O_3 NCs. Figure 6.3d qualitatively demonstrates the composition-induced tunability of GIO NC emission and their potential as inorganic LEDs. Importantly, a decrease in NC size leads to a blue shift of the γ-Ga_2O_3 NC emission, which can be associated with an increase in the Coulombic interactions between donors and acceptors due to a decrease in their average separation.[6] However, the emission peaks of GIO NCs are red-shifted for higher In concentrations in spite of the fact that In^{3+} ions in solution inhibit NC growth.
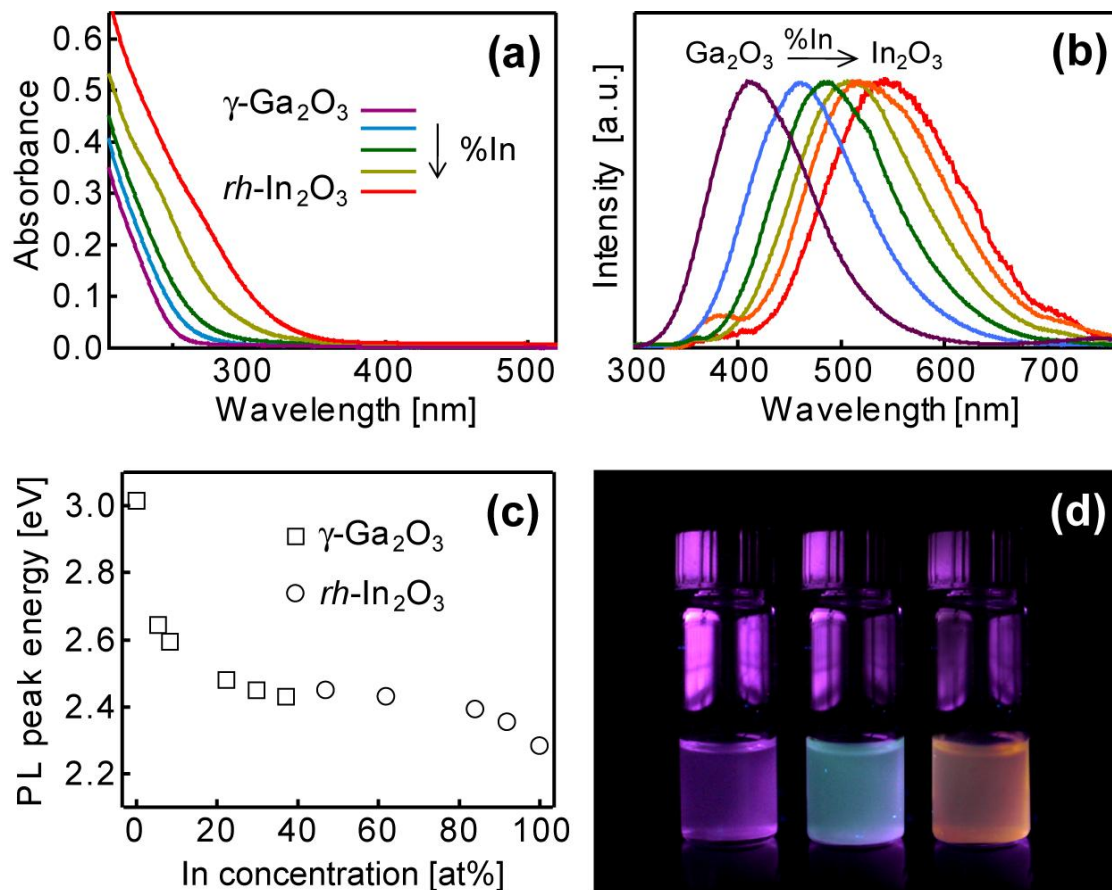
Figure 6.3 (a) Absorption spectra of GIO NCs with varying In content. (b) Photoluminescence spectra of GIO NCs with 0 (purple), 13 (blue), 24 (green), 47 (olive), 84 (orange) and 100 at% In (red) synthesized at 200 °C. (c) Photoluminescence peak energies of GIO NCs as a function of In concentration. Different symbols show the dominant crystal structure of GIO NCs based on XRD data. (d) Photograph of γ-Ga_2O_3 (left) GIO (24 at% In, middle) and rh-In_2O_3 NCs (right) synthesized at 200 °C.

Figure 6.4a compares PL spectra of γ-Ga$_2$O$_3$ NCs prepared at different temperatures. The blue PL band of γ-Ga$_2$O$_3$ NCs synthesized at higher temperature is red-shifted owing to the larger NC sizes and the lower concentration of native defects.[6] The same comparison for GIO NCs having similar compositions (20-25 atom % In) reveals a much smaller difference in the emission energies (Figure 6.4b). Smaller differences in PL band energies of GIO NCs synthesized at different temperatures indicate that the nature of DAP recombination changes with the incorporation of In into γ-Ga$_2$O$_3$ NCs.
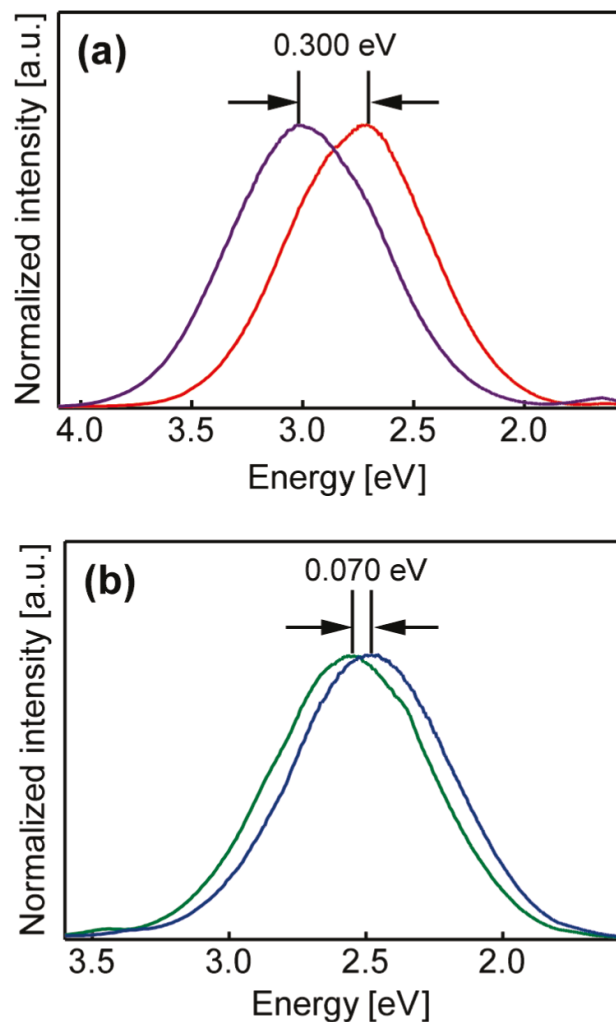
Figure 6.4 (a) PL of 3.3 nm γ-Ga$_2$O$_3$ NCs synthesized at 200 °C (purple) and 6.0 nm γ-Ga$_2$O$_3$ NCs synthesized at 290 °C (red). (b) PL of GIO NCs containing 24 at% In synthesized at 200 °C (green) and 22 at% In synthesized at 290 °C (blue).

Figure 6.5a compares steady state (solid line) and delayed PL spectra (dashed line) of GIO NCs containing 5 at% of In. The delayed PL spectrum was collected 0.1 ms after NC excitation through the band gap.
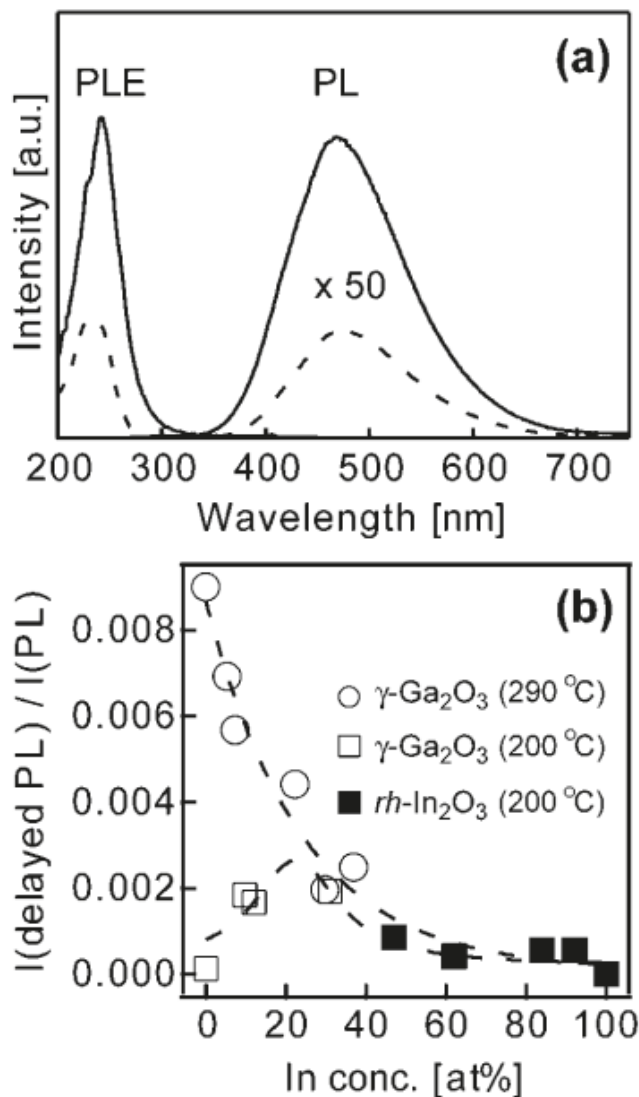
Figure 6.5 (a) Steady-state (solid line) and delayed (dashed line) PL spectra of GIO NCs containing 5 atom % In. The corresponding excitation (PLE) spectra are shown with the same lines. The delayed PL and PLE spectra were collected 0.1 ms after excitation and are multiplied by a factor of 50 for clarity. (b) Ratio of 0.1 ms delayed PL and steady-state PL intensities of GIO NCs as a function of the In content. The synthesis temperatures and the corresponding majority structures of GIO NCs are indicated in the graph. The exponential and Lorentzian function fits are shown as a guide to the eye.

The PL and delayed PL spectra, as well as the corresponding excitation (PLE) spectra, have the same structures and band shapes, confirming that at low-to intermediate In content the observed emission is due to DAP recombination in NCs having the same structure and very similar compositions, rather than subsets of NCs with particular compositions (i.e., Ga-rich and In-rich NCs). The red shift of the delayed relative to the steady-state PL spectrum, which is associated with recombination of more distant donors and acceptors,[6] is much smaller than for pure Ga_2O_3 NCs. This difference suggests stronger delocalization of an electron on a donor in GIO than in Ga_2O_3 NCs. The ratios of delayed PL and PL band intensities are summarized in Figure 6.5b for different In concentrations in GIO NCs prepared at different temperatures. To distinguish the influence of the GIO NC structure and composition on the PL decay dynamics, we measured the intensity ratios of delayed and steady-state PL for Ga-rich NCs prepared at 290 ˚C (open circles) and In-rich NCs prepared at 200 ˚C (filled squares).
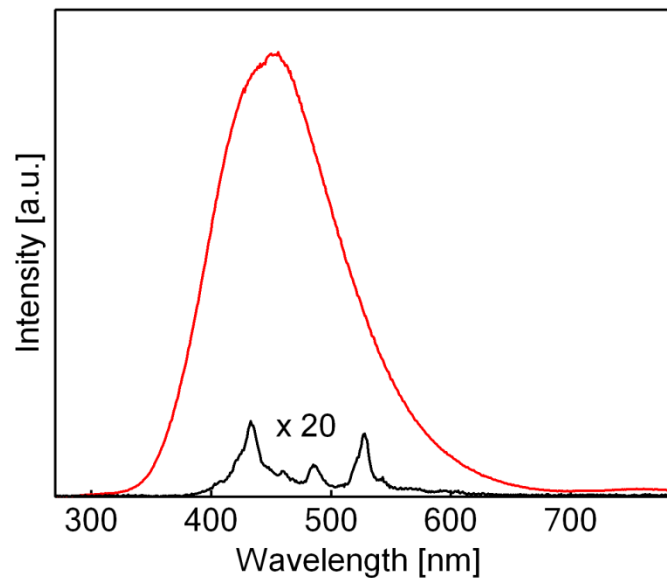
Figure 6.6 Photoluminescence spectra of bcc-In_2O_3 NCs synthesized at 250 °C (black trace). The spectrum is multiplied by a factor of 20 for clarity. Photoluminescence of γ-Ga_2O_3 NCs synthesized under identical conditions (red trace) is shown for comparison.

As mentioned above, the only detected secondary phase in the synthesis at 290 ˚C is bcc-In_2O_3-type GIO NCs, which show a negligible emission (Figure 6.6). The PL spectra of these samples come from GIO NCs with γ-Ga_2O_3 structure. On the other hand, for the samples synthesized at 200 ˚C PL is due to NCs with both γ-Ga_2O_3 and rh-In_2O_3 structures, depending on the NC composition.

The intensity ratios (delayed PL/PL) for NCs synthesized at 290 ˚C decrease exponentially with increasing concentration of In (Figure 6.5b, open circles). These data further suggest a change in the nature of the DAP emission of γ-Ga_2O_3-type NCs with increasing incorporation of In. An interesting comparison is the relationship between delayed and steady-state PL intensities for GIO NCs with γ-Ga_2O_3 structure prepared at 200 ˚C (Figure 6.5b, open squares) and 290 ˚C (open circles). A sharp decrease in the delayed PL intensity is observed for NCs prepared at the lower temperature. This increase in the PL decay rate is associated with shorter donor-acceptor distances in NCs obtained at lower synthesis temperatures.[6] As the concentration of In becomes larger the delayed PL/PL ratio for NCs synthesized at lower temperature approaches that of NCs synthesized at higher temperature.

The quantum yield values for the samples in Figure 6.5b are shown in Figure 6.7. For γ-Ga_2O_3 NCs the quantum yield is ca. 20%, and it drops exponentially with increasing In content.
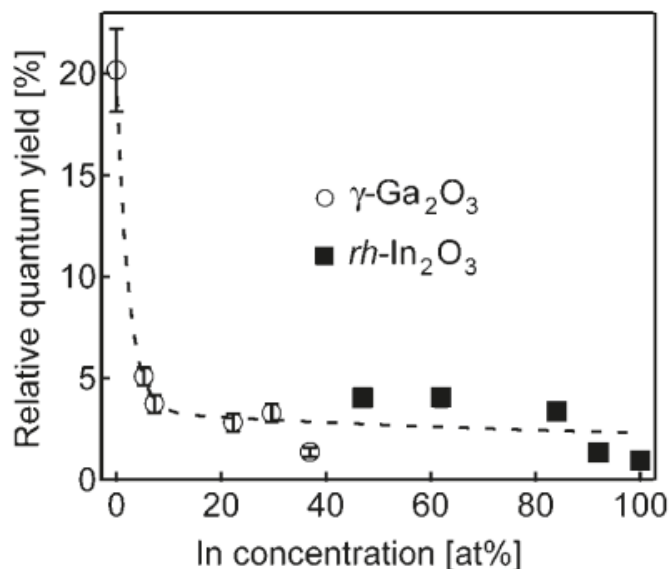
Figure 6.7 Indium concentration dependence of the relative quantum yield for GIO NCs having different crystal structures as labeled in the graph. The dashed line is an exponential fit to the experimental data points.

This trend is also consistent with a different nature of PL in alloyed GIO relative to pure Ga_2O_3 and In_2O_3 NCs. The development of LEDs that emit white light has attracted much attention lately for their potential use in the next generation of displays and as lighting sources. The broad tunability,

large-emission Stokes shifts, and long lifetimes render GIO NC-based phosphors potentially promising materials for the design of white light emitters.

6.3 EXAFS Study of Gallium Indium Oxide

To obtain quantitative information about the local environment of In sites, we conducted a systematic XAS study of photoluminescent GIO NC samples having different In concentrations. Normalized In K-edge X-ray absorption spectra of GIO and rh-In_2O_3 NCs in the full spectral range are shown in Figure 6.8. A direct comparison between the spectra of GIO and rh-In_2O_3 NCs in the near edge region confirms that indium ions have +3 oxidation state in GIO NCs.
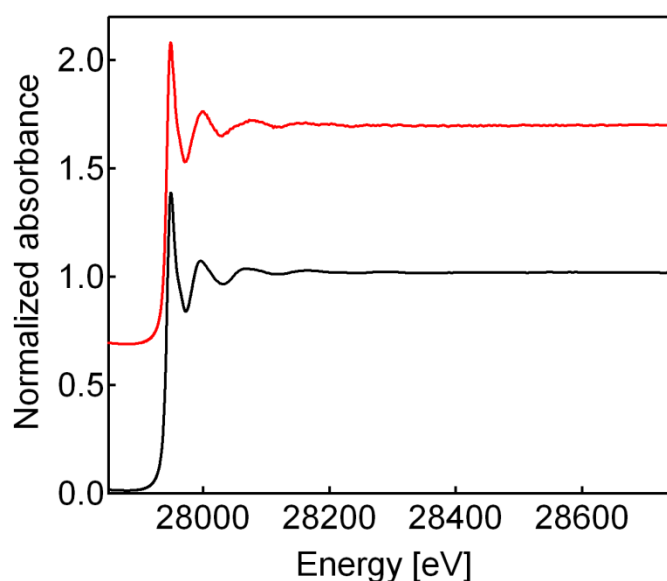
Figure 6.8 Normalized In K-edge X-ray absorption spectra of rh-In_2O_3 (black trace) and GIO NCs containing 10 % In (red trace), synthesized at 200 °C. The spectrum of GIO NCs is intentionally offset along *y*-axis for clarity.

Figure 6.9a shows the *k*-weighted In K-edge EXAFS spectra of GIO NCs having different compositions, synthesized at 200 °C. The spectrum of rh-In_2O_3 NCs is also shown for comparison. The spectra were Fourier transformed from *k*-space to R-space in the 2.40-10.56 Å^{-1} region. The resulting pseudo-radial distribution functions are shown in Figure 6.9b. The first prominent peak centered at ca. 1.6 Å is due to backscattering of the ejected photoelectron from the first coordination shell of the neighboring oxygen atoms (In-O), while the second peak at ca. 3.0 Å is less pronounced and corresponds to the second shell of cation sites. The inverse Fourier transform of the first (R=1.0-2.2 Å) and second shell (R=2.45-3.60 Å) of the pseudo-radial distribution functions gives the Fourier-

filtered EXAFS spectra which are shown in Figure 6.10. The bond-distances obtained from the single-shell analysis were used as initial parameters to perform the inverse Fourier transform of the pseudo-radial functions in the full range (R=1.0-3.6 Å), and obtain Fourier-filtered EXAFS spectra (Figure 6.9c, solid lines). The Fourier-filtered curves were fit well in the k-range of 2.40-10.56 Å^{-1} with two shells (Figure 6.9c, dashed lines).
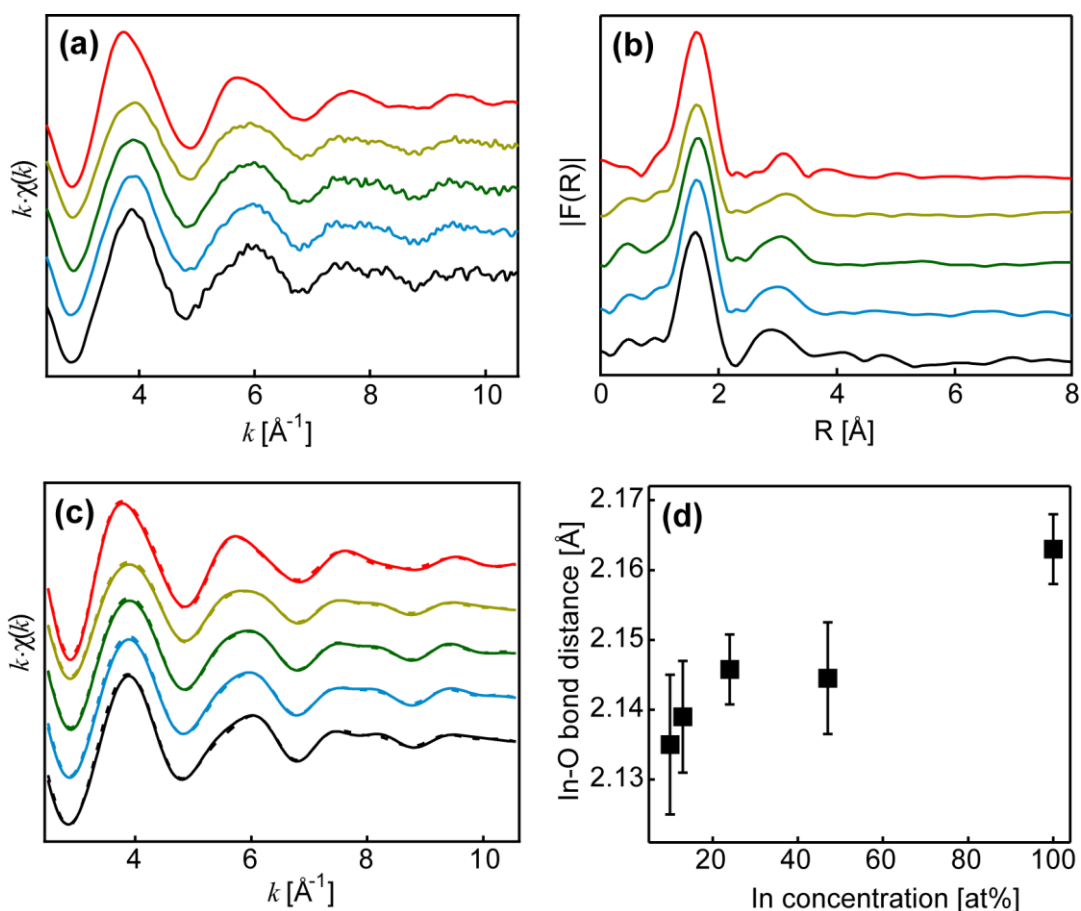
Figure 6.9 (a) In K-edge k-weighted EXAFS spectra of GIO NCs with different compositions synthesized at 200 ˚C. (b) Pseudoradial distribution functions obtained by Fourier transformation of the spectra in (a). (c) Fourier-filtered EXAFS spectra obtained by the inverse Fourier transform of the radial functions in (b) in the range $R = 1.0$-3.6 Å (solid lines) and the corresponding curve fits (dashed lines) from which the structural parameters were calculated. (d) In-O bond distances, determined from the EXAFS analysis, as a function of the In concentration in GIO NCs. The spectra in (a) - (c) correspond to In concentrations of 10 (black), 13 (blue), 24 (green), 47 (olive), and 100 (red) atom %.
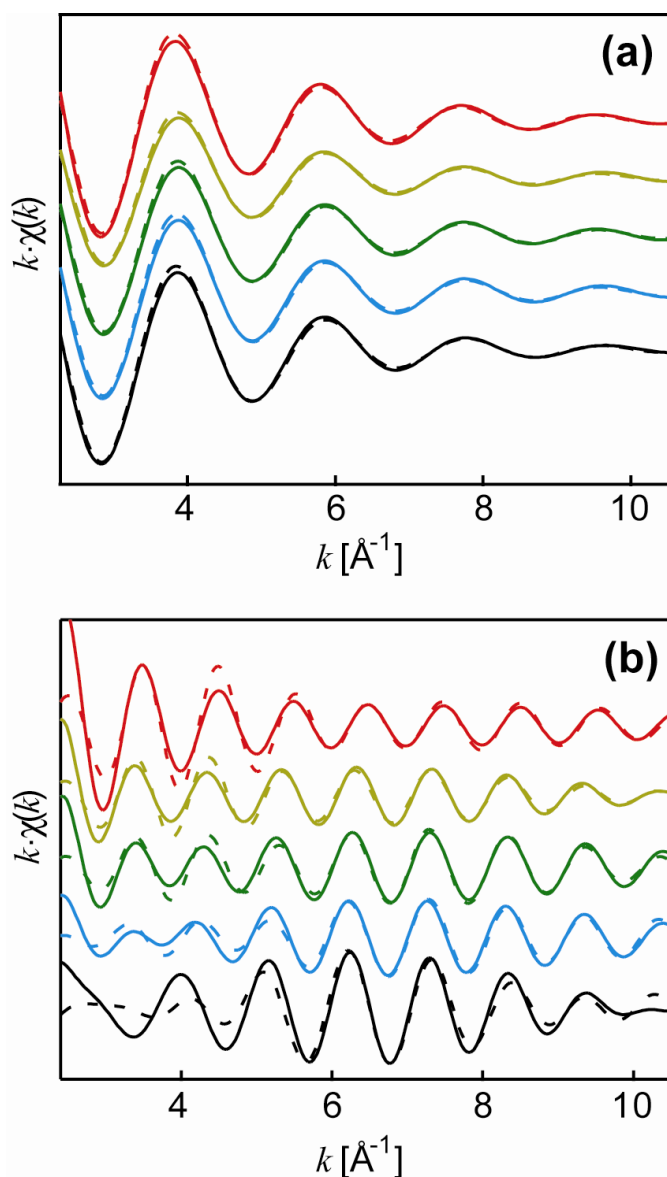
Figure 6.10 Fourier-filtered EXAFS spectra of the first shell (a) and the second shell (b). The corresponding curve fits from which the structural parameters were calculated are shown with dashed lines.

Table 6.1 summarizes the structural parameters for the In-O and In-Ga (or In-In) shells obtained from the curve-fitting. For rh-In_2O_3 NCs the fitting results suggest In^{3+} coordination with 6 oxygen atoms, with an average In-O bond distance of 2.15±0.01 Å. These results are in good agreement with the crystallographic data, from which the average In-O bond length was determined to be 2.17 Å.[119]

Table 6.1 Fitting parameters obtained from the analysis of EXAFS spectra of GIO NCs synthesized at 200 °C having different In content. The standard deviation for In-O bond distances is shown as error bars in Figure 6.9d

In [%]	In-O			In-Ga			In-In			ρ^b [%]
	N	R [Å]	σ^2 [Å^2]	N	R (Å)	σ^2(Å^2)^a	N	R (Å)	σ^2(Å^2)	
10	5.8	2.135	0.0082	4.9	3.053	0.020	0.9	3.356	0.0040	0.6
13	5.3	2.139	0.0071	2.7	3.063	0.020	1.0	3.349	0.0041	0.6
24	5	2.145	0.0066	2.0	3.051	0.020	1.2	3.330	0.0054	0.4
47	4.5	2.144	0.0077	0.2	3.040	0.000	1.3	3.343	0.0065	0.5
100	6	2.163	0.0073	—	—	—	2.1	3.252	0.0130	0.5

^{a} Debye-Waller factor. ^{b} Weighted residual factor.

Metastable γ-Ga$_2$O$_3$ has been reported to have a defective spinel-type cubic crystal structure, similar to that of γ-Al$_2$O$_3$, with octahedral and tetrahedral cationic sites.[120, 121] Majority of Ga^{3+} cations have octahedral coordination, in the ratio Ga$^{3+}(T_d)$/Ga$^{3+}(O_h) \approx 0.6$.[121, 122] The average bond distances for Ga-O shell in γ-Ga$_2$O$_3$ were reported to be 1.88 and 2.00 Å for tetrahedral and octahedral sites, respectively.[122] Understanding the substitutional occupancy of the two sites for different In^{3+} concentrations is, therefore, critical for understanding the optical properties of the complex GIO NCs. EXAFS analysis presented in Table 6.1 shows that the average In-O bond distances in all GIO NC samples are shorter than those in pure rh-In$_2$O$_3$ NCs due to substitution of In^{3+} in γ-Ga$_2$O$_3$ or Ga^{3+} in rh-In$_2$O$_3$ NCs, both of which result in the reduction of In-O distances. We plotted the In-O bond distances as a function of In content in GIO NCs in Figure 6.9d. An increase of In-O bond distances with increasing In concentration in GIO NCs is accompanied by a decrease in the coordination number (N). At low concentration of In (10 at%) N is determined to be 5.8, indicating the In^{3+} initially occupies octahedral sites. With increasing concentration of In, N becomes lower, reaching the value of 4.5 at 47 at% In. This decrease in the coordination number could be due to increased occupancy of the tetrahedral sites by In^{3+}, or a local structural disorder due to In^{3+} incorporation and/or decrease in NC size. It has been previously reported that in bulk solid solutions In^{3+} substitutes for octahedral Ga^{3+} in β-Ga$_2$O$_3$, for In concentrations below 44 at% at 1000 °C.[123] Further increase in In concentration up to 95 at% leads to the formation of both β-Ga$_2$O$_3$ and bcc-In$_2$O$_3$ phases with different

compositions. Above 95 at% In, Ga^{3+} substitutes for In^{3+} in the bcc-In_2O_3 phase. β-Ga_2O_3 has a monoclinic structure in which half of the Ga^{3+} cations occupy octahedral and the other half tetrahedral sites. This structural consideration in conjunction with the In solubility in bulk β-Ga_2O_3 (44 %) indicates that In^{3+} replaces most of the octahedrally coordinated Ga^{3+} sites in β-Ga_2O_3, before undergoing phase separation.[123] The extracted data from EXAFS show a small gradual increase in In-O bond distances for In concentration below 24 at%, due to incorporation of In^{3+} in γ-Ga_2O_3 structure (Figure 6.9d). As the concentration of In approaches that of Ga, the average In-O bond distance becomes nearly constant, although the apparent coordination number still decreases (Table 6.1). This increase in the average bond distance cannot be explained by the In^{3+} occupation of the smaller tetrahedral sites, and is associated with a slight expansion of the Ga_2O_3 NC host lattice with increasing In content. The decrease in the apparent coordination number, N, therefore suggests a distorted local environment around In^{3+}, which can be associated with incorporation of a foreign ion or contribution from the surface sites. At high concentrations of In (above 50 at%), the In-O bond distances increase again, finally reaching the value for pure rh-In_2O_3. EXAFS results for the second shell support these findings. The coordination number of Ga (N_{In-Ga}) decreases simultaneously with an increase in the coordination number of In (N_{In-In}), indicating substitutional incorporation of In^{3+}. The EXAFS results are in agreement with the XRD results for GIO NCs synthesized at 200 °C. At low concentrations of In only NCs with γ-Ga_2O_3 structure were formed. Upon increasing the concentration of In above 24 at% the rh-In_2O_3 phase becomes evident in addition to the γ-Ga_2O_3. From these data we conclude that In^{3+} occupies only octahedral sites in Ga_2O_3 until reaching saturation limit (ca. 25 %). Further increase in the In precursor concentration leads to the phase segregation and formation of rh-In_2O_3 phase coexisting with γ-Ga_2O_3.

These results are also in agreement with the dependence of the PL energies on In concentration in GIO NCs (Figure 6.3c). The emission energy decreases sharply with increasing In concentration up to ca. 30 at%, and then remains unchanged until rh-In_2O_3 becomes the majority phase. It should be noted that the shift of the PL band of GIO NCs with γ-Ga_2O_3 structure is significantly more dependent on the concentration of impurity ions than that of the NCs with rh-In_2O_3 structure. This structural analysis allows for a rational design of complex oxide NCs with targeted photonic properties based on the occupancy of the available crystal lattice sites.

6.4 Proposed Mechanism for Photoluminescence

Figure 6.11 schematically depicts the origin of the emission in tunability of GIO NCs, on the basis of the results in this work and the previous reports.[6, 124-126] The blue emission in Ga_2O_3 has been explained by the DAP recombination (Figure 6.11, left part). Theoretical work by Maximenko *et al*. has suggested that recombination of an electron on the localized isoelectronic dopant levels within the band gap with a valence band hole may be a possible source of green emission in Ga_2O_3.[126] The energies of such dopant impurity sub-band gap states are sensitive to the NC composition as well as the band gap width (the incorporation of In^{3+} narrows the band gap, as demonstrated in Figure 6.3a) and are expected to become lower following a decrease in the band gap energy. Another possible explanation for the red shift of the GIO NC emission, and the one favored in this thesis, is the changing nature of the DAP recombination with the incorporation of In^{3+} (Figure 6.11,right).
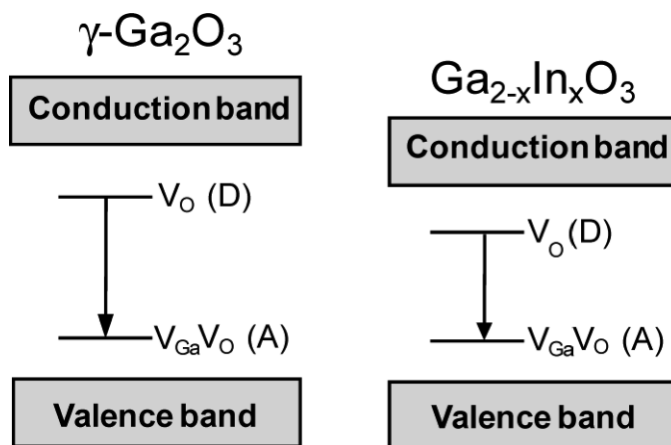
Figure 6.11 Schematic representation of the possible origin of photoluminescence in undoped γ-Ga_2O_3 NCs (left) and GIO NCs with a γ-Ga_2O_3 structure (right) based on the findings in this work and the evidence previously reported (see the text). The radiative transitions (DAP recombination) are indicated by arrows, and the labels correspond to the defect species described in the text.

The energy states of the donors and acceptors also follow a reduction in the band gap of GIO NCs, leading to a continuous red shift of the DAP PL band with increased substitutional incorporation of In^{3+}. Furthermore, the average Bohr radius of the donor electrons should also increase with increasing In^{3+} incorporation (i.e., they become more delocalized), favoring faster DAP recombination and a decrease in the delayed PL intensity. The efficiency of the DAP recombination in GIO NCs may be lower than that in pure Ga_2O_3 NCs due to the change in the local environment of the oxygen vacancies or a decrease in the concentration of the gallium and oxygen vacancy sites. This

explanation for the red shift of the PL band of GIO NCs would also be consistent with a similar broadening of the PL spectra in Figure 6.3b. At a sufficiently high In precursor concentration (>50 atom % with respect to Ga) GIO NCs adopt rh-In_2O_3 structure.

However, the origin of PL in In_2O_3 is much less understood. Some literature reports propose that radiative recombination of a photoexcited hole in the valence band with an electron occupying sub-band gap oxygen vacancy states is responsible for the deep-level emission in In_2O_3.[127] Other authors suggest the DAP mechanism involving oxygen and indium vacancies, as described above for Ga_2O_3.[128]
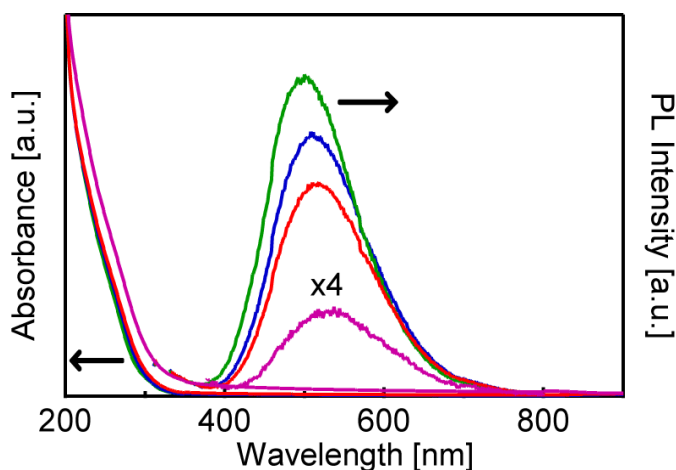
Figure 6.12 Absorption and PL spectra of colloidal rh-In_2O_3 NCs synthesized at 200 ˚C for 1 (green), 4 (blue), 7 (red) and 30 (purple) hours. The spectra correspond to the same concentration of NCs. The spectrum of the sample synthesized for 30 h is shown multiplied by a factor of 4.

Absorption and PL spectra of colloidal rh-In_2O_3 NCs synthesized for different durations at 200 ˚C are shown in Figure 6.12. The PL bands are rather broad and exhibit large Stokes' shifts. With increasing synthesis time the PL intensity decreases and the emission band shifts to lower energies. The PL intensity of the sample synthesized for 30 h is ca. 15 times smaller than the intensity of the sample synthesized for 1 h. The decrease in the PL intensity accompanied by the red shift of the emission band can be attributed to an increase in the average donor-acceptor separation due to a decrease in the concentration of defects by NC annealing in solution similarly to colloidal Ga_2O_3 NCs. The PL properties of rh-In_2O_3 NCs are significantly different from those of bcc-In_2O_3 NCs, which show no such emission when synthesized by the described colloidal method. This difference is likely associated with a lower concentration and/or different structure of defect sites in colloidal bcc-

In$_2$O$_3$ NCs. It should also be noted that the synthesis conditions and the size of polymorphic NCs play a very important role in determining the defect electronic structure and PL properties. We believe that the higher synthesis temperatures lead to a significantly lower concentration of defect sites in bcc-In$_2$O$_3$ compared to rh-In$_2$O$_3$ NCs in the present work. In addition, our results suggest that defect formation in metastable rh-In$_2$O$_3$ NCs prepared under the described conditions is more favorable than in bcc-In$_2$O$_3$ NCs.

Chapter 7
Conclusions and Future Work

7.1 Conclusions

The studies performed throughout this thesis elaborate on the manipulation of crystal phase and physical properties in colloidal In_2O_3 NCs. Structural transformations in NCs have previously been achieved at high pressures or temperatures, and studied as a function of these parameters. We demonstrated that NC phase transformations can be achieved in solution by controlling the NC growth conditions and sizes. In addition, we studied the kinetics of phase transformation of rh-In_2O_3 to bcc-In_2O_3 NCs during colloidal synthesis. The kinetic data based on XRD and EXAFS measurements were investigated in the framework of JMAEK and interface nucleation models. The activation energy of phase transformation under isothermal conditions was found to be in excellent agreement for these two analyses ($E_a \approx 152$ kJ/mol). Correlation of the kinetic results with TEM imaging of the product at different points in time during the reaction suggests that the phase transformation occurs by nucleation of bcc-In_2O_3 at the interfaces between contacting rh-In_2O_3 NCs. The nucleation rate reaches the maximum at an early stage of the reaction and consequently decreases due to a decrease in the concentration of small rh-In_2O_3 NCs in the reaction mixture. The rate of phase transformation is critically dependent on both NC size and concentration; it increases with increasing concentration and decreasing size, owing to a higher probability of NC contact formation. Upon the nucleation of bcc-In_2O_3, which most likely occurs at the interfacial defect sites, the growth of the new phase propagates at a time scale much shorter than that examined in this study. This work demonstrates that phase transformation of In_2O_3 NCs in solution is a kinetically controlled process, and provides greater understanding of the growth and phase transformation mechanism of oxide NCs. The results of this study allow for a rational manipulation of the NC surfaces and their interactions by controlling the reaction conditions, such as time and temperature, enabling the synthesis of colloidal NC building blocks with a desired crystal structure and properties. These findings can be applied to other materials that exhibit metastability, allowing for an expansion of the available NC building blocks through simple chemical approaches.

We showed that dopant ions can be generally used to control and manipulate size and crystal structure of colloidal free-standing In_2O_3 NCs. Metastable rh-In_2O_3, which is the transient species in the formation of bcc-In_2O_3 NCs, can be stabilized for NCs smaller than 5 nm by adsorption of

transition-metal impurities and subsequent inhibition of the NC growth. The incorporation of transition-metal ions critically depends on their average residence time on different NC surface binding sites, which is directly related to the average heat of adsorption of dopant ions on the NC surfaces. We experimentally identified the structural similarity between the dopant transition-metal oxide and the In_2O_3 host crystal lattices as a key component determining the affinity of dopant ions for the incorporation into NCs. It is important to note that bonding between the dopant ions and the coordinating ligands, such as electron pair donor/acceptor interactions, should also play a significant role in the process of dopant ion binding to the NC surfaces and their incorporation. These bonding interactions impact the stability of dopant-surface site bonds, which would directly influence ΔH_{ads}. Such considerations were not a subject of the current work, which was performed in the same chemical environment, focusing on the relative comparison of dopant incorporation into different host lattice polymorphs. Our approach enables a new way of simultaneously controlling the NC structure and doping in the solution phase, which can be applicable to both synthetic and natural systems. In a broader context, our results emphasize that the size, structure, and morphology of the crystallites at the early growth stages all critically dependent on the presence and concentration of impurities, and colloidal NCs can serve as a model system for studies and control of the crystal growth in such conditions. The paramagnetic $TM:In_2O_3$ exhibit room temperature ferromagnetism when spin-coated into the film which is attributed to the formation of extended structural defects, proposed to be oxygen vacancies at the NC interfaces. Colloidal methods and the size-structure dependence allow for accessibility, precise tuning, and separation of different NC phases and therefore a convenient engineering of the relevant properties of TCO NCs in an effective way. The MCD spectra reveal that Cr^{3+} ions occupy the C_2 symmetry sites in $bcc-In_2O_3$ which is distinctly different from the C_{3v} symmetry sites for Cr^{3+} ions in $rh-In_2O_3$.

In addition, we demonstrated the structure and composition dependences of the PL properties of colloidal gallium indium oxide NCs. These dependences can be used to achieve a wide tunability of PL in the visible region of the spectrum. The increasing concentration of In in GIO NCs leads to band gap narrowing and a systematic red-shift of PL. A comparison between the emission energies and efficiencies, and the decay rates of $\gamma-Ga_2O_3$ and GIO NCs suggests that the emission peak shifts to lower energies with increasing indium content owing to the changes in the energy states of the donors and acceptors and their interactions. EXAFS analysis strongly suggests that In^{3+} is selectively substituted for octahedral Ga^{3+} in metastable $\gamma-Ga_2O_3$, which has a spinel-type structure. The changes in the electronic structure of defects, induced by changes in NC structure and composition, allow for

wide-range tuning of the photoluminescence properties. These defects are also responsible for other functional properties of TCOs, particularly conductivity, and the ability to control both structure and composition provides new degrees of freedom, and a path for enhancement of the inherent functionalities of complex TCOs-NCs. Multifunctionality, achieved in this way, can enable the application of alloyed TCO-NCs as integrated optoelectronic materials.

7.2 Future Work

We have demonstrated that dopant ions can be generally used to control and manipulate size and crystal structure of colloidal free-standing In_2O_3 NCs and that the presence of dopant ions profoundly influences the growth, optical and magnetic properties of the host lattice. Thermodynamic and kinetic study of dopants incorporated in the nanocrystal can provide deeper understanding of dopant incorporation mechanism in doped nanomaterials. All these results enable manipulation of the relevant properties in these materials. The incorporation of transition-metal ions critically depends on their average residence time on different NC surface binding sites, which is directly related to the average heat of adsorption of dopant ions on the NC surfaces. As a next step, thermal gravimetric analysis (TGA) and differential scanning calorimetry (DSC) analysis could be used to measure the heat of absorption of dopant ions on the NC surfaces, and their miscibility in the host lattice in each crystal structure of In_2O_3 NCs.

In addition, thermodynamic stability studies of transition metal oxide using calorimetric data on surface energies for cobalt, iron, manganese, and nickel oxide systems, has revealed that nanoparticle redox reactions is energetically different from the bulk.[129] Since redox reactions of dopants may have an important role for the observed magnetism in semiconductors, it is of particular interest to investigate the effects of oxidation state of the dopant on the observed ferromagnetism. In Chapter 4, we shown that nanocrystalline films fabricated from colloidal chromium and manganese doped In_2O_3 nanocrystals exhibit strong ferromagnetic ordering up to room temperature. Samples include manganese-doped In_2O_3 nanocrystals which were synthesized with different Mn^{2+} to In^{3+} molar ratios (5%-15%). Manganese can be oxidized from Mn^{2+} to Mn^{3+} during the reactions and this process can produce unknown molar ratios of Mn^{2+} to Mn^{3+}. In the next step, quantifying these molar ratios of oxidation states of manganese as well as electronic structure and local coordination environment around dopant ions is particular of interest. X-ray absorption spectroscopy (XAS) is a powerful technique in both X-ray absorption near edge structure (XANES) and extended X-ray absorption fine structure (EXAFS) regions in order to determine metal-oxidation and spin states, nature and number

of neighbors and metal-ligand distances. An XANES study of Mn L- and K-edge can be used to determine the oxidation state of Mn in the NCs. In addition, extended grain boundary defects formed at the interfaces of NCs in their films are a key factor in mediating dopant interactions, through charge carrier formation. Circularly polarized scanning transmission X-ray microscopy (STXM) imaging at nanoscale can provide the ability to directly correlate the location of the dopants (with respect to the grain boundaries) with magnetization properties in nanostructure arising from the presence of dopants. In these experiments, a monoenergetic X-ray beam (ca. 30 nm in diameter) is focused on a particular area of the sample, and an image is generated by monitoring the transmitted X-ray signal as the specimen is raster-scanned at the focus of the X-rays. These experiments will be followed by X-ray magnetic circular dichroism (XMCD) studies of both Cr-and Mn-doped In_2O_3 nanocrystalline films. The dependence of XMCD intensity (and therefore magnetization) on the structure of nanocrystalline domains and the corresponding electronic/oxidation state of dopants should be established. Similar measurements will be made at the O K-edge to determine the interaction between dopant ions and NC valence band (mostly O in character). All of this work can help enhance the understanding of the microscopic origins of ferromagnetism in wide band gap semiconductor nanostructures, and lead to improved magnetic and electrical properties of these materials with significant promise in electronic and alternative energy technologies.

Appendix A

The figures shown in Appendix A.1-A.3 are the supporting information for the data presented in Chapter 3. Appendix A.4, Appendix A. 5, and Appendix A. 6 are the supporting information for the data presented in Chapter 4, Chapter 5, and Chapter 6, respectively.
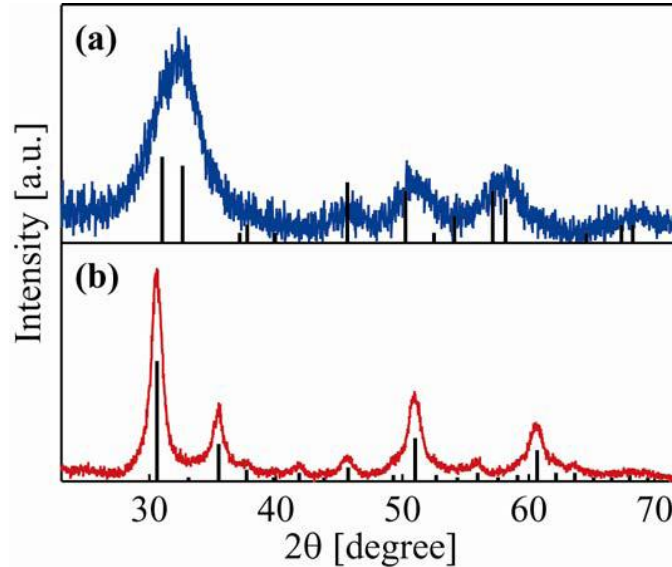
Appendix A. 1 (a) XRD pattern of In_2O_3 nanocrystals synthesized at 200 °C for 30 hours without any water added to the original reaction mixture (data from Figure 3.6a). Black lines represent the XRD pattern of bulk rh-In_2O_3. Similar data were obtained by adding sub-stoichiometric amounts of water with respect to In(acac)$_3$. (b) XRD of In_2O_3 nanocrystals synthesized at 200 °C for only 1 h with added excess water (ca. 10 times the molar amount of In(acac)$_3$). Black lines represent the XRD pattern of bulk bcc-In_2O_3. The obtained nanocrystals have exclusively bixbyite-type structure. These data indicate that the amount of water determines the nanocrystal growth kinetics, and therefore the obtained phase. Sub-stoichiometric amounts of water result in rh-In_2O_3 NCs, while a large excess of water speeds up the reaction under identical conditions resulting in bcc-In_2O_3 nanocrystals.
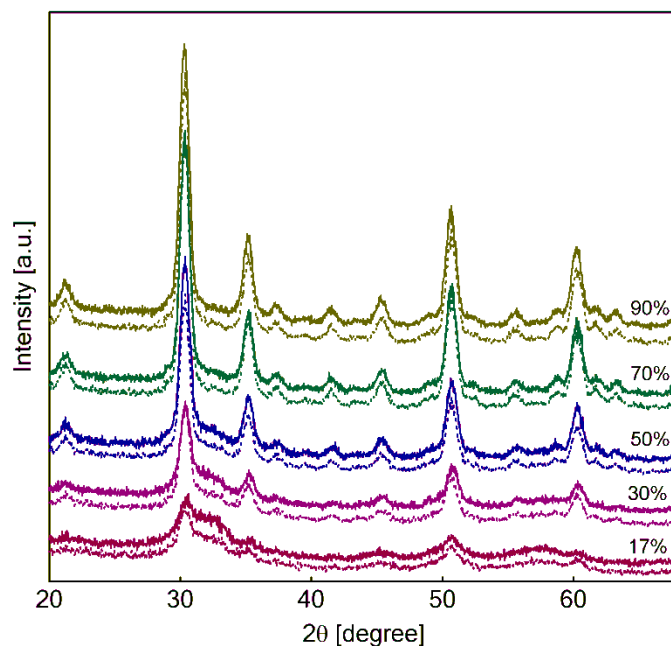
Appendix A. 2 Measured XRD patterns of mixed rh-In_2O_3 and bcc-In_2O_3 NC references (solid lines) and the corresponding simulated XRD patterns derived as the linear combination of the references (dotted lines). The percentages shown indicate the content of bcc-In_2O_3 phase in the samples.
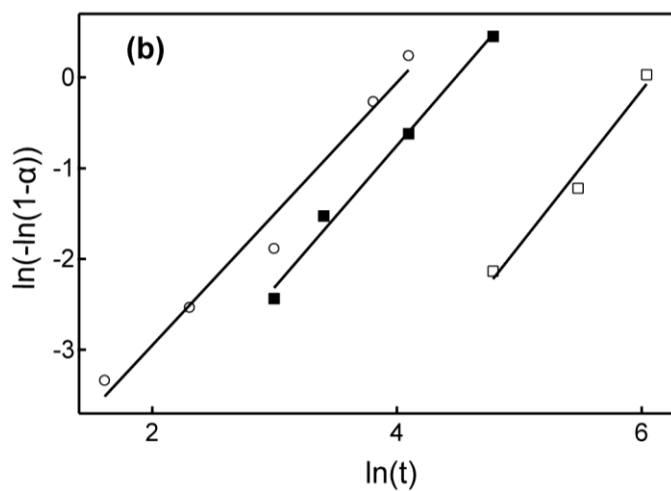
Appendix A. 3 Linear fit to the JMAEK equation for different fractions of the bcc-In_2O_3 phase. open square (220 °C), solid square (230 °C), and open circle (250 °C)
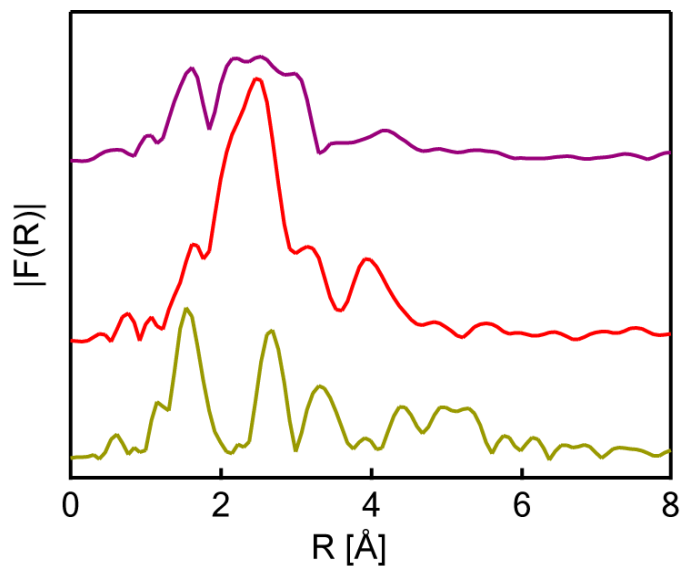
Appendix A. 4 Fourier transform EXAFS spectra of Cr_2O_3 (olive line), rh-$In_{1.667}Cr_{0.333}O_2$ (red line), and bcc-$In_{1.942}Cr_{0.058}O_2$ (purple line)
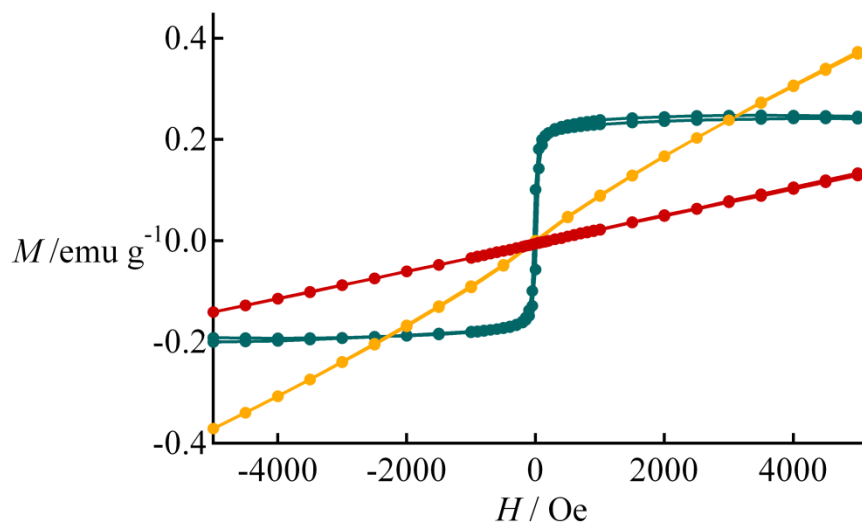
Appendix A. 5 M vs. H data for nanocrystalline Cr_2O_3 measured at 5 K (blue-green dots), 100 K (yellow dots) and 300 K (red dots). No ferromagnetic ordering is observed at 300 K, while the sample is superparamagnetic at 5 K and very weakly superparamagnetic at 100 K.
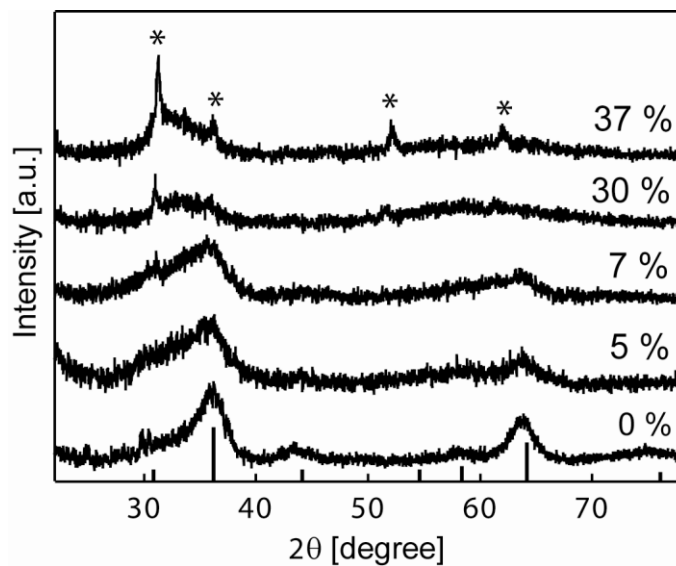
Appendix A. 6 XRD patterns of GIO NCs with different compositions synthesized at 290 °C. The percentages indicate the final doping concentrations of In in at%. The vertical lines at the bottom represent the XRD pattern of bulk γ-Ga_2O_3 NCs (JCPDS 20-0426). The stars indicate the peaks corresponding to GIO NCs having bcc-In_2O_3 crystal structure.

Permissions

Copyright Clearance Center

RightsLink®

ACS Publications
High quality. High impact.

Title: Colloidal Chromium-Doped In2O3 Nanocrystals as Building Blocks for High-TC Ferromagnetic Transparent Conducting Oxide Structures

Author: Shokouh S. Farvid et al.

Publication: The Journal of Physical Chemistry C

Publisher: American Chemical Society

Date: Nov 1, 2008

Copyright © 2008, American Chemical Society

PERMISSION/LICENSE IS GRANTED FOR YOUR ORDER AT NO CHARGE

This type of permission/license, instead of the standard Terms & Conditions, is sent to you because no fee is being charged for your order. Please note the following:

Copyright Clearance Center

RightsLink®

ACS Publications
High quality. High impact.

Title: Dopant-Induced Manipulation of the Growth and Structural Metastability of Colloidal Indium Oxide Nanocrystals

Author: Shokouh S. Farvid et al.

Publication: The Journal of Physical Chemistry C

Publisher: American Chemical Society

Date: Sep 1, 2009

Copyright © 2009, American Chemical Society

PERMISSION/LICENSE IS GRANTED FOR YOUR ORDER AT NO CHARGE

This type of permission/license, instead of the standard Terms & Conditions, is sent to you because no fee is being charged for your order. Please note the following:

- Permission is granted for your request in both print and electronic formats.
- If figures and/or tables were requested, they may be adapted or used in part.
- Please print this page for your records and send a copy of it to your publisher/graduate school.
- Appropriate credit for the requested material should be given as follows: "Reprinted (adapted) with permission from (COMPLETE REFERENCE CITATION). Copyright (YEAR) American Chemical Society." Insert appropriate information in place of the capitalized words.
- One-time permission is granted only for the use specified in your request. No additional uses are granted (such as derivative works or other editions). For any other uses, please submit a new request.

ACS Publications
High quality. High impact.

Title:	Phase-Controlled Synthesis of Colloidal In2O3 Nanocrystals via Size-Structure Correlation
Author:	Shokouh S. Farvid et al.
Publication:	Chemistry of Materials
Publisher:	American Chemical Society
Date:	Jan 1, 2010

Copyright © 2010, American Chemical Society

PERMISSION/LICENSE IS GRANTED FOR YOUR ORDER AT NO CHARGE

This type of permission/license, instead of the standard Terms & Conditions, is sent to you because no fee is being charged for your order. Please note the following:

- Permission is granted for your request in both print and electronic formats.
- If figures and/or tables were requested, they may be adapted or used in part.
- Please print this page for your records and send a copy of it to your publisher/graduate school.
- Appropriate credit for the requested material should be given as follows: "Reprinted (adapted) with permission from (COMPLETE REFERENCE CITATION). Copyright (YEAR) American Chemical Society." Insert appropriate information in place of the capitalized words.
- One-time permission is granted only for the use specified in your request. No additional uses are granted (such as derivative works or other editions). For any other uses, please

submit a new request.

Copyright Clearance Center / RightsLink®

ACS Publications — High quality. High impact.

Title: Colloidal Gallium Indium Oxide Nanocrystals: A Multifunctional Light-Emitting Phosphor Broadly Tunable by Alloy Composition
Author: Shokouh S. Farvid et al.
Publication: Journal of the American Chemical Society
Publisher: American Chemical Society
Date: May 1, 2011

PERMISSION/LICENSE IS GRANTED FOR YOUR ORDER AT NO CHARGE

This type of permission/license, instead of the standard Terms & Conditions, is sent to you because no fee is being charged for your order. Please note the following:

- Permission is granted for your request in both print and electronic formats.
- If figures and/or tables were requested, they may be adapted or used in part.
- Please print this page for your records and send a copy of it to your publisher/graduate school.
- Appropriate credit for the requested material should be given as follows: "Reprinted (adapted) with permission from (COMPLETE REFERENCE CITATION). Copyright (YEAR) American Chemical Society." Insert appropriate information in place of the capitalized words.
- One-time permission is granted only for the use specified in your request. No additional uses are granted (such as derivative works or other editions). For any other uses, please submit a new request.

Copyright Clearance Center / RightsLink®

ACS Publications — High quality. High impact.

Title: Phase Transformation of Colloidal In2O3 Nanocrystals Driven by the Interface Nucleation Mechanism: A Kinetic Study
Author: Shokouh S. Farvid et al.
Publication: Journal of the American Chemical Society
Publisher: American Chemical Society
Date: Apr 1, 2012

Bibliography

(1) Wan, Q.; Dattoli, E. N.; Fung, W. Y.; Guo, W.; Chen, Y.; Pan, X.; Lu, W. *Nano Lett.* **2006**, *6*, 2909-2915.

(2) Baxter, J. B.; Aydil, E. S. *Appl. Phys. Lett.* **2005**, *86*, 053114.

(3) Zhang, H.; Banfield, J. F. *J. Mater. Chem.* **1998**, *8*, 2073-2076.

(4) Zhang, H.; Banfield, J. F. *J. Phys. Chem. B* **2000**, *104*, 3481-3487.

(5) Gurlo, A.; Kroll, P.; Riedel, R. *Chem. Eur. J.* **2008**, *14*, 3306-3310.

(6) Wang, T.; Farvid, S. S.; Abulikemu, M.; Radovanovic, P. V. *J. Am. Chem. Soc.* **2010**, *132*, 9250-9252.

(7) Wang, T.; Radovanovic, P. V. *J. Phys. Chem. C* **2011**, *115*, 18473-18478.

(8) Wang, T.; Radovanovic, P. V. *J. Phys. Chem. C* **2011**, *115*, 406-413.

(9) Bawendi, M. G.; Steigerwald, M. L.; Brus, L. E. *Annu. Rev. Phys. Chem.* **1990**, *41*, 477-496.

(10) Karazhanov, S. Z.; Ravindran, P.; Vajeeston, P.; Ulyashin, A.; Finstad, T. G.; Fjellvåg, H. *Phys. Rev. B* **2007**, *76*, 075129.

(11) Shannon, R. D. *Solid State Commun.* **1966**, *4*, 629-630.

(12) Stanek, C. R.; McClellan, K. J.; Uberuaga, B. P.; Sickafus, K. E.; Levy, M. R.; Grimes, R. W. *Phys. Rev. B* **2007**, *75*, 134101.

(13) Philip, J.; Punnoose, A.; Kim, B. I.; Reddy, K. M.; Layne, S.; Holmes, J. O.; Satpati, B.; Leclair, P. R.; Santos, T. S.; Moodera, J. S. *Nat. Mater.* **2006**, *5*, 298-304.

(14) Chopra, K. L.; Major, S.; Pandya, D. K. *Thin Solid Films* **1983**, *102*, 1-46.

(15) Noguchi, S.; Sakata, H. *J. Phys. D: Appl. Phys.* **1980**, *13*, 1129-1133.

(16) Li, X.; Wanlass, M. W.; Gessert, T. A.; Emery, K. A.; Coutts, T. J. *Appl. Phys. Lett.* **1989**, *54*, 2674-2676.

(17) Chu, D.; Zeng, Y. P.; Jiang, D.; Xu, J. *Nanotechnology* **2007**, *18*, 435605.

(18) Ágoston, P.; Erhart, P.; Klein, A.; Albe, K. *J. Phys. Condens. Matter* **2009**, *21*, 455801.

(19) Walsh, A. *Appl. Phys. Lett.* **2011**, *98*, 261910.

(20) Han, S. Y.; Herman, G. S.; Chang, C. H. *J. Am. Chem. Soc.* **2011**, *133*, 5166-5169.

(21) Lim, T.; Lee, S.; Meyyappan, M.; Ju, S. *ACS Nano* **2011**, *5*, 3917-3922.

(22) Nadaud, N.; Lequeux, N.; Nanot, M.; Jove, J.; Roisnel, T. *J. Solid State Chem.* **1998**, *135*, 140-148.

(23) Farvid, S. S.; Dave, N.; Wang, T.; Radovanovic, P. V. *J. Phys. Chem. C* **2009**, *113*, 15928-15933.

(24) Adamson, A. W. In *Physical Chemistry of Surfaces;* A Wiley-Interscience publicatin: New York, 1990.

(25) Reid, A. F.; Ringwood, A. E. *J. Geophys. Res.* **1969**, *74*, 3238-3252.

(26) Prewitt, C. T.; Shannon, R. D.; Rogers, D. B.; Sleight, A. W. *Inorg. Chem.* **1969**, *8*, 1985-1993.

(27) Fuchs, F.; Bechstedt, F. *Phys. Rev. B* **2008**, *77*, 155107.

(28) Epifani, M.; Siciliano, P.; Gurlo, A.; Barsan, N.; Weimar, U. *J. Am. Chem. Soc.* **2004**, *126*, 4078-4079.

(29) Ashok, V. D.; De, S. K. *J. Phys. Chem. C* **2011**, *115*, 9382-9392.

(30) Yu, D.; Yu, S. H.; Zhang, S.; Zuo, J.; Wang, D.; Qian, Y. *Adv. Funct. Mater.* **2003**, *13*, 497-501.

(31) Chen, C.; Chen, D.; Jiao, X.; Wang, C. *Chem. Commun.* **2006**, , 4632-4634.

(32) Lee, C. H.; Kim, M.; Kim, T.; Kim, A.; Paek, J.; Lee, J. W.; Choi, S. Y.; Kim, K.; Park, J. B.; Lee, K. *J. Am. Chem. Soc.* **2006**, *128*, 9326-9327.

(33) Khawam, A.; Flanagan, D. R. *J. Phys. Chem. B* **2006**, *110*, 17315-17328.

(34) Hulbert, S. F. *J. Brit. Ceram. Soc.* **1969**, *6*, 11-20.

(35) Christian, J. W. In *The Theory of Transformations in Metals and Alloys: An Advanced Textbook in Physical Metallurgy;* Pergamon Press: Oxford, 1965; Vol. 7.

(36) Avrami, M. *J. Chem. Phys.* **1939**, *7*, 1103-1112.

(37) Choi, S. Y.; Mamak, M.; Speakman, S.; Chopra, N.; Ozin, G. A. *Small* **2005**, *1*, 226-232.

(38) Kirsch, B. L.; Richman, E. K.; Riley, A. E.; Tolbert, S. H. *J. Phys. Chem. B* **2004**, *108*, 12698-12706.

(39) Avrami, M. *J. Chem. Phys.* **1940**, *8*, 212-224.

(40) Weinberg, M. C.; Birnie, D. P.; Shneidman, A. V. *J. Non Cryst. Solids* **1997**, *219*, 89-99.

(41) Zhang, H.; Banfield, J. F. *J. Mater. Res.* **2000**, *15*, 437-448.

(42) Khawam, A.; Flanagan, D. R. *J. Pharm. Sci.* **2006**, *95*, 472-498.

(43) Zhou, D.; Grant, D. J. W. *J. Phys. Chem. A* **2004**, *108*, 4239-4246.

(44) Gribb, A. A.; Banfield, J. F. *Am. Mineral.* **1997**, *82*, 717-728.

(45) Zhang, H.; Banfield, J. F. *Chem. Mater.* **2005**, *17*, 3421-3425.

(46) Zhang, H.; Banfield, J. F. *Am. Mineral.* **1999**, *84*, 528-535.

(47) Yu, D.; Wang, D.; Qian, Y. *J. Solid State Chem.* **2004**, *177*, 1230-1234.

(48) Chen, C. C.; Herhold, A. B.; Johnson, C. S.; Alivisatos, A. P. *Science* **1997**, *276*, 398-401.

(49) Bryan, J. D.; Gamelin, D. R. *Prog. Inorg. Chem.* **2005**, *54*, 47-126.

(50) Norris, D. J.; Efros, A. L.; Erwin, S. C. *Science* **2008**, *319*, 1776-1779.

(51) Yang, H.; Santra, S.; Holloway, P. H. *J. Nanosci. Nanotechnol.* **2005**, *5*, 1364-1375.

(52) Efros, A. L.; Rashba, E.; Rosen, M. *Phys. Rev. Lett.* **2001**, *87*, 206601.

(53) Ogale, S. B. *Adv. Mater.* **2010**, *22*, 3125-3155.

(54) Wolf, S. A.; Awschalom, D. D.; Buhrman, R. A.; Daughton, J. M.; Von Molnar, S.; Roukes, M. L.; Chtchelkanova, A. Y.; Treger, D. M. *Science* **2001**, *294*, 1488-1495.

(55) Archer, P. I.; Radovanovic, P. V.; Heald, S. M.; Gamelin, D. R. *J. Am. Chem. Soc.* **2005**, *127*, 14479-14487.

(56) Radovanovic, P. V.; Gamelin, D. R. *Phys. Rev. Lett.* **2003**, *91*, 157202.

(57) Schwartz, D. A.; Norberg, N. S.; Nguyen, Q. P.; Parker, J. M.; Gamelin, D. R. *J. Am. Chem. Soc.* **2003**, *125*, 13205-13218.

(58) Matsumoto, Y.; Murakami, M.; Shono, T.; Hasegawa, T.; Fukumura, T.; Kawasaki, M.; Ahmet, P.; Chikyow, T.; Koshihara, S.; Koinuma, H. *Science* **2001**, *291*, 854-856.

(59) Coey, J. M. D.; Venkatesan, M.; Fitzgerald, C. B. *Nat. Mater.* **2005**, *4*, 173-179.

(60) Lee, D. C.; Smith, D. K.; Heitsch, A. T.; Korgel, B. A. *Annu.Rep.Prog.Chem., Sect.C* **2007**, *103*, 351-402.

(61) Yin, Y.; Alivisatos, A. P. *Nature* **2005**, *437*, 664-670.

(62) Mikulec, F. V.; Kuno, M.; Bennati, M.; Hall, D. A.; Griffin, R. G.; Bawendi, M. G. *J. Am. Chem. Soc.* **2000**, *122*, 2532-2540.

(63) Dave, N.; Pautler, B. G.; Farvid, S. S.; Radovanovic, P. V. *Nanotechnology* **2010**, *21*, 134023.

(64) Counio, G.; Esnouf, S.; Gacoin, T.; Boilot, J. P. *J. Phys. Chem.* **1996**, *100*, 20021-20026.

(65) Erwin, S. C.; Zu, L.; Haftel, M. I.; Efros, A. L.; Kennedy, T. A.; Norris, D. J. *Nature* **2005**, *436*, 91-94.

(66) Radovanovic, P. V.; Gamelin, D. R. *J. Am. Chem. Soc.* **2001**, *123*, 12207-12214.

(67) Soo, Y. L.; Ming, Z. H.; Huang, S. W.; Kao, Y. H.; Bhargava, R. N.; Gallagher, D. *Phys. Rev. B* **1994**, *50*, 7602-7607.

(68) Blacklocks, A. N.; Atkinson, A.; Packer, R. J.; Savin, S. L. P.; Chadwick, A. V. *Solid State Ionics* **2006**, *177*, 2939-2944.

(69) Dalpian, G. M.; Chelikowsky, J. R. *Phys. Rev. Lett.* **2006**, *96*, 226802.

(70) Archer, P. I.; Santangelo, S. A.; Gamelin, D. R. *J. Am. Chem. Soc.* **2007**, *129*, 9808-9818.

(71) Gilstrap Jr, R. A.; Capozzi, C. J.; Carson, C. G.; Gerhardt, R. A.; Summers, C. J. *Adv Mater* **2008**, *20*, 4163-4166.

(72) Choi, S. I.; Nam, K. M.; Park, B. K.; Seo, W. S.; Park, J. T. *Chem. Mater.* **2008**, *20*, 2609-2611.

(73) Hammarberg, E.; Prodi-Schwab, A.; Feldmann, C. *Thin Solid Films* **2008**, *516*, 7437-7442.

(74) Minami, T.; Takeda, Y.; Kakumu, T.; Takata, S.; Fukuda, I. *J. Vac. Sci. Technol. A* **1997**, *15*, 958-962.

(75) Chiang, H. Q.; Hong, D.; Hung, C. M.; Presley, R. E.; Wager, J. F.; Park, C. H.; Keszler, D. A.; Herman, G. S. *J. Vac. Sci. Technol. B* **2006**, *24*, 2702-2705.

(76) Hong, N. H.; Sakai, J.; Huong, N. T.; Ruyter, A.; Brizé, V. *J. Phys. Condens. Matter* **2006**, *18*, 6897-6905.

(77) Singhal, A.; Achary, S. N.; Manjanna, J.; Jayakumar, O. D.; Kadam, R. M.; Tyagi, A. K. *J. Phys. Chem. C* **2009**, *113*, 3600-3606.

(78) Kharel, P.; Sudakar, C.; Sahana, M. B.; Lawes, G.; Suryanarayanan, R.; Naik, R.; Naik, V. M. *J. Appl. Phys.* **2007**, *101*, 09H117.

(79) Bérardan, D.; Guilmeau, E.; Pelloquin, D. *J. Magn. Magn. Mater.* **2008**, *320*, 983-989.

(80) Seo, W. S.; Jo, H. H.; Lee, K.; Park, J. T. *Adv Mater* **2003**, *15*, 795-797.

(81) Bañobre-López, M.; Vázquez-Vázquez, C.; Rivas, J.; López-Quintela, M. A. *Nanotechnology* **2003**, *14*, 318-322.

(82) Gill, J. E. *Photochem. Photobiol.* **1969**, *9*, 313-322.

(83) Mason, W. R. In *A practical guide to magnetic circular dichroism spectroscopy;* Wiley: Hoboken, New Jersey, 2007.

(84) Lever, A. B. P. In *Inorganic Electronic Spectroscopy;* Elsevier: Amsterdam, 1984.

(85) McHale, J. M.; Auroux, A.; Perrotta, A. J.; Navrotsky, A. *Science* **1997**, *277*, 788-791.

(86) Blakely, J. M. In *Introduction to the properties of crystal surfaces;* Pergamon Press Ltd.: New York, 1973; Vol. 12.

(87) Chen, L. X.; Rajh, T.; Jager, W.; Nedeljkovic, J.; Thurnauer, M. C. *J. Synchrotron Rad.* **1999**, *6*, 445-447.

(88) Parent, P.; Dexpert, H.; Tourillon, G.; Grimal, J. M. *J. Electrochem. Soc.* **1992**, *139*, 276-281.

(89) Narayanaswamy, A.; Xu, H.; Pradhan, N.; Kim, M.; Peng, X. *J. Am. Chem. Soc.* **2006**, *128*, 10310-10319.

(90) Wang, C. Y.; Dai, Y.; Pezoldt, J.; Lu, B.; Kups, T.; Cimalla, V.; Ambacher, O. *Cryst. Growth Des.* **2008**, *8*, 1257-1260.

(91) Kumar, K. N. P.; Keizer, K.; Burggraaf, A. J. *J. Mater. Chem.* **1993**, *3*, 1141-1149.

(92) Grünwald, M.; Dellago, C. *Nano Lett.* **2009**, *9*, 2099-2102.

(93) Frank, G.; Olazcuaga, R.; Rabenau, A. *Inorg. Chem.* **1977**, *16*, 1251-1253.

(94) Li, X.; Xia, C.; Pei, G.; He, X. *J. Phys. Chem. Solids* **2007**, *68*, 1836-1840.

(95) Somorjai, G. A. In *Introduction to surface chemistry and catalysis;* John Wiley and Sons Inc: New york, 1994.

(96) White, M. A.; Ochsenbein, S. T.; Gamelin, D. R. *Chem. Mater.* **2008**, *20*, 7107-7116.

(97) Figgis, B. N.; Hitchman, M. A. In *Ligand field theory and its applications;* Wiley-VCH: New York, 2000.

(98) Pavlov, R. S.; Marzá, V. B.; Carda, J. B. *J.Mater.Chem.* **2002**, *12*, 2825-2832.

(99) Taran, M. N.; Langer, K.; Platonov, A. N.; Indutny, V. *Phys. Chem. Miner.* **1994**, *21*, 360-372.

(100) Harding, M. J.; Briat, B. *Mol. Phys.* **1974**, *27*, 1153-1172.

(101) Khomenko, V. M.; Platonov, A. N. *Phys. Chem. Miner.* **1985**, *11*, 261-265.

(102) Abragam, A.; Bleaney, B. In *Electron Paramagnetic Resonance of Transition Ions;* Clarendon Press: Oxford, 1970.

(103) Farvid, S. S.; Dave, N.; Radovanovic, P. V. *Chem. Mater.* **2010**, *22*, 9-11.

(104) Farvid, S. S.; Ju, L.; Worden, M.; Radovanovic, P. V. *J. Phys. Chem. C* **2008**, *112*, 17755-17759.

(105) Ju, L.; Sabergharesou, T.; Stamplecoskie, K. G.; Hegde, M.; Wang, T.; Combe, N. A.; Wu, H.; Radovanovic, P. V. *J. Am. Chem. Soc.* **2012**, *134*, 1136-1146.

(106) Bryan, J. D.; Santangelo, S. A.; Keveren, S. C.; Gamelin, D. R. *J. Am. Chem. Soc.* **2005**, *127*, 15568-15574.

(107) Xing, G. Z.; Yi, J. B.; Wang, D. D.; Liao, L.; Yu, T.; Shen, Z. X.; Huan, C. H. A.; Sum, T. C.; Ding, J.; Wu, T. *Phys. Rev. B* **2009**, *79*, 174406.

(108) Abraham, D. W.; Frank, M. M.; Guha, S. *Appl. Phys. Lett.* **2005**, *87*, 252502.

(109) Winkler, E.; Zysler, R.; Mansilla, M. V.; Fiorani, D. *Phys. Rev. B* **2005**, *72*, 132409.

(110) McClure, D. S. *J. Chem. Phys.* **1962**, *36*, 2757-2779.

(111) Piper, T.; Carlin, R. L. *J. Chem. Phys.* **1961**, *35*, 1809-1815.

(112) Fackler Jr, J. P.; Davis, T.; Chawla, I. *Inorg. Chem.* **1965**, *4*, 130-132.

(113) Dingle, R. *Acta Chem. Scand.* **1966**, *20*, 33-44.

(114) Dingle, R. *J. Mol. Spectrosc.* **1962**, *9*, 426-427.

(115) Norberg, N. S.; Dalpian, G. M.; Chelikowsky, J. R.; Gamelin, D. R. *Nano Lett.* **2006**, *6*, 2887-2892.

(116) Lorenz, M. R.; Woods, J. F.; Gambino, R. J. *J. Phys. Chem. Solids* **1967**, *28*, 403-404.

(117) He, H.; Orlando, R.; Blanco, M. A.; Pandey, R.; Amzallag, E.; Baraille, I.; Rérat, M. *Phys. Rev. B* **2006**, *74*, 195123.

(118) Cizeron, J.; Pileni, M. P. *J. Phys. Chem. B* **1997**, *101*, 8887-8891.

(119) Christensen, A. N.; Broch, N. C.; Von Heidenstam, O.; Nilsson, A. *Acta Chem. Scand.* **1967**, *21*, 1046-1056.

(120) Otero Areán, C.; Bellan, A. L.; Mentruit, M. P.; Delgado, M. R.; Palomino, G. T. *Microporous Mesoporous Mater.* **2000**, *40*, 35-42.

(121) Kroll, P.; Dronskowski, R.; Martin, M. *J. Mater. Chem.* **2005**, *15*, 3296-3302.

(122) Nishi, K.; Shimizu, K.; Takamatsu, M.; Yoshida, H.; Satsuma, A.; Tanaka, T.; Yoshida, S.; Hattori, T. *J. Phys. Chem. B* **1998**, *102*, 10190-10195.

(123) Edwards, D. D.; Folkins, P. E.; Mason, T. O. *J. Am. Ceram. Soc.* **1997**, *80*, 253-257.

(124) Binet, L.; Gourier, D. *J. Phys. Chem. Solids* **1998**, *59*, 1241-1249.

(125) Vanithakumari, S. C.; Nanda, K. K. *Adv Mater* **2009**, *21*, 3581-3584.

(126) Maximenko, S. I.; Mazeina, L.; Picard, Y. N.; Freitas Jr, J. A.; Bermudez, V. M.; Prokes, S. M. *Nano Lett.* **2009**, *9*, 3245-3251.

(127) Liang, C.; Meng, G.; Lei, Y.; Phillipp, F.; Zhang, L. *Adv. Mater.* **2001**, *13*, 1330-1333.

(128) Guha, P.; Kar, S.; Chaudhuri, S. *Appl. Phys. Lett.* **2004**, *85*, 3851-3853.

(129) Navrotsky, A.; Ma, C.; Lilova, K.; Birkner, N. *Science* **2010**, *330*, 199-201.